UNIVERSIDADE FEDERAL DE PERNAMBUCO
CENTRO DE TECNOLOGIA E GEOCIÊNCIA-CTG
DEPARTAMENTO DE ENGENHARIA ELETRÔNICA E SISTEMAS
PROGRAMA DE PÓS-GRADUAÇÃO EM ENGENHARIA ELÉTRICA

SAJID FAROOQ

OPTICAL PROPERTIES OF METALLIC NANOPARTICLES AND PERSPECTIVES FOR BIOMEDICAL APPLICATIONS

Recife

2018

SAJID FAROOQ

OPTICAL PROPERTIES OF METALLIC NANOPARTICLES AND PERSPECTIVES FOR BIOMEDICAL APPLICATIONS

Thesis submitted to the Post-Graduation Program in Electrical Engineering of the Federal University of Pernambuco as part of the requirement for obtaining the degree of Doctor in Electrical Engineering.

Area of Research: Photonics.

Supervisor: Prof. Renato Evangelista de Araujo, *D.Sc.*

Recife

2018

Catalogação na fonte
Bibliotecária Margareth Malta, CRB-4 / 1198

F237o Farooq, Sajid.
Optical properties of metallic nanoparticles and perspectives for biomedical applications / Sajid Farooq. – 2018.
120 folhas, il., gráfs., tabs.

Orientador: Prof. Dr. Renato Evangelista de Araujo.
Tese (Doutorado) – Universidade Federal de Pernambuco. CTG. Programa de Pós-Graduação em Engenharia Elétrica, 2018.
Inclui Referências e Apêndices.
Texto em Inglês.

1. Engenharia Elétrica. 2. Nanopartículas metálicas. 3. Ressonância plasmônica de superfície localizada. 4. Método dos elementos finitos. 5. Sensores. 6. Terapia fotodinâmica. I. Araujo, Renato Evangelista de. (Orientador). II. Título.

UFPE

621.3 CDD (22. ed.) BCTG/2018-437

SAJID FAROOQ

OPTICAL PROPERTIES OF METALLIC NANOPARTICLES AND PERSPECTIVES FOR BIOMEDICAL APPLICATIONS

Thesis submitted to the Post-Graduation Program in Electrical Engineering of the Federal University of Pernambuco as part of the requirements for obtaining the degree of Doctor in Electrical Engineering.

Approved: 12/03/2018

EXAMINATION COMMITTEE

Prof. Dr. Marcelo Cabral Cavacanti (Coordinator PPGEE) Federal University of Pernambuco, Recife Brazil	Prof. Dr. Renato Evangelista de Araujo (Supervisor) Federal University of Pernambuco, Recife Brazil
Prof. Dr. Anderson Stevens Leonidas Gomes Federal University of Pernambuco, Recife Brazil	Prof. Dr. Eduardo Fontana Federal University of Pernambuco, Recife Brazil
Prof. Dr. Pierre François Brevet Claude Bernard University Lyon 1, France	Prof. Dr. Diego José Rátiva Millán University of Pernambuco, Recife Brazil

In The Name Of Almighty Allah

The Most Gracious

The Most Merciful.

Dedicated to my family and all those who believe in propagating knowledge to serve the human being.

ACKNOWLEDGEMENT

I witness my urge to seek knowledge of heaven and earth and all between them. I witness the existence of my creator who created me and made me the best creation. I thank my Almighty who bestowed upon me his blessings, mercy, and competence that made me able to understand the diversity of knowledge and expand it without borders for all human being.

I would like to express an elegant gratitude to my prestigious supervisor Prof. Renato Evangelista de Araujo for his tremendous guidance, patience and extraordinary support. He provided me an outstanding and friendly environment for completing my research. He always helps me to understand and acquire knowledge about science and technology. He taught me many courses during this period which helped me improving in myself. I am deeply indebted for his dynamic supervision during the course of my research work.

I am grateful to Prof. Frederico Dias Nunes who is too kind to allow me to work in his simulation laboratory. His guidance and support is always outstanding. I am also thankful to my laboratory colleagues Wellington dos Santos, Fábio Rodrigo, Diogenes Moura, Carlitos Lopes and Thiago Campos for their research assistance and valuable discussions.

Special thanks to my parents who always stand with me through thick and thin. My brothers Umar Farooq, Muhammad Azam and Amer Sohail always encourage me to achieve my goals during the whole period of my life in such a wonderful world.

CAPES is acknowledged for providing a full graduate scholarship for my study and stay in Brazil.

SAJID FAROOQ

"Seek Knowledge From Cradle To Grave".

Muhammad [PBUH]

ABSTRACT

This thesis explains some of the fundamental concepts regarding localized surface plasmon resonance (LSPR) and how to explore it on biosensing and photodynamic therapy. Molecular LSPR sensing and metal-enhanced oxygen singlet generation for photodynamic therapy were demonstrated exploring spherical and non-spherical silver/gold nanoparticles with various size and structures. Mathematical simulations and experimental analyses were used on the discussion of the metallic nanoparticle (NP) size, material and shape contribution to LSPR-based effects. The light-NP interactions were evaluated by the use of Finite Element Method with COMSOL Multiphysics. Computational simulations, focused on the assessment of the LSPR spectrum and spatial distribution of electromagnetic field enhancement near a metallic nanoparticle, were used to ascribe the behavior of crucial parameters, as figure of merit, bulk and molecular sensitivity, which rules the LSPR sensor performance. Here, spherical nanostructures were evaluated as starting points for LSPR biosensor. The theoretical analyses indicated a nonlinear behavior of the bulk and molecular sensitivity of gold and silver nanosphere-based sensing platform as function of the NP size. Significant LSPR peak shift due to the adsorption of molecular layer on the NP surface were observed for nanoparticles with ~ 5 and ~ 40 nm radii. Besides, the theoretical approach used in this work provides insights on the LSPR behavior due to adsorption layer of molecules on a NP surface, establishing a new paradigm on engineering LSPR biosensor. Moreover, molecular sensing was demonstrated by the identification *Candida albicans* antigen. The feasibility of using Ag nanotriangles on LSPR biosensing was also evaluated. Refractive index based sensitivity (406 nm/RIU) and figure of merit (2.6) values were calculated for nanotriangles colloids, with altitudes ~ 57 nm, and attributed to LSPR near field enhancement at the tips of the nanostructure. The interaction of Ag nanotriangles with Methylene blue photosensitizer was also appraised, and 2.2-fold metal enhanced singlet oxygen generation was determined. The association of Methylene blue with Au nanoshells (80 nm silica core/20 nm gold shell) was also quantified, showing 300% increase in singlet oxygen production upon the irradiation of laser light (632 nm). These results introduce new perspectives on the use of metallic nanoparticles on photodynamic process.

Keywords: Metal nanoparticles. Localized surface plasmon resonance. Finite element method. Sensors. Photodynamic therapy

RESUMO

Esta tese explica alguns dos conceitos fundamentais sobre a ressonância plasmônica de superfície localizada (LSPR) e como explorá-la em terapia fotodinâmica e biosensores. Detecção Molecular LSPR e geração de oxigênio singleto realçado por metal para terapia fotodinâmica foram demonstrados pelo uso de nanopartículas de prata / ouro esféricas e não esféricas com vários tamanhos e estruturas. Simulações matemáticas e análises experimentais foram usadas na discussão do tamanho das nanopartículas metálicas (NP), contribuição do material e da forma para os efeitos baseados em LSPR. As interações luz-NP foram avaliadas pelo uso do Método dos Elementos Finitos com o COMSOL Multiphysics. Simulações computacionais, focadas na avaliação do espectro LSPR e distribuição espacial do aumento do campo eletromagnético próximo a uma nanopartícula metálica, foram utilizadas para atribuir o comportamento de parâmetros cruciais, como figura de mérito, bulk e sensibilidade molecular, que regem o desempenho do sensor LSPR. Aqui, as nanoestruturas esféricas foram avaliadas como pontos de partida para o biossensor LSPR. As análises teóricas indicaram um comportamento não-linear da sensibilidade bulk e molecular da plataforma de detecção baseada em nanoesfera de ouro e prata em função do tamanho da NP. Mudanças significativas no pico do LSPR devido à adsorção da camada molecular na superfície da NP foram observadas para nanopartículas com raios de ~ 5 e ~ 40 nm. Além disso, a abordagem teórica utilizada neste trabalho fornece insights sobre o comportamento do LSPR devido à camada de adsorção de moléculas em uma superfície de NP, estabelecendo um novo paradigma na engenharia de biosensores LSPR. Além disso, a detecção molecular foi demonstrada pela identificação do antígeno Candida albicans. A viabilidade do uso de nanotriangulos de Ag em biossensores LSPR também foi avaliada. Os valores de sensibilidade baseada no índice de refração (406 nm / RIU) e mérito (2.6) foram calculados para colóides de nanotriangulos, com tamanho ~ 57 nm, e atribuídos ao aumento de campo próximo do LSPR nas pontas da nanoestrutura. A interação de nanotriangulos de Ag com o fotossensibilizador Azul de metileno também foi avaliada, e a geração de oxigênio singleto 2,2 vezes maior foi determinada. A associação do Azul de metileno com nanocascas de Au (núcleo de sílica de 80 nm / 20 nm de casca de ouro) também foi quantificada, mostrando um aumento de 300% na produção de oxigênio singleto sob irradiação de luz laser (632 nm).

Estes resultados introduzem novas perspectivas sobre o uso de nanopartículas metálicas no processo fotodinâmico.

Palavras-chave: Nanopartículas metálicas. Ressonância plasmônica de superfície localizada. Método dos elementos finitos. Sensores. Terapia fotodinâmica.

LIST OF FIGURES

LIST OF TABLES

LIST OF ABBREVIATIONS

Ag	*Silver*
AgNPl	*Silver nanoplate*
AR	*Aspect ratio*
Au	*Gold*
FEM	*Finite Element Method*
FoM	*Figure of Merit*
FWHM	*Full width at half maximum*
GR	*Green reagent*
Laser	*Laser amplification by stimulated emission of radiation*
LSPR	*Localized surface plasmon resonance*
MEF	*Metal-enhanced fluorescence*
MEO	*Metal-enhanced singlet oxygen generation*
MB	*Methylene blue*
NIR	*Near infrared*
nm	*nanometer*
NPs	*Nanoparticles*
PDT	*Photodynamic Therapy*
PS	*Photosensitizer*
PTT	*Photothermal Therapy*
RI	*Refractive index*
ROS	*Reactive oxygen species*
SEM	*Scanning electron microscopy*
SERS	*Surface enhanced Raman scattering*
SPR	*Surface plasmon resonance*
TEM	*Transmission electron microscopy*
UV	*Ultraviolet*

LIST OF SYMBOLS

$\boldsymbol{\alpha}$	*Polarizability*
$\boldsymbol{c}$	*Speed of light*
$\boldsymbol{e}$	*Charge on electron*
$\boldsymbol{\epsilon_i}$	*Imaginary part of dielectric function*
$\boldsymbol{\epsilon_r}$	*Real part of dielectric function*
$\boldsymbol{\epsilon_0}$	*Permittivity of free space*
$\Delta\boldsymbol{f}$	*Change in frequency*
$\boldsymbol{k}$	*Wave number*
$\boldsymbol{k_{nr}}$	*Non-radiative decay rate*
$\boldsymbol{m_e}$	*Effective mass of electron*
$\boldsymbol{N}$	*Number of density electron*
$\boldsymbol{n_i}$	*Imaginary part of refractive index*
$\boldsymbol{n_r}$	*Real part of refractive index*
$\boldsymbol{\eta_b}$	*Bulk sensitivity*
$\boldsymbol{\sigma_{abs}}$	*Absorption cross sections*
$\boldsymbol{\sigma_{sc}}$	*Scattering cross sections*
$\boldsymbol{\sigma_{ext}}$	*Extinction cross sections*
$\boldsymbol{\Phi_T}$	*Quantum yield of triplet state*
$\boldsymbol{\lambda}$	*Wavelength*
$\boldsymbol{\tau}$	*Life time*
γ	*Phenomenological scattering parameter*
$^3\boldsymbol{\Sigma}$	*Triplet ground state*
$\boldsymbol{\omega}$	*Angular frequency*

TABLE OF CONTENTS

1 INTRODUCTION

1.1 General Introduction on Nanostructures

When the matter is converted into nanostructures, novel physical and optical characteristics may arise, which cannot be emerged in bulk materials. This concept has been attracted for many centuries to humans and later on provided basis for new field of science and technology known as nanotechnology [1]. The nanotechnology has become fascinating to fabricate nanoscale devices, materials and systems within the range of 1 to 200 nm. Nowadays, nanotechnology demonstrates the convergence of various scientific and technologic fields to explore the areas as materials, physics, engineering, chemistry, electronics and biology [2].

Nanotech has brought an investment from health sectors, and is expected to generate a paradigm shift in diagnostic, prevention as well as treatment of several diseases [3]. In particular, nanostructures are bringing a revolution within the wide scientific fields. Elements limited to nanoscale in diverse size or forms provide robust physical properties i.e. electronics, optical, catalytic and magnetic [4]. More than one thousand (1000) sub-wavelength nanostructures have been explored like magnetic, metallic, dielectric, liposomal and carbon based NPs [5]. Within the nanometer range, the nanostructures are well resembled in size with biological molecular structures and structures inside the living cells. Due to their facile surface chemistry and appropriate size match allowing conjugation of gas or biologically active molecules, several nanostructures are potentially exploitable for broad range in medicine and biology applications [3].

One of the pioneer scientists investigated the interaction of light with small inorganic nanoparticles (NPs) was Michael Farady, who first analyzed metal colloids to elucidate brilliant ruby color of gold (Au) and yellow color of silver (Ag) on glass using dispersed colloidal gold/silver particles [6]. However, the colors of nanomaterials have attracted mankind for a long history, for instance, Lycurgus cup which is fourth century Roman glass and currently exhibited in British Museum. Lycurgus cup exhibits deep green color when it is illuminated from ambient light and ruby red color on illumination from inside as shown in figure 1. A plethora of studies, later on, reveal that the cup is made of gold and silver nanoparticles with the size of 50 to 100

nm in diameter and are embedded on the cup with the ratio of gold to silver 3:7 which shows color variations due to absorption as well as scattering [7].

Later on, Gustav Mie published his famous article, in 1908, explaining the basis of scattering and absorption of a plane electromagnetic wave by homogeneous sphere, finding a rigorous solution applying electromagnetic theory [8]. Rapid advances, in the capacity of fabricating nanoscale materials, promise a starting point to bring revolution in sciences and technology. Synthetic procedures continue to evolve and lead to improve the control over size as well as on shapes for sub-wavelength nanostructures. Attaining the optical properties by simply modifying the nanostructures parameters i.e. size, shape, and composition could be attractive and employ in the advance biomedical areas [9]. More sophisticated designs of nanostructures are now in progress, in particular, multifunctional nm-structures [5].

Figure 1 - The Lycurgus cup illuminated from inside (ruby red) and from ambient light (green), obtained from 'British Museum' free image service.

Source**:** taken from [7]

When the size of the particle decreases, the importance of surface to volume ratio increases [10]. To indicate how decrease in size increases the number of atoms on the surface of particle consider, for example, a cube of iron with a length of 1 cm on an edge that contains 10^{-5} % surface atoms. Dividing the same cube into smaller parts until an edge of 10 nm is achieved that gives 10% surface atoms which presents the significance from micro to nano level size conversion [11]. Artificially engineered such materials reveal unique optical properties that cannot be achieved naturally existing materials. In fact, such materials posses positive imaginary (ϵ_i) and negative real (ϵ_r) parts of dielectric function ($\epsilon(\omega) = \epsilon_r + i\epsilon_i$) and considered as capable of supporting plasmon resonance.

Localized Surface Plasmon Resonance (LSPR) is attributed to an optical phenomenon that exhibit due to light-particle interaction when the size of the plasmonic particle is smaller than the wavelength (λ) of the incident light (size << λ) [6,12]. The light-NP interaction creates free electrons of metallic nanostructures to oscillate coherently with respect to lattice positive ions at resonant frequency as shown in figure 2 [13]. The resonance is generated when natural frequency of oscillating dipole of the nm-structure and frequency of incident light are matched [14].

Figure 2 - The localized surface plasmon resonance behavior induced by electromagnetic (EM) field.

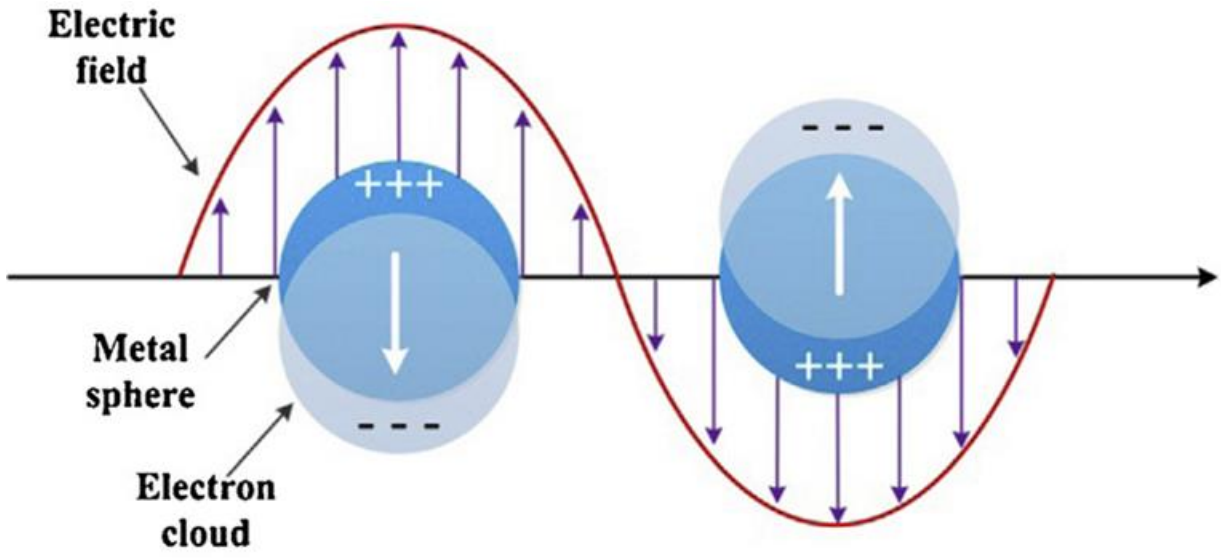

Source**:** taken from [15]

In order to get nano-materials based properties, researchers show great interest to fabricate and design nanoparticles of various size and shapes using different materials such as nanospheres [16], nanorice [17], nanocages [18], nanostars [19], nanorods [20] and nanopyramids [21] which allow the shift of LSPR response from visible to near infrared region (NIR) of LSPR extinction spectrum.

One of the important fabrication methods is chemical reduction to prepare nanoparticles of any shape or size as stable and colloid dispersion in organic or water solvents. Borohydride, ascorbate, citrate and elemental hydrogen can be used as reductants during chemical reduction [22]. Mulvaney et al. employed γ-ray source to generate different types of metallic NPs using gold and silver [23]. Esumi et al. used thermolysis method for the fabrication of palladium NPs in numerous organic solvents [23]. Electrolysis can also lead to size selective synthesis of transition metal NPs [23]. Laser irradiation can be used to fabricate nanoparticles of well defined size and shape without using reducing agents. For instance, silver particles were prepared only by silver salt and surfactant in solution [24].

Although a precise control over the shape, size and structure of metal nanoparticles can be obtained by wet chemical methods, but to manage the inter-particles separation is complicated task in colloid solution [25,26]. A well controlled separation between nanoparticles of different shapes or size can be achieved on a substrate by electron beam lithography as well as nanosphere lithography [27,28]. Duyne et al. used nanosphere lithography (NSL) to fabricate various size of nanostructures. NSL achieves excellent control over NP's shape, size and inter-particle separation [29]. However, NSL and electron beam are expensive techniques and need high vacuum to prepare the NPs.

The light can be scattered or absorbed by metal nanostructures with remarkable efficiency, thereby, the NPs present 4 to 5 order higher optical cross sections than to conventional dyes [30], at a resonance frequency. For example, Au nanospheres of 40 nm size exhibit molar absorption coefficient 7.66×10^{9} $M^{-1}cm^{-1}$ that is 5-times higher than that of indocyanine green (1.08×10^{4} $M^{-1}cm^{-1}$) and are commonly introduced in photothermal therapy (PTT) [31]. Similarly, the small size of AuNPs (80 nm diameter) demonstrates the comparable scattering to larger polystyrene (300 nm diameter) at wavelength 560 nm [32]. The particular shape like Au

nanocages, due to their moderate scattering and higher absorption, possess hidden potential as contrast agent in optical imaging [33]. Therefore, the metallic nano-size structures have been utilizing as contrast agents for optical imaging modalities, fluorescence microscopy and optical coherent tomography because of their high scattering features [34].

The absorption or scattering of nanostructures can also be changed by varying the size, shape or composition. The dielectric core with metal shell or metal core with dielectric shell, for instance, can enhance absorption/scattering on changing the core/shell dimensions [30]. The silica coated gold nanostructures, in particular, as a consequence of their valuable optical characteristics and facile functionalization show high stability, biocompatibility, low immunogenicity, and versatility comparatively to symmetric bare gold nanoparticles [35].

Metallic nanostructures are increasingly receiving attention as an important starting point for medical therapy and medical diagnosis [36–39]. The plasmonic NPs establish several features of LSPR sensing that explore their importance in biomedical and biological assays, further LSPR sensing. The use of plasmonic NPs for label free assays localize the sensing area and thus reduce the total amount of analyte to generate a signal, further minimizing the effects of diffusion limited mass transport.

Several biomolecules have been detected using LSPR-based effects. For instance, biotin-streptavidin is appropriate to LSPR sensing because biotin (a small organic molecule) is conjugated to NP surface, and protein streptavidin (large molecule) is detected [40]. Antigen-antibody detection is another example of LSPR assay. Detection antibody is basically conjugate of antibody-NPs through self assembled monolayer and then standard bio-conjugate linker. Most reports characterized the sensitivity based on dose-response curve, for example, detection of a marker for Alzheimer's disease. Besides of antibody-antigen and biotin-streptavidin interactions, other bio-markers have been probed using LSPR sensors as aptamer-protein, toxin-receptor, cytochrome-inhibitor, protein-carbohydrate and nucleic acid hybridization interactions [41].

Moreover, morphology related optical features have been developed significantly by tuning spherical into non-spherical forms [42]. In particular, shape associated study described the high performance of sensing platform using non-isotropic particles [43,44]. Due to poor monodispersity and sharp edges of Au bipyramids, enable them to utilize in colorimetric sensor

to detect influenza virus [45]. Further, Au nanorods are compared with nanobypramids for biosensing application, and bipyramids show 64-fold enhancement than to the rods 16-fold enhancement containing sensor systems [46].

Metallic nanoparticles have also been explored as contrast agents for optical imaging modalities, as fluorescence microscopy and optical coherent tomography [47]. The metal NPs are usually not fluorescent, and therefore for imaging applications they are frequently tagged with fluorophores and targeting molecules [48]. On medical therapy, gold nanostructures have been explored on photo-thermal therapy [49]. Light energy absorbed by the metallic nanoparticle is converted to heat that dissipates, increasing the temperature of the NP surrounding medium. Various shapes as spheres, rods, and shells show robust potential for thermal related therapy [50].

Likewise, Photodynamic Therapy (PDT) has emerged as one of the important therapeutic options, for several diseases treatment. PDT combines photosensitizing drugs and light to induce selective damages on a target tissue [51]. Since, singlet oxygen is considered as primary cytotoxic-agent that may damage a wide variety of cells [52]. Therefore, the PDT performance is largely dependent on the production of oxygen singlet ($^1O_2$). Nearby the photosensitizer (PS), the nanostructures increase the local field which results more production of $^1O_2$ [53]. The presence of plasmonic nanoparticles is much required for hydrophobic PSs that are more complicated to manage for applications in vivo [54]. The metal NPs are functionalized with PS through weak interactions or strong covalent bonding. The presence of nanoparticles in close proximity to PS can enhance the quantum yield as well as stabilize the PS against photobleaching [55]. Furthermore, the weak pharmaceutical effects result in part of poor penetration of PS into the cellular-compartment of tumor. Embedding the PS with metal nanoparticles can enhance the drug penetration into cells/tissues. Additionally, the reduction of drug can be protected by embedding it into the silica shells in *vitro* [52].

The objective of this thesis is to explore optical characteristics of noble metal nanostructures for engineering new platforms for biosensing and optical related therapy.

In this thesis, it will be demonstrated some of the basic concepts regarding localized resonance response and how to scrutinize it for bio-applications. Numerical simulations and experimental results will be used on the investigation of size, shape and material of the NP

contribution to the LSPR sensor. Furthermore, the relationship between EM field decay length and size of the nanoparticles will be discussed to probe the LSPR sensor performance. This thesis will also investigate the possibility of exploring singlet oxygen generation by Methylene blue in the metallic NPs presence.

1.2 Overview

The current **Chapter 2** describes some specific mathematical theories i.e. Mie theory and Quasi-Static approximation as well as Finite Element Method. It also describes influence of various parameters on which LSPR is reliant on, such as shape, size, surrounding dielectric medium and material compositions. It also includes expansion of Campbell's model to predict the LSPR peak shift due to adsorbate molecules layer. Moreover, the behavior of crucial parameters such as Figure of Merit, bulk/molecular sensitivity, MEF and MEO, are investigated to probe the effects of NPs.

In **Chapter 3,** gold and silver nanoparticles were explored as starting point to assess the plasmonic optical characteristics of the nanostructured sensor platform. Here, for the first time in the literature, Campbell's model was evaluated exploiting a NP size-dependence approach. This chapter provides insights on the LSPR behavior due to adsorption of molecules layer on a NP surface, establishing a new paradigm on engineering LSPR biosensor.

Chapter 4 describes the optical properties of Ag nanoplates and evaluate their potential to manipulate on LSPR biosensing and PDT applications. The analysis which is based on experimental and simulated results, focus on the assessment of the LSPR spectral shift and spatial distribution of the electromagnetic field enhancement near metallic nanoplates, with various altitude lengths as well as thickness. The important parameters that explore the LSPR sensor performance for triangular NPs, such as sensibility and Figure of Merit, are identified and resolved. The interaction of Ag nanoplates with MB is also appraised, and MEO is evaluated and quantified.

In **Chapter 5,** the effects and characterization of negatively charged (silica core/Au shells) nanostructures were demonstrated to explore their potentials for PDT applications. The near electric field around the nanoshell was calculated by Finite Element Method (FEM)

simulations. The influence of irradiation time and concentration of metallic nanostructures on MEO were also appraised and quantified.

The conclusion and future perspectives are summarized in **Chapter 6**.

2 OPTICAL PROPERTIES OF METAL NANOSTRUCTURES

2.1 Evaluation Methods for Optical Properties

The optical properties of metallic nanostructures can be characterized analytically by solving Maxwell's equations under proper boundary conditions. Here, two methods are used to solve the spherical shape metallic NPs: Mie theory for calculating light-scattering characteristics with any arbitrary size and Quasi-Static approximation for particles of size less than 30 nm.

2.1.1 Dielectric Functions of Au and Ag Nanoparticles

The fundamental optical characteristics of metal nanoparticles may be predicted calculating their size-dependent dielectric function. The dielectric function value of a metal is influenced by its structure. As the metallic nanoparticle becomes smaller, electron scattering on the NP surface becomes more pronounce, and therefore affecting the dielectric function value of the material. The complex dielectric function ($\epsilon(\omega)$) can be described by Drude model, which also account for the conduction electrons scattered by the nanoparticle surface. Therefore, dielectric function can be written as [56]:

$$\epsilon(\omega) = \epsilon_{inter}(\omega) + \frac{\omega_p^2}{\omega(\omega + i\gamma)} \tag{2.1}$$

where $\epsilon_{inter}(\omega)$ depicts interband transitions, ω_p represents plasmon frequency and γ is a phenomenological scattering parameter. The plasma frequency can be expressed for bulk metal by:

$$\omega_p = \left(\frac{Ne^2}{\epsilon_0 m_e}\right)^{1/2} \tag{2.2}$$

where m_e is the effective mass of an electron, N is the number density of free electrons, e is the charge of an electron and ϵ_0 dielectric function of free space (vacuum). For nanoparticles, the scattering parameter has inherent contributions of the intrinsic properties of the material as well as from interface scattering and therefore, it can be described as $\gamma = \gamma_{bulk} + \gamma_{scat}$.

Interface scattering becomes significant when the effective electron path length L_{eff} is larger than to the nanoparticle itself [57]. The effective path length for convex shapes particles, for instance sphere, rods, cubes etc, is expressed as $L_{eff} = 4V/S$ where V is the volume and S is the surface area [56]. Thus, the scattering parameter is given by $\gamma_{scat} = AV_f/L_{eff}$ where A is scattering efficiency [57]. For gold, $\gamma_{bulk} = 1.07\text{x}10^{14}$ s^{-1}, $V_f = 1.40\text{x}10^{6}$ ms^{-1}, while for silver $\gamma_{bulk} = 3.22\pm1.22\text{x}10^{13}$ s^{-1}, and $V_f = 1.39\text{x}10^{6}$ ms^{-1} [58]. Table 1 depicts the spheres radii and effective electron path lengths with respect to their sizes.

The figure 3 depicts the dielectric functions of Au and Ag particles, considering size correction, showing that decreasing the nanoparticle radius (effective path length) both real (ϵ_r) and imaginary parts (ϵ_i) of metallic dielectric changes. The real part of dielectric function depicts the pattern of electron polarization in the medium as a consequence of incident field and determines LSPR peak position.

Table 1 - Nanospheres radii and their corresponding effective electron path lengths (L_{eff}).

Sphere Radius (nm)	L_{eff} **(nm)**
5	6.67
10	13.34
15	20.00
20	26.67
25	33.34
30	40.00
35	46.67
40	53.34
45	60.00
50	66.67

Source: belong to author

Figure 3 - Complex dielectric function based on surface scattering of gold (a) and (c), as well as silver (b) and (d) nanospheres with different radii (5, 10, 15, 20, 25, 30, 35, 40, 45, 50 nm).

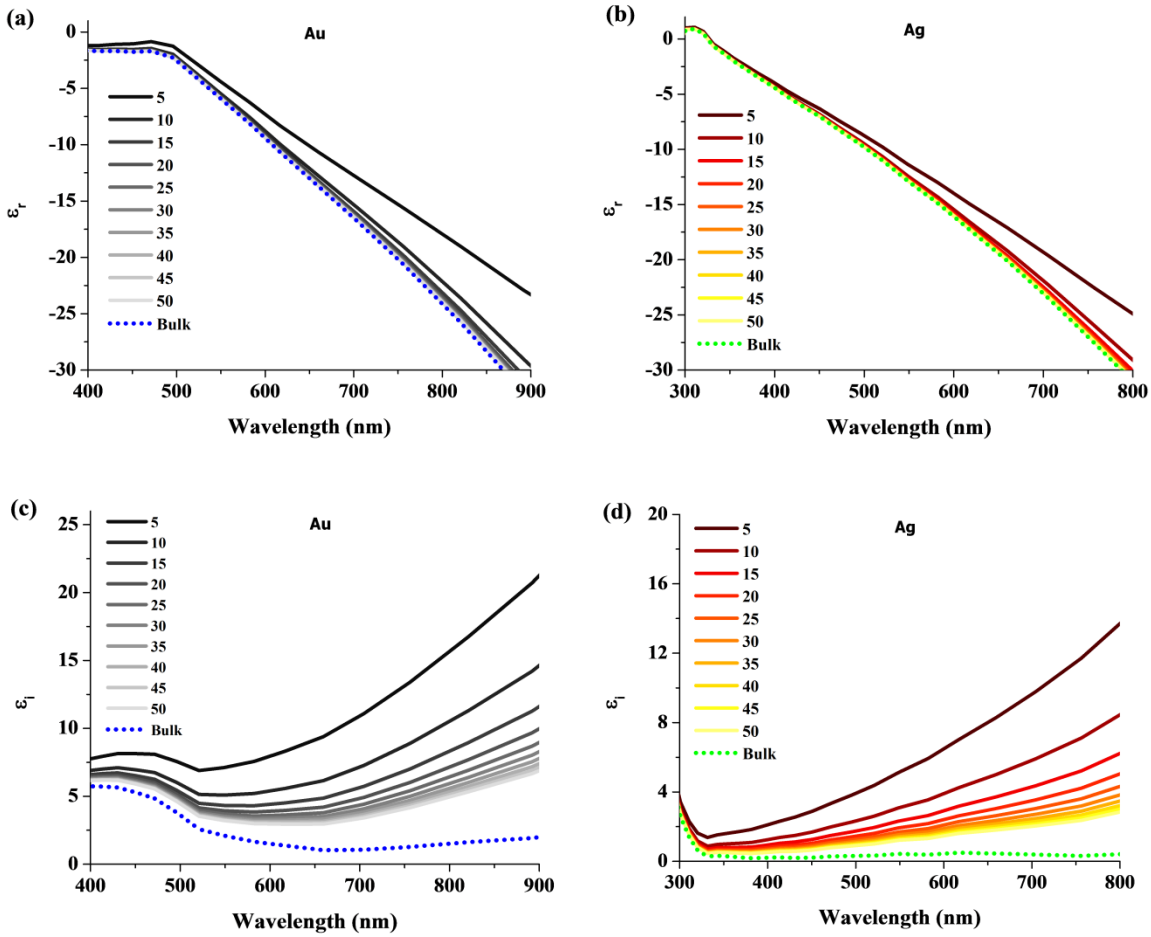

Source**:** belong to Author

However, imaginary part ϵ_i describes energy dissipation or loss in the materials. Decreasing of the nanoparticle size leads to a lower polarizability of the metal (fig. 3(a) and (b)), while increases the magnitude of ϵ_i (fig. 3(c) and (d)). Therefore, higher loss is expected for metallic particle with 5 nm radius than to 50 nm radius nanostructures due to surface scattering. One can notice that on decreasing effective path length (particle radius), both real and imaginary parts of $\epsilon(\omega)$ are affected. Real part of $\epsilon(\omega)$ (fig. 3(a) and (b)) becomes less negative, showing that metals are less polarizable, while increase in magnitude of imaginary part (fig. 3 (c) and (d)) of $\epsilon(\omega)$ causing increase in overall losses in the NP. In particular, these effects yield overall poor plasmonic metal.

2.1.2 Mie Theory

Lord Rayleigh, in 1871, gave the basic understanding of dipole moment after investigating sub-wavelength nanostructures excited by EM radiation [59]. Later on, it was Mie who was responsible of real breakthrough to analyze the light coupling with spherical NPs and his rigorous solution resembled with Rayleigh scattering. He derived the following equations to discuss scattering, absorption and extinction cross-sections induced by EM interaction with spherical NPs [12]:

$$\sigma_{sca} = \frac{2\pi}{|k|^2}\sum_{l=1}^{\infty}(2l+1)(|a_l|^2 + |b_l|^2) \tag{2.3}$$

$$\sigma_{ext} = \frac{2\pi}{|k|^2}\sum_{l=1}^{\infty}(2l+1)[Re(a_l + b_l)] \tag{2.4}$$

$$\sigma_{abs} = \sigma_{ext} - \sigma_{sca} \tag{2.5}$$

where *k* is wavenumber, *l* represents integers that are used to explain dipole (*l* = 1), quadrupole (*l* = 2) and multipole of higher orders of scattering. The parameters a_l and b_l are derived from Riccati-Bassel functions ψ_l and χ_l

$$a_l = \frac{m\psi_l(mx)\psi'_l(x) - \psi'_l(mx)\psi_l(x)}{m\psi_l(mx)\chi'_l(x) - \psi'_l(mx)\chi_l(x)} \tag{2.6}$$

$$b_l = \frac{\psi_l(mx)\psi'_l(x) - m\psi'_l(mx)\psi_l(x)}{\psi_l(mx)\chi'_l(x) - m\psi'_l(mx)\chi_l(x)} \tag{2.7}$$

Here $x = k_m r$ where r is the radius of spherical NP and k_m is the wavenumber in the medium. Similarly, $m = n/n_m$ where $n = n_r + in_i$ is the complex refractive index of the noble metals and n_m is the surrounding medium refractive index. $\chi_l(x)$ and $\psi_l(x)$ are Ricatti-Bessel cylindrical functions [60].

2.1.3 Quasi-Static Approximation

The electrostatics approximation is explored to understand optical characteristic of the metallic NPs that posses size very small ($k_m r \ll 1$) as compare to incident light wavelength. Consequently, such electrostatic problem can be solved using Laplace equations with proper boundary conditions [61]. Consider a sphere of radius *r* is placed in homogeneous medium and its diameter is assumed to be smaller than the wavelength of applied field E_0, as shown in figure 4. As the particle size is smaller, therefore, the field is supposed to be uniform inside the spherical nanoparticle. The internal field (E_i) is calculated as [62]:

$$E_i = E_0 \frac{3\epsilon_m}{\epsilon + 2\epsilon_m} \tag{2.8}$$

where ϵ_m is dielectric function of surrounding medium.

Figure 4 - The study of spherical shaped nanoparticle $r << \lambda$ in homogeneous electrostatic field.

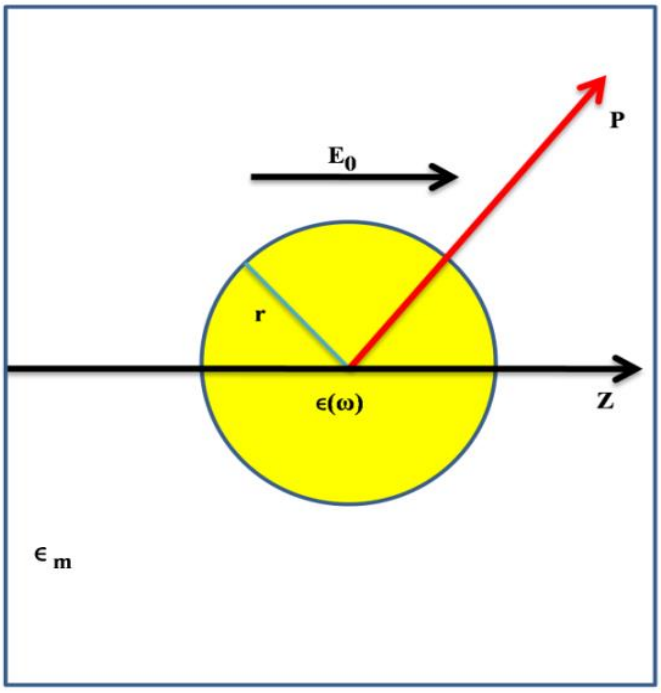

Source**:** taken from [61]

Therefore, the polarizability "α" for a particle of radius r due to applied field is

$$\alpha = 4\pi r^3 \left(\frac{\epsilon - \epsilon_m}{\epsilon + 2\epsilon_m}\right) \tag{2.9}$$

where $\epsilon = \epsilon_r + i\epsilon_i$ is the dielectric function of the NPs. The electrostatics solution related to small sphere in quasi-static regime using oscillating EM field, and is considered to be time dependent but not spatial dependence on EM field. Also in this approach, ϵ and ϵ_m in the above equations are replaced by $\epsilon(\omega)$ and $\epsilon_m(\omega)$ due to their frequency dependent behavior, and ϵ_m may be taken as real constant (non-absorbent medium). It is apparent that polarizablity observes robust resonant under the condition i.e. $\epsilon + 2\epsilon_m$ is minimum.

That is expressed as:

$$(\epsilon_r + 2\epsilon_m)^2 = 0 \tag{2.10}$$

If ϵ_i is negligible, ϵ_r should be negative that is necessarily for resonance, known as Fröhlich condition ($\epsilon_r = -2\epsilon_m$). The corresponding cross-sections for absorption (σ_{abs}) and scattering (σ_{sca}) for small nanoparticles ($\leq$ 30 nm in diameter) can be calculated as [8]:

$$\sigma_{sca} = \frac{k^4}{6\pi}|\alpha|^2 = 8\pi\frac{k^4}{3}r^6\left|\frac{\epsilon - \epsilon_m}{\epsilon + 2\epsilon_m}\right|^2 \tag{2.11}$$

$$\sigma_{abs} = kIm(\alpha) = 4\pi k r^3 Im\left(\frac{\epsilon - \epsilon_m}{\epsilon + 2\epsilon_m}\right) \tag{2.12}$$

Extinction cross section (σ_{ext}) is obtained $\sigma_{ext} = \sigma_{sca} + \sigma_{abs}$ by combining equations (2.11) and (2.12) and resultant equation is demonstrated as:

$$\sigma_{ext} = \frac{9\omega}{c}\epsilon_m^{1.5} V \frac{\epsilon_i}{(\epsilon_r + \epsilon_m)^2 + (\epsilon_i)^2} \tag{2.13}$$

where V is volume, c is the speed of light and ω is angular frequency.

It is clear (equation (2.13)) that increasing the value of ϵ_m, the extinction cross section becomes more intense [63]. One can notice that absorption process, on a quasi static approach, is

proportional to r^3, although scattering cross section is proportional to r^6. Therefore, absorption-process will be more effective than scattering on particles with dimension smaller than 10 nm. As a result, for large NPs size, the scattering process play significant role on the resulting extinction spectra [64]. When the particle size increases, the higher order modes are induced due to non-homogeneous polarization of NPs by incident light and resultantly plasmon peak grows towards longer wavelength [65].

2.1.4 Anisotropic NPs beyond Mie Theory

Mie theory and quasi-static approach are considered an efficient tool for spherical shaped NPs. However, complex shapes/morphologies such as nanocages, nanorods, nanoplates, nanobipyramids, nanostars, nanorice and nanocubes, cannot be properly evaluated using Mie theory. The elongated metallic nanoparticles, for instance Au nanorods, can be studied theoretically using Mie Gans theory to depict longitudinal and transverse LSPR modes [66]. Although, for various other shapes, different numerical methods are applied to characterize the morphologies such as discrete-dipole approximation (DDA), boundary element method (BEM), finite element method (FEM) and finite difference time domain (FDTD). In particular, FEM is a standard method to solve the partial differential equations, associated to complex geometries. In this thesis, numerical calculations based on FEM are performed using COMSOL Multiphysics, describing the interaction of light with metallic NPs of different shapes (Appendix A).

2.2 Important Factors for LSPR

The plasmon resonance is highly sensitive to different shapes, size, material composition and dielectric function of surrounding medium for plasmonic NPs which are used to manipulate LSPR spectra. Various types of NPs, in the last decade, have been fabricated and investigated to evaluate LSPR spectra and to enhance electric field on or around the NPs.

2.2.1 Shapes dependence of LSPR

Fascinating changes on LSPR properties can be observed by the modification of the metallic NP morphology. Recent progress in fabrication and synthesis of NPs increased the interests of plasmon modes in broken-symmetric and symmetric nanostructures [67].

Nanosphere lithography and electron beam lithography techniques are used to design nanostructures with multiple shapes and to control the inter-particle distance on a substrate surface [68].

These methods are expensive limiting their use to a restricted number of research groups. Additionally, colloidal chemistry methods allow inexpensive synthesis of nanoparticles with various shapes, albeit unable to control over the distance between the particles [69]. LSPR feature is highly dependent on shapes, which enable them to render plasmon peak in manifold spectral regions [70]. The sharper tips NPs, in particular, are expected to exhibit LSPR at longer wavelength compared with spheroids. For instance, the red-shift more than 200 nm for scattering spectra was examined for individual triangular Ag nanoplate than to the spherical NP peak shift [71]. The different geometrical shapes have specific LSPR spectra such as 506, 537, 548, 603 and 629 nm for triangles, trapezoids, irregular circular cylinder, hexagonal and parallelograms, shapes respectively [72]. Wang et al. fabricated AuNPs of different shapes such as nanospheres, nanorods, nanocubes, nanobranches and nanobipyramids, to investigate shape dependent LSPR resonance from visible to near infrared region [73]. Figure 5 shows a LSPR peak of Ag triangular NP red-shift more than 400 nm as compare to spherical particle.

Figure 5 - The extinction LSPR spectra and TEM images of silver nanostructures.

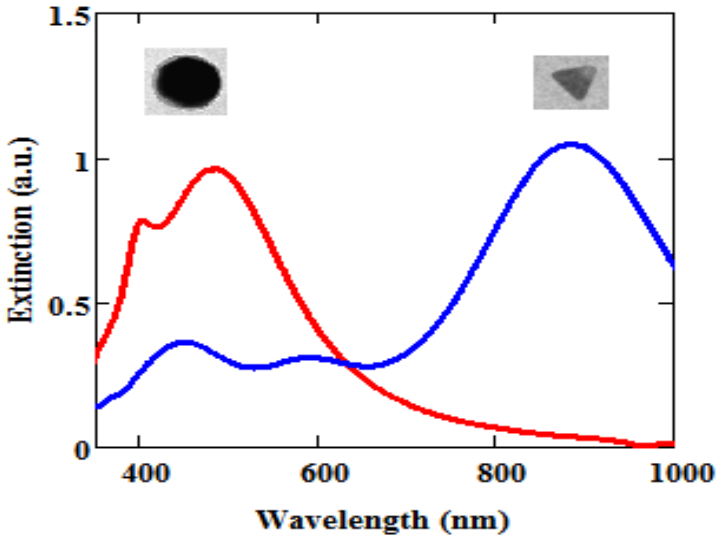

Source: belong to author

2.2.2 Size dependence of LSPR

The size of a metallic nanostructure plays an important role on the light-NP interaction. The decreasing the size of metallic NPs enhance the dipole contribution on the LSPR spectra. However, increasing the radius of NPs, higher order modes become relevant in the extinction cross section and quadrupole resonance can overcome on dipole participation. In fact, scattering and absorption cross sections are size dependent, as displaying in equations (2.11) and (2.12). For larger metallic structures, the light-NP interaction will be determined mainly by scattering. Scattering cross sections rapidly increase with increasing the size of metallic NPs ($\sigma_{sca} \propto r^6$) [60,74]. The scattering increases as a function of size, therefore, radiation damping causes broadenings, drastic shift and increases the amplitude of extinction [65]. The particles of small diameters ($d \leq 30\, nm$), the extinction spectra are dominated by dipole resonance; however, scattering which is radiative phenomenon, may be negligible [75]. When the particles possess dimensions smaller or comparable to the mean free path of oscillating conduction electrons, dielectric function of the NPs is highly dependent on the nanostructure size, as described in section (2.1.1).

For NPs with diameters ($d \geq 50\, nm$), scattering is significant factor that reduces the role of the surface damping and retardation effects are considered in the optical response [31]. Radiation scattering arises because the electrons accelerate as a result of EM field, causing loss of energy and leading to broadening of LSPR spectrum [76]. The peak position of LSPR band is not dependent strongly on the size of AuNPs in the range 8-60 nm. For larger particles, the peak clearly red shifts and broadens [77]. The spectra of figure 6 were obtained by using Mie simulations.

Additionally, the spectrum changes are more pronounced for AgNPs than for Au nanostructures. Moreover, Ag nanospheres show the presence of quadrupole mode when the radius of sphere exceeds 30 nm, while the most dominant mode for Au nanospheres is due to dipole resonance. The simulations also indicate that the FWHM of the extinction spectrum decrease with respect to the reduction of NPs radius.

Figure 6 - The LSPR extinction efficiency for gold (a) and silver (b) nanospheres in water.

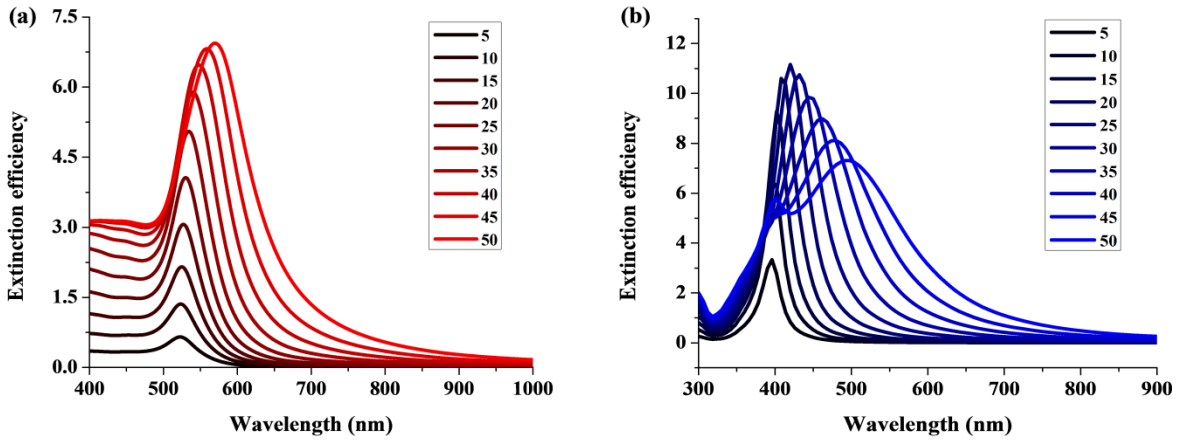

Source: belong to author

2.2.3 Materials dependence of LSPR

LSPR can be achieved theoretically in any metal, semiconductor or alloy by prompting the Fröhlich condition. On LSPR application, Au and Ag are mostly used metals with negative real part and small positive imaginary part of dielectric function. In particular, metals like aluminum offers plasmon resonance in ultraviolet region where several organic molecules absorb light [78]. Copper (Cu) is another example of plasmonic metals that exhibits the LSPR resonance. Cu nanostructure presents a narrow and intense LSPR peak similar to Ag and Au nanoparticles, with the same structure and geometry [79].

Na, Li and Ga may also satisfy Fröhlich criterion, showing plasmon resonance of these metals at UV-Visible spectrum [79–81]. However, these metals are easily oxidized and highly reactive to the surrounding, make difficult to use them experimentally like Au or Ag [82]. It is a fact that surface plasmon resonance, in case of Ag and Au, can be tuned into UV-Visible or near IR spectrum [83]. The real and imaginary parts of dielectric functions for Au as well as Ag are shown in figure 7. Figure 7 (a) depicts the real parts of dielectric functions for both Au and Ag. One can notice that negative values of ϵ_r of dielectric function for Au and Ag reaching ~ –2.0 close to 354.4 nm and 494.4 nm, respectively, fulfilling the Fröhlich condition ($\epsilon_r = -2\epsilon_m$) for a NP in air. Figure 7(b) indicates the imaginary parts of dielectric function for both Au and Ag.

Figure 7 - The real (a) and imaginary (b) parts of dielectric functions for both Au and Ag, respectively.

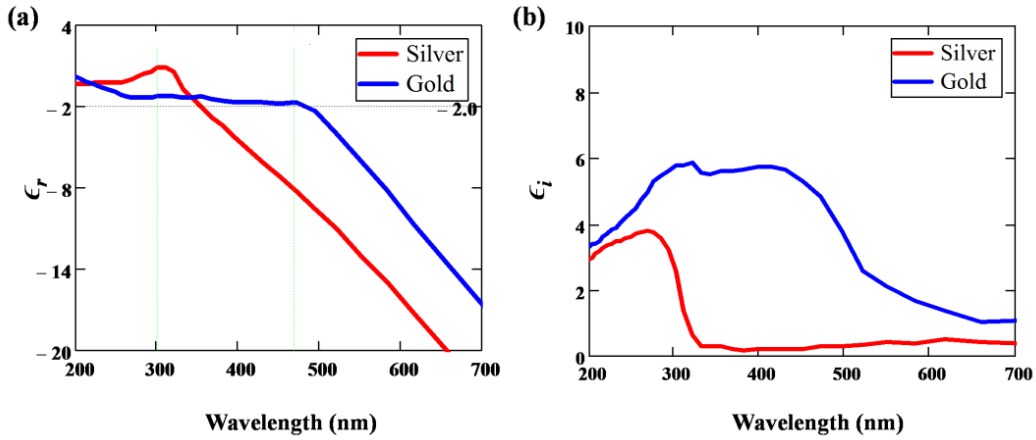

Source: taken from Johnson and Christy [58].

However, imaginary part of dielectric function has small positive values that cause the energy loss of matter and reason of broadening of linewidth of Au and Ag. Close to LSPR resonance wavelength, the imaginary parts of dielectric function are 3.81 and 0.28 for Au (@494.4 nm) and Ag (@354 nm), respectively, that cause energy loss in air.

2.2.4 Surrounding Medium dependence of LSPR

The surface of plasmon NP is very sensitive to the change in local medium and the influence of surrounding medium on LSPR of metallic particles have been studied for many years. As the RI of the surrounding medium increases, there is a peak-shift in LSPR wavelength [84]. The spectral dispersion in real part of dielectric function plays a remarkable role to investigate the surface plasmonic resonance due to change in RI of local environmental medium [85]. The electric field around NP generates the polarization in the local environment and the polarized medium has the influence on the restoring force in the presence of external EM field.

As the values of the dielectric function of the surrounding medium increase, the small value of restoring force is observed and more charge is compensated by the polarized surrounding medium [84]. The spectra of single NP due to scattering shows the change in color of AgNP from blue to green after the addition of oil as shown in figure 8 (a) and (b) respectively. After removing the oil, the color of AgNP is changed again to blue, shown in figure 8 (c) [86]. As the RI of the solvent increases around the AuNP, the spectral plasmon peak gradually becomes

red-shift, as can be observed on the extinction spectra of gold nanoparticles (figure 8). The graphics in figure 9 were obtained by FEM with COMSOL Multiphysics (detailed in chapter 3).

Figure 8 - The transfer of colors with change of RI by oil under dark field; before oil (a), with oil (b), and after removing oil (c).

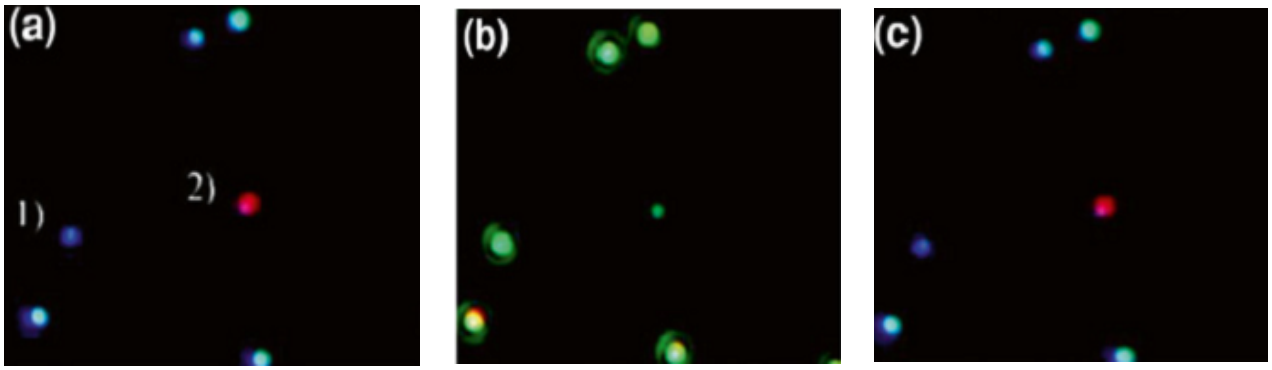

Source: taken from [86].

Figure 9 - The extinction spectra of individual gold nanoparticle (r = 50 nm) as a function of refractive index of solvents.

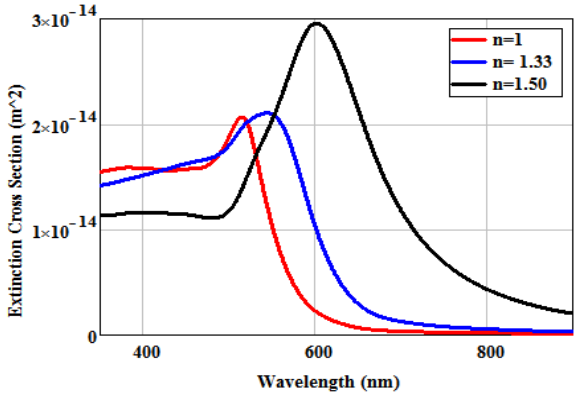

Source: belong to author

2.3 Important Factors for LSPR Sensors

2.3.1 Bulk Sensitivity

Sensitivity is one of the important parameters to characterize a sensor. For LSPR based sensors, bulk sensitivity is termed as the variation of LSPR peak position with respect to the change in RI unit (RIU) of the medium, and its unit is eV/RIU or nm/RIU [87]. The most commonly employed equation for refractive index (RI) based sensitivity or bulk RI sensitivity can be written as [88]:

$$\eta_b = \frac{\Delta\lambda_{LSPR}}{\Delta n_m} \tag{2.14}$$

where η_b represents bulk sensitivity, while $\Delta\lambda_{LSPR}$ and Δn_m are, respectively, the wavelength shift of LSPR peak and the refractive index change of a medium. The refractive index changes of the surrounding medium induces wavelength shift of LSPR peak of NPs, therefore, playing a critical role in η_b . For instance, LSPR spectrum from Au nanospheres suspension can significantly red-shift by changing the colloidal solvent as shown in figure 9 (previous section). For 50 nm diameter Au nanospheres, the spectral shift in plasmonic peak is nearly linear with

Figure 10- The plasmon peak wavelength shift for different refractive index medium obtained experimentally.

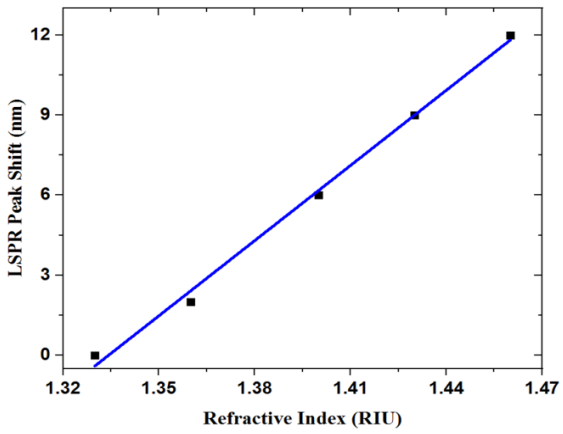

Source**:** belong to author

respect to change in RI of the solvents as represented in figure 10, and calculated sensitivity was 85 nm/RIU.

The significant larger shift in LSPR peak observed, encourage researchers to design and fabricate different structures or shapes of metallic NPs with different size. In addition, bulk sensitivity can be manipulated as function of various shapes. Xia et al. investigated the η_b value of Au nanoshells versus Au nanospheres with same size, noticing that η_b value is bigger for shells (328.5 nm/RIU) than to spheres (66.5 nm/RIU) [89]. Chen et al. calculated the η_b of AuNPs of various shapes as branches > bipyramides > rods > cubes > spheres with their corresponding η_b values 703 > 540 > 288 > 83 > 44 nm/RIU, respectively [90].

Neils et al. reported to the η_b value of AuNPs in the shape of XI cavity, and calculated a higher value of η_b 1000 nm/RIU [91]. A research group have fabricated sharp axes nanoparticles and calculated η_b for nanorice ($\eta_b = 801\ \mathrm{nm/RIU}$) [17], nanocrescents ($\eta_b = 880\ \mathrm{nm/RIU}$) [92] comparatively larger than to the gold nanorods and nanoshells. The reported η_b for Au nanorings is 880 nm/RIU which is five times higher than that of nanodisks with same diameter and at the same spectral position [93]. Hafner et al. designed a complex star-shaped of AuNP that has multiple plasmonic peaks showing bulk sensitivity at 665 nm/RIU [94].

Yu and coworkers investigated the Au nanorods with various aspect ratios from 2.8-7.0 with corresponding η_b values ranging from 450-1150 nm/RIU [95]. Zalyubovskiy et al. have reported the η_b value of ring, split ring and sandwich possessing same dimensions which followed η_b order as ring (503) > split ring (498) > sandwich (441) with units nm/RIU [96]. Table 2 presents an overview of various nanostructures explored on sensing. The results suggest a strong correlation between NP surface area and η_b values.

2.3.2 Figure of Merit

LSPR sensing depends not only on the plasmonic peak shift but also on the precision to identify spectral changes. Therefore an important Figure of Merit (FoM) of plasmonic sensor is defined as [97]:

$$FoM = \frac{\eta_b}{FWHM} \tag{2.15}$$

where FWHM is the full width at half maximum of the LSPR peak. Figure 11 indicates plamonic FWHM and peak shift used on sensing procedure.

Figure 11 - The LSPR spectral shift and FWHM for sensing procedures.

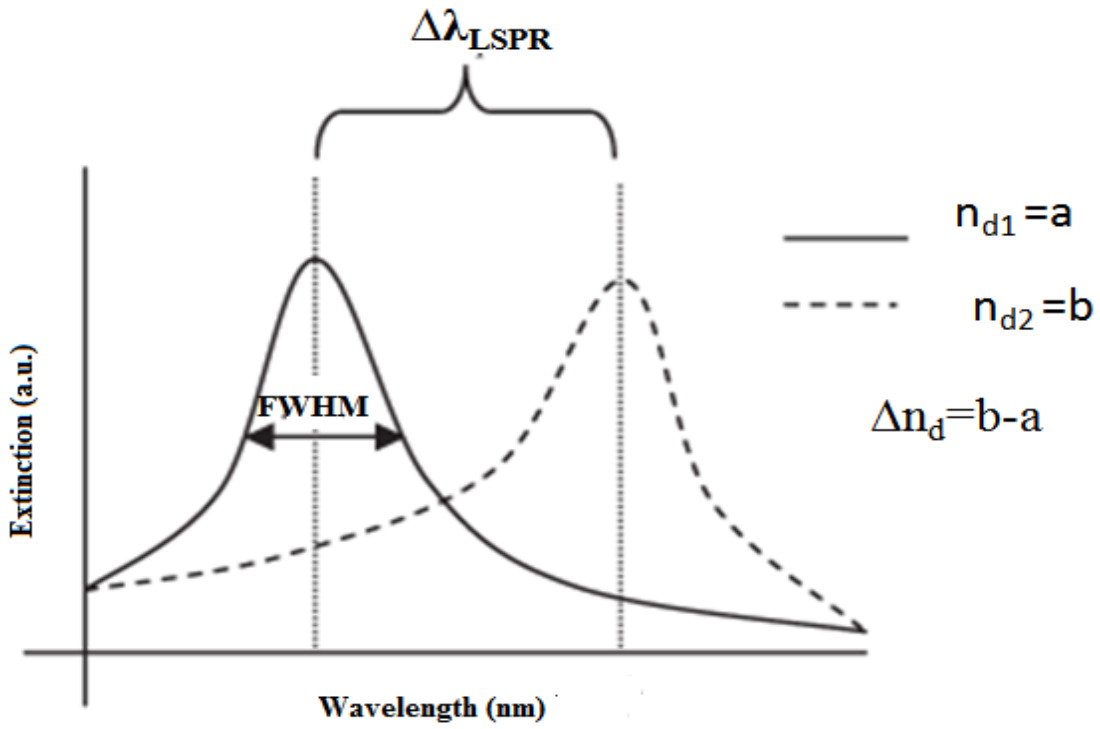

Source: taken from [97]

Table 2 presents FoM values for several nanostructures, indicating that the nanostructure shape is relevant for sensing purpose. One can observe that sharp nanostructures, as triangles, pyramids and stars have a tendency to possess higher FoM values. Moreover, the nanoparticle size plays an important role on FoM values. As the nanoparticle size increases, a red shift and a broadening of the LSPR peak are observed.

Table 2 - Bulk sensitivity (η_b) and Figure of Merit (FoM) of plasmonic nanostructures of various shapes.

Nanoparticles	**Types**	$\boldsymbol{\lambda_{max}}$ **(nm)**	$\boldsymbol{\Delta\lambda_{LSPR}}$ **(nm)**	$\boldsymbol{\eta_b}$ **nm/RIU**	**FOM**	**References**
Au branches	Ensemble	1141	879	703	0.8	[73]
Au nanorice	Ensemble	1600	600	801	1.3	[17]
Au crescent	Ensemble	1795	209	596	2.4	[92]
Au shells	Ensemble	770	350	314	0.9	[98]
Au nanorods	Ensemble	720	125	170	1.3	[99]
Au/AuS	Ensemble	700	400	409	1.0	[89]
Au sphere	Ensemble	530	60	90	1.5	[100]
Au bipyramid	Ensemble	681	52	352	4.5	[101]
Ag cube	Single	510	91	146	1.6	[102]
Ag sphere	Single	520	73	160	2.2	[103]
Ag triangle	Single	760	80	350	4.4	[103]
Ag cube-sub	Single	430	22	118	5.4	[102]
Au star	Single	675	125	238	1.9	[94]
Au pyramid	Single	680	114	221	2.2	[21]
Au rattle	Single	570	52	199	3.8	[104]
Au star	Single	770	124	665	5.4	[94]

2.3.3 Molecular Sensing

Various aspects of LSPR sensor propose its suitability of biomedical and biological assays. LSPR based sensing can be label-free. The response of LSPR sensor can be identified to any molecular attachment to the surface of NPs. The surface sensing enhances with increasing the volume of analyte [105,106].

A phenomenon that explains LSPR based molecular sensing, is the formation self-assembled monolayer (SAM) on the surface of NPs [107]. Campbell and coworkers presented mathematical model for the interpretation of plasmon resonance signals from adsorbed molecular layer on nanostructures [108]. This model can be employed to estimate the adlayer thickness on plasmonic structures, for both SPR and LSPR procedures. The formalism for this model consider the relation of E-field intensity (*I*) and distance (z) from the surface as:

$$I(z) = I_0 \left[e^{-(\frac{2z}{l_d})} \right] \tag{2.16}$$

where l_d the EM field decay length and I_0 is the incident E-field intensity.

On Campbell's model, an effective refractive index is calculated by averaging the refractive index over the depth of layer-medium structure. Therefore, this effective index of refraction can be calculated as:

$$n_{eff} = \frac{\int_0^\infty n(z)\, P dz}{\int_0^\infty P dz} \tag{2.17}$$

where $P = I(z)/I_0$. Therefore,

$$n_{eff} = \frac{2}{l_d} \int_0^\infty n(z) e^{-(\frac{2z}{l_d})} dz \tag{2.18}$$

For monolayer structure, equation (2.18) can be written as:

$$n_{eff} = (n_1 - n_m) \left[1 - e^{-(\frac{2d_1}{l_d})} \right] + n_m \tag{2.19}$$

where n_1 and n_m are the refractive index of adsorbed layer (with thickness d_1) and of surrounding medium, respectively.

Considering the definition of sensitivity (η_b) in equation (2.14), plasmon peak shift (Δλ) can be described as:

$$\Delta\lambda = \eta_b \left[(n_1 - n_m)(1 - e^{-(\frac{2d}{l_d})}) \right] \tag{2.20}$$

Equation (2.20) shows maximum shift for $d >> 1$, if $l_d > 2d$. Also, l_d and n_b both are size and shape dependent. Moreover, the big change in RI value ($n_1 - n_m$) and n_b present higher peak shift.

Campbell's model is not limited to monolayer structure and can be expanded to multilayer structure, as shown in fig. 12 (for bilayers), where the first layer presents refractive index n_1 with adsorption layer thickness d_1, while the second layer has a refractive index n_2 and thickness d_2 , in surrounding medium (n_m).

Figure 12- Nanosphere with a bilayer shell with thickness d_1 and d_2 with refractive indices n_1 and n_2 in surrounding medium (n_m) respectively.

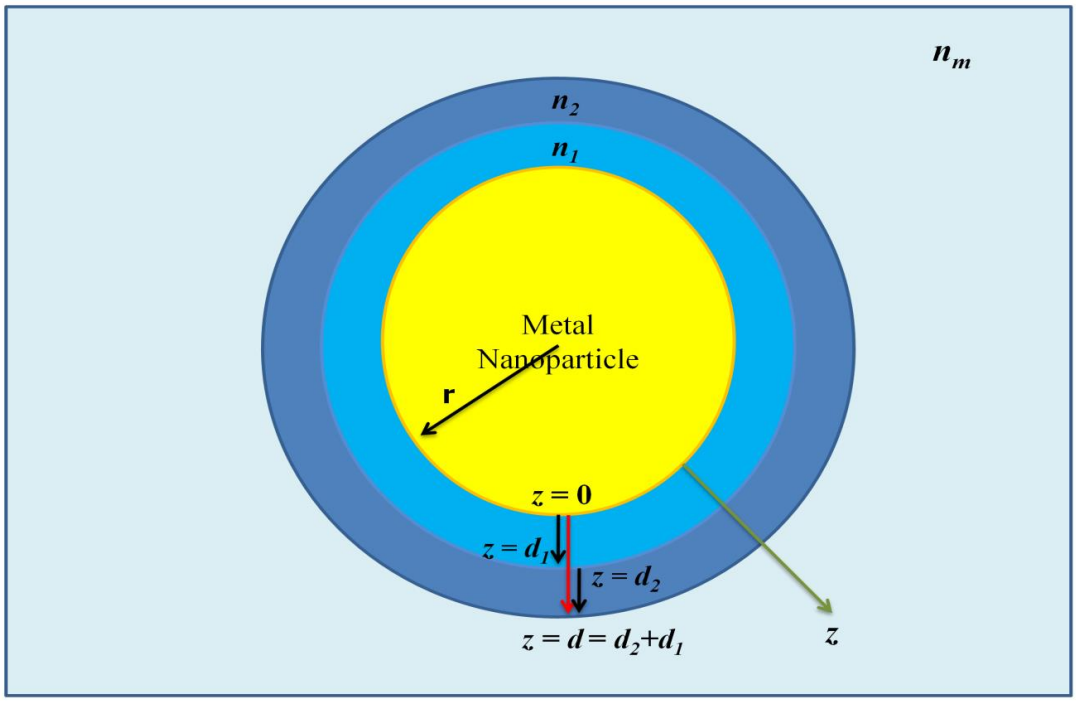

Source: belong to author

Therefore, effective RI can be expressed as:

$$n_{eff} = (n_1 - n_2)\left[1 - e^{-(\frac{2d_1}{l_d})}\right] + (n_2 - n_m)\left[1 - e^{-(\frac{2d}{l_d})}\right] + n_m \quad (2.21)$$

where $d = d_1+d_2$. Therefore, the plasmon peak shift can be expressed as:

$$\Delta\lambda = \eta_b(n_1 - n_2)\left[1 - e^{-(\frac{2d_1}{l_d})}\right] + \eta_b(n_2 - n_m)\left[1 - e^{-(\frac{2d}{l_d})}\right] \quad (2.22)$$

where η_b is bulk sensitivity of bare NP.

It can be seen (equation (2.22)) that if $d >> l_d$, there can be observed maximum shift, while for growing value of l_d, the spectral shift is effectively decreased. For bilayer structure, good condition can be identified for $l_d \leq d$, and the spectral shift show the increasing tendency. However, for $d = 0$, no spectral shift can be observed, and this fact demonstrates the bare particle presence without any adlayer.

The equations (2.20) and (2.22) can also be used to pre-determine the adlayer thickness by employing the values of η_b, l_d and change in refractive index values. These formalisms can also be presented for the quantitative estimates of adsorbate layer in the presence of pre-functionalizing adlayers and for non-uniformities of adlayers thickness.

Table 3 shows the analyte detection limit (density) obtained with NPs of various shapes, size and material composition. Several examples of biological molecules label free sensing can be presented on various concentrations. Usually, on medical diagnosis from micro to nano concentrations are appropriate for detection. NS1 antigen concentrations, for example, in serum samples of patients can be detected during the acute phase of the infection (up to 7 days) which varies from 0.04 to 2 µg/ml.

Table 3 - The study of biological molecules with detection limit using various structures of Au/Ag.

Nanostructures	Biological Molecules	Detection Limit	References
Au NPs	IgG	0.1 nM	[109]
Ag plates	Anti-ADDL	50 nM	[110]
Au NPs	Streptavidin	0.05 µM	[40]
Au NPs	Streptavidin	16 nM	[111]
Ag triangles	Streptavidin	1.0 pM	[112]
Au nanorod	Streptavidin	19 nM in serum	[113]
Au nanorod	IgG	200 nM	[114]
Au nanorods	Anti-rabbit IgG	10.0 nM	[99]
Au NPs	BSA	0.01 µM	[115]
Au@SiO_2	Mellitin	10 nM	[116]
Single Au NP	Streptavidin	50 µM	[117]
Single Au nanorod	Streptavidin	1.0 nM	[118]

2.4 Nanoparticles on Metal-Enhanced Fluorescence

Metal-enhanced fluorescence (MEF) is an emerging tool that achieved high significance over the past decades due to its remarkable applications in biological research, molecular physics and medical diagnostics [119,120]. MEF depends on the couplings of excited state fluorophore with LSPR particles [121,122]. The metal NPs exhibited strong field enhancement at the particle surface. This enhanced near field could increase the fluorescence emission [123]. Furthermore, this phenomenon is characterized by increased quantum yield, spontaneous emission rate and decreased florescent life time [124,125]. For better understanding about this concept, it is informative to observe Jabłoński diagram for fluorophore in free space and in close proximity of plasmonic NP, as shown in figure 13. After absorption of a photon, fluorophore excites and transits to first excited state (S_1). After a short time, fluorophore can emit a photon with radiative rate Γ or return to ground state (S_0) by non-radiative process with decay rate process k_{nr}.

Figure 13- Jabłoński diagram with and without (free space) metal plasmon resonance. E_m and E indicate the excitation rate with metal and in free space respectively. While Γ_m and Γ depicts respectively radiative rate in proximity of metal and in free space, k_{nr} is the non-radiative decay rate.

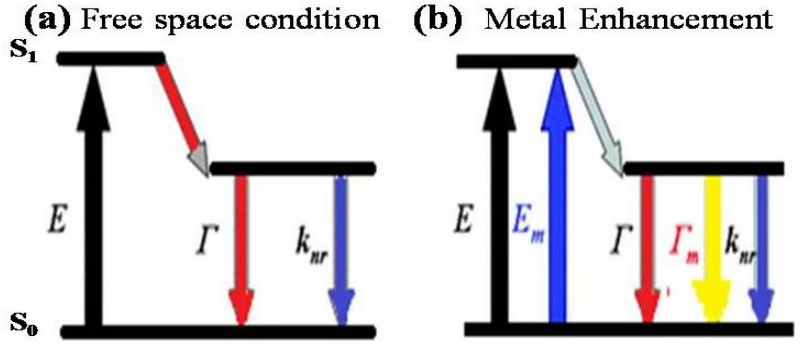

Source: taken from [119].

However, modification of radiative decay rate may undergo when the fluorophore is placed near metallic nanoparticles at a suitable distance. Therefore, NPs can enhance the fluorophore emission by improving excitation emission and changing decay rates. Geddes et al studied the enhancement in fluorophore emission up to 500x due to LSPR of Ag nanostructures grown over glass [123].

2.5 Nanoparticles on Metal-Enhanced Singlet Oxygen Generation

Molecular oxygen is one of the most abundant substances on the earth that is involved in a variety of chemical reactions in biological and chemical systems [126]. The important example among one of its remarkable applications is interaction of O_2 with organic molecules. It is known that the ground state of O_2 is a triplet state [127]. The chemical reactions between triplet O_2 and singlet organic molecule are not allowed by Wigner's spin selection rule to form new singlet. Therefore, at room temperature most chemical reactions do not occur between organic molecule and triplet O_2 because of triplet multiplicity characteristics of O_2 [128]. The highly reactive excited states (singlet) are generated by direct excitation of the ground triplet state ($^3\Sigma$) of oxygen (O_2). Kautsky and co-workers first revealed the existence of singlet oxygen ($^1O_2$) molecule experimentally [129]. There are no further restrictions for $^1O_2$ to react with singlet organic molecules because of its trait of singlet multiplicity [130]. Several applications needed its generation in well controlled manner in human tissues or organic solvents, therefore PS is

involved to generate $^1O_2$ [71, 72].

In Photodynamic Therapy, photosensitizers are involved on $^1O_2$ generation [71, 72]. Multifold PSs should exhibit the characteristics such as (1) high absorption coefficient, (2) excited triplet state of suitable energy, (3) quantum yield of triplet state ($\Phi_T > 0.4$) and (4) long life time ($\tau > 1\mu s$). Table 4 exhibits a few examples of PSs and their quantum yields. In particular, cationic Methylene Blue is a photosensitizer with a high oxygen singlet generation quantum yield, ~0.5 [131]. Moreover, Methylene blue is a FDA-approved anti-microbial agent [132], and a low cost bacteriologic staining for histological applications [133].

Photodynamic therapy can be limited by insufficient generation of $^1O_2$ while reacting with biological cells. It has been demonstrated that LSPR metal field enhancement could improve the generation of oxygen singlet by a photosensitized molecule [121,135]. Due to robust EM fields around metallic NPs close in proximity to PS, a more efficient excitation of the photosensitizer is established [247]. Consequently, NP-PS interaction generated more $^1O_2$ because of increased in triplet excited states yield of PS. Figure 14 presents the mechanism of metal-enhanced singlet oxygen generation (MEO) using modified Jabłoński diagram, showing the excited PS near the plasmonic NP. The PS is excited first from the ground state (S_0) to an excited state (S_n). The enhanced excitation rate (S_n) then relaxes to a lowest excited singlet state (S_1), and enhancing intersystem crossings events.

Table 4- Some examples of PSs and their quantum yields.

PS	Quantum yield (Φ) in H_2O
Rose Bengal	0.75
Methylene Blue	0.5
Eosin Blue	0.52
Fluorescein	0.03

Source: taken from [134]

Figure 14- Jabłoński diagram for the PS and LSPR-based singlet oxygen generation procedure.

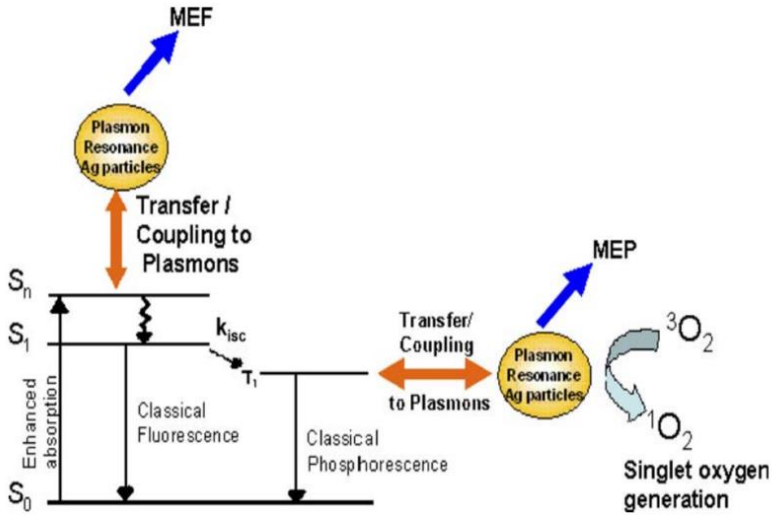

Source: taken from [247]

More yield of $^1O_2$ is subsequently generated due to increasing intersystem crossing and triplet yield [136–138]. The metallic NP-photosensitizer distance is a relevant factor on Metal-enhanced oxygen singlet generation, therefore, particle charge and concentration may play an important role on $^1O_2$ generation procedure. In a solution, electrostatic interaction can aggregate NP and PS, with the same charge signal, leading to resonance energy transfer (RET) that can decrease the production of $^1O_2$. For compounds with opposite charges, RET can be avoided by controlling the NP-PS distance with the solution compounds concentration. In that case, the EM field decay length associated to the NP becomes an important parameter on MEO. A higher MEO value, 3.3x, was observed exploring Rose Bengal photosensitizer on a non-continuous silver island films (2-dimension system) [139]. Moreover, Fales et al. demonstrated metal enhanced $^1O_2$ generation by Methylene-Blue-encapsulated in silica shell of gold nanostars, in breast cancer cells [19]. Although MEO was not quantified by Fales and coworkers, the coated gold nanostars allow SERS detection (diagnostic) and therapeutic action (PDT) in a single platform.

3 ENGINEERING LSPR PLATFORM FOR MOLECULAR BIOSENSING

3.1 Introduction

Gold and silver nanostructures are increasingly receiving attention as an important starting point for label-free sensing. LSPR sensors can be explored as fast, reliable, low-cost, and fairly simple tool for medical diagnosis. Various examples of LSPR biosensors were attributed to the diagnosis of relevant medical disease, as Alzheimer [140], preeclampsia [141], influenza [142], HIV–1 [143], hepatitis–B infections [66] and Dengue virus [144], as well as for intracellular protein sensing [145].

LSPR sensors are mainly based on the identification of plasmon resonance wavelength shift. LSPR peak shift may be induced by changes of the NP surrounding medium or by molecular attachment to the nanostructure surface. On molecular LSPR sensors, when a specific analyte attaches to the surface of NPs, a shift of LSPR spectra may be observed. In particular, chemisorption process can lead to SAM formation on the NP surface [146]. Moreover several important biomolecules, as antibodies, enzymes, DNAs and proteins, have been associated to metallic nanostructures, providing a diversity of LSPR platform for biomedical applications [147].

For nanosphere LSPR-based sensors, the bulk sensitivity, FoM and EM field decay length are dependent of the NP particle radius [147]. Therefore, the plasmon peak shift of LSPR molecular sensor should also be dependent of the nanoparticle size. To develop an efficient LSPR molecular sensor, an evaluation of $\Delta\lambda$ as a function of the NP size and adsorbate molecule layer thickness are required. Whereas several good reviews on LSPR sensors can be found in the literature [3,148–151].

In this chapter, crucial parameters that rule the LSPR molecular sensor performance, as Figure of Merit, bulk sensitivity and electromagnetic field distribution around the NP and their dependence with nanostructure size and material composition (gold and silver) are evaluated. Moreover, this chapter provides insights on the LSPR behavior due to adsorption of molecules layer on a NP surface. Campbell's model is evaluated exploiting a NP size-dependence approach, establishing a new paradigm on engineering LSPR biosensor.

3.2 Materials and Methods

3.2.1 Simulations Analyses

Computational simulations were used to describe the interaction of light with the nanoparticle, and therefore, leading to the understanding of the behavior of crucial parameters that govern the LSPR molecular sensor performance. Here, Finite Element Method (FEM) was performed using COMSOL multiphysics, to determine the scattered field distributions and, therefore, the NP extinction cross-sections. In FEM simulation, the nanoparticle surface was divided into small tetrahedral mesh elements with size 'finer'. Additionally, isotropic perfectly matched layer (PML) around the nanoparticle, was introduced to avoid any reflection artifacts on the simulation. The amplitude of the background-oscillating field was set to $1Vm^{-1}$.The values of the metal complex (real and imaginary) dielectric functions for Au and Ag were obtained from literature [152].

3.2.2 Experimental setup

UV–Visible extinction spectra, from 350 to 800 nm, were obtained using a spectrophotometer from Ocean Optics (HR+4000) with Halogen-Deutrium light source and two fibers. Figure 15 demonstrates the complete set up to measure the LSPR extinction spectrum of metallic nanoparticle in colloidal suspension.

Figure 15- The experimental set up to determine the extinction spectrum of colloidal nanoparticles

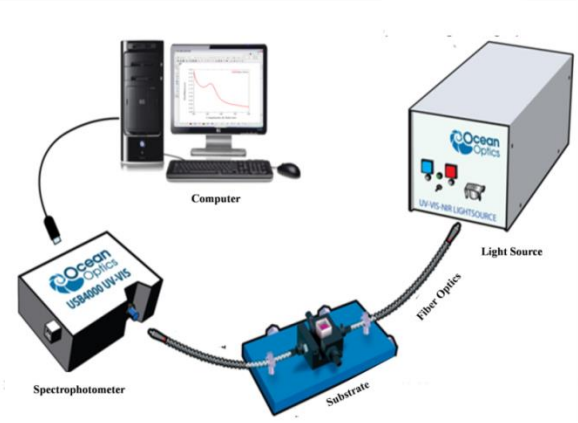

Source: taken from [153]

3.3 Results and Discussion

LSPR peak position is solved not only by the real part ϵ_r of NP permittivity, but also by the RI of the local medium. On a refractive index based LSPR sensors, bulk sensitivity indicates how LSPR peak position moves with changes on the RI of the local medium. Figure 16 shows the theoretical and experimental analyses of the LSPR spectral peak position of 25 nm radius silver and gold nanosphere in several surrounding media, with different RI values.

The experimental spectral analysis of the colloidal Au and Ag nanospheres were performed in different solvents e.g. water (1.33), acetone (1.36), tetrahydrofuran (1.407), dimethylformamide (1.43), polyethylene glycol-300 (1.465). LSPR peak position is linearly dependent on the refractive indices of surrounding medium as shown in figure 16 (a) for Au and Ag (fig. 16(b)) nanospheres. For gold nanosphere, with radius of 25 nm, LSPR peak wavelength can shift from 527 to 539 nm with RI increasing from 1.33 to 1.46, as shown in figure 16 (a). Experimental and theoretical values for the bulk sensitivity of gold spherical nanoparticles were identified as 78 nm/RIU and 83 nm/RIU, respectively. The small difference (6%) on the experimental and theoretical results indicate the good performance of the simulation method explored. The obtained experimental and theoretical bulk sensitivity values of silver nanospheres were 176 nm/RIU and 163 nm/RIU, respectively (fig.16 (b)).

Figure 16- LSPR peak shift of gold (a) and silver (b) 25 nm radius nanospheres on changing the refractive index of the surrounding.

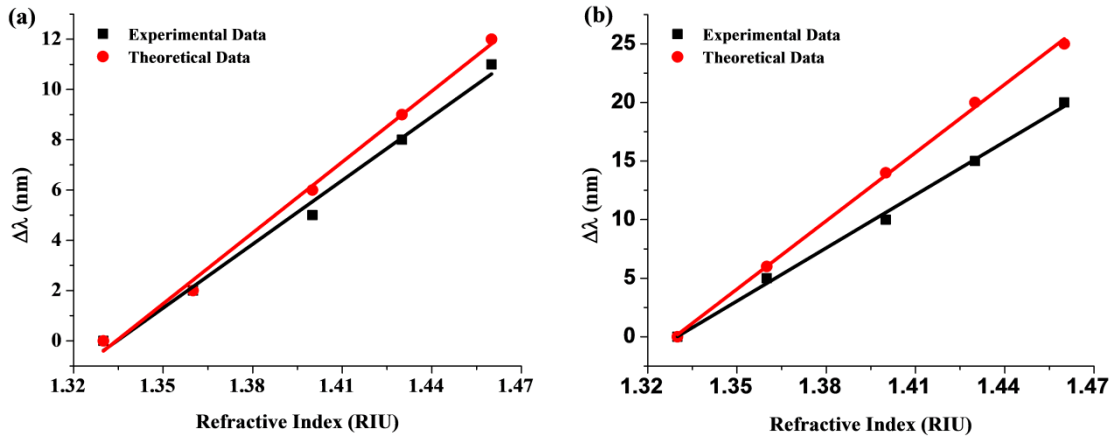

Source: belong to author

Table 5 presents the bulk sensitivity values of Au or Ag nanospheres for radius 25 nm, is in good numerical agreement. The reason in the bulk sensitivity differences of Au versus Ag nanospheres is due to their materials dielectric functions. It is evident that value of ϵ_i of silver is smaller than that of gold, in the visible band, resulting higher scattering efficiency and less plasmon damping. This fact makes silver more desirable over gold for sensing applications. The effects of NP size on the bulk sensitivity and FoM determining nanoparticle sensing platform, can be observed in fig 17. Ag and Au nanospheres with radii 5-50 nm were analyzed. A theoretical analysis of the bulk sensitivity as function of the NP size (figure 17(a)) indicates a nonlinear behavior for the η_b values. As the radius of the nanoparticles enhance, an increase of nanosensor bulk sensitivity from 50 to 182 nm/RIU for gold, and 103 to 284 nm/RIU for silver nanospheres were observed. As NP radius increases, the sensing area also increases, rising the sensitivity of the nanostructured platform.

Moreover, for small particle (r < 10 nm) the absorption process mainly determines the light-NP interaction. Scattering phenomenon grows by increasing the particle size (r > 10 nm). For AuNP platform, with 20 < r < 40 nm bulk sensitivity is highly dependent on the nanostructure size. It can be seen (fig. 17) that bulk sensitivity of nanospheres for Ag is highly influenced on size than the Au. The nonlinear behavior of the bulk sensitivity, shown in figure 17(a), can be empirically described as:

$$y(r) = A + \left[\frac{B}{1 + e^{\frac{(r-C)}{D}}}\right] \tag{3.1}$$

where A, B, C and D are constants and *r* is the radius of nanospheres.

Table 5- Bulk sensitivity of gold and silver nanospheres (25 nm radius).

Material	**Experimental η_b (nm/RIU)**	**Theoretical η_b(nm/RIU)**
Au	78	83
Ag	176	163

Source: belong to author

As the Ag nanosphere radius increase, the FWHM increase due radiation damping factor [33]. Therefore, FoM of Ag nanospheres decrease as the particle size grow, as shown in figure 17(b) Albeit, the ϵ_i value of Ag dielectric function is less than that of Au across visible band, therefore less damping occurs, resulting narrow FWHM (fig. 17(a) and (b)) and high values of FoM for silver particles. This is an advantage of Ag over Au nanospheres in practical biosensing applications.

The calculated value of FoM (3.8) of silver nanospheres (r = 10 nm) is higher than the reported values of more complex shapes, such as single Au nanorod (1.3) [34], Au nanostar (1.9) [35], Au pyramid (2.2) [8] Ag nanocube (1.6) [36]. The FWHM of gold spectrum is not so affected by increasing the particle size, as compared to Ag nanoplatform. Therefore, the FoM behavior of AuNP is mainly determined by bulk sensitivity changes. On molecular LSPR sensing, the EM field decay length is an important parameter to be considered. As l_d increases the LSPR wavelength shift decreases, due to a molecular bilayer adsorption on a metallic NP surface, as indicated in Campbell's model in section 2.3.3 (equation 2.20). Figure 18(a) shows the EM field decay of an isolated silver nanosphere (r = 5 nm) in homogeneous surrounding medium (n = 1.33).

Figure 17- The bulk sensitivity of gold versus silver nanospheres as a function of particle radius (a) and their respective figure of merit (b).

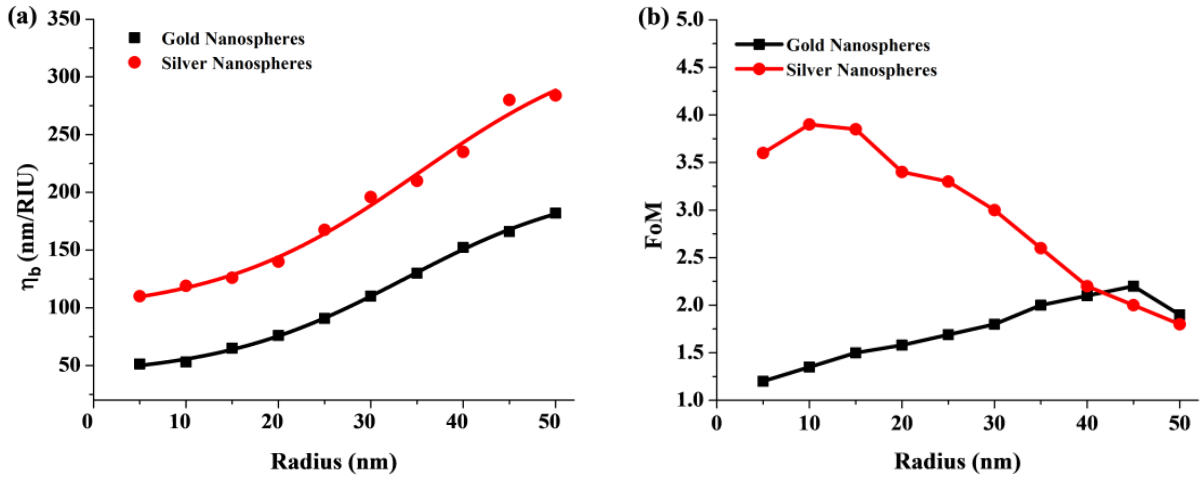

Source: belong to author

The field decay length can be determined by fitting a single exponential on the field intensity distribution, as proposed by Barbillon et al [154]. Figure 18 shows that EM field decay length increases linearly as the NPs radius grows.

For AgNPs with 2.5 < r < 50 nm, the Ag l_d values can be described by a linear fitting as:

$$l_d = G \times r + H \tag{3.2}$$

where G (slope) and H are constants (fitting parameters).

Figure 18(b) shows that the EM field decay length of Au or Ag nanospheres can reach few tens of nanometers (at resonance), indicating that LSPR sensors can be highly selective for thinners adsorption layers. While for surface plasmon resonance thin film based sensors the evanescent field decay length is of the order 200 to 300 nm. Campbell's model (section 2.3.3) shows that LSPR peak shift increases by increasing the η_b values and reducing l_d. As η_b and l_d are dependent on the nanostructure size, the $\Delta\lambda$ of a LSPR sensor should also be conditioned to the nanosphere radius.

Figure 18- The electric field decay with respect to distance from Ag nanosphere (r = 5 nm) surface (a) and l_d values for Ag or Au nanospheres with increasing particles radii (b), in homogeneous surrounding medium (n = 1.33).

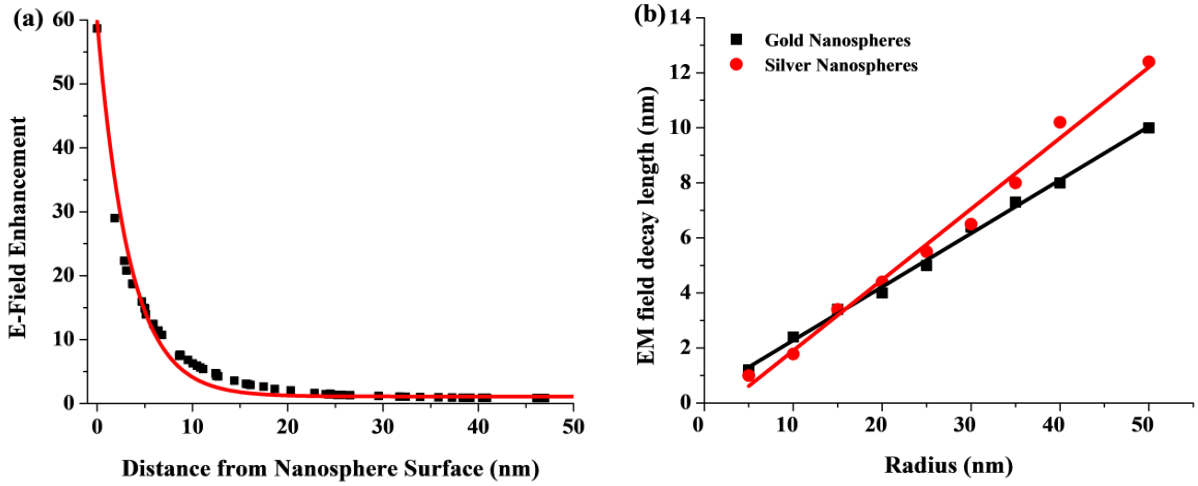

Source: belong to author

Moreover, Campbell's model also indicates that by increasing the adsorbate layer thickness the LSPR peak shift increases. Figure 19 shows the behavior of LSPR peak shift of an Ag nanosphere sensing platform for different nanostructure size, calculated from equations (2.20), (3.2), and (3.3). From figure 19, we assumed that a single monolayer, with refractive index equal to 1.47 and different thickness (0.5, 1.0, 1.5, 2.0 and 3.0 nm), adhered on the NP surface.

For small particles ($r \leq 5$ nm), LSPR peak is determined by absorption process, field decay length is limited to few nm and η_b values are around 50 nm/RIU for gold and 103 nm/RIU for silver. Thus higher values for $\Delta\lambda$ were observed, about 12 to 17 nm shift for AgNPs and about 5 to 8 nm for AuNPs. For larger particles, the l_d values increase, increasing the exponential factor on Campbell's model and therefore reducing $\Delta\lambda$ (for $5 \leq r \leq 20$ nm). Albeit, for particles with radius bigger than 25 nm, as NP size increases the bulk sensitivity values considerably increase (fig. 17), and therefore an increase of the LSPR peak shift is observed in figure 19. Moreover, figure 19 show that $\Delta\lambda$ reduces for particles with radius bigger than 45 nm, due to the fact that bulk sensitivity growth is also reduced (fig. 17). Figure 19 also indicates that, on engineering a LSPR platform, two nanoparticles size range should be considered (r about 5 nm or 40 nm radius). Figure 20 shows the behavior of LSPR peak shift of 5 nm and 40 nm metallic (Ag and Au) nanospheres for molecular sensing platform, calculated from equation (2.20). On figure 20, it was assumed that single dielectric shell, with refractive index equal to 1.47 and shell thickness varying from 1 to 10 nm, shielded the NP surface, in water.

Figure 19- The LSPR spectral peak shift ($\Delta\lambda$) as a function of Ag (a) and Au (b) nanoparticles radii by increasing the adsorbate layer thickness, with n_{ads} = 1.47.

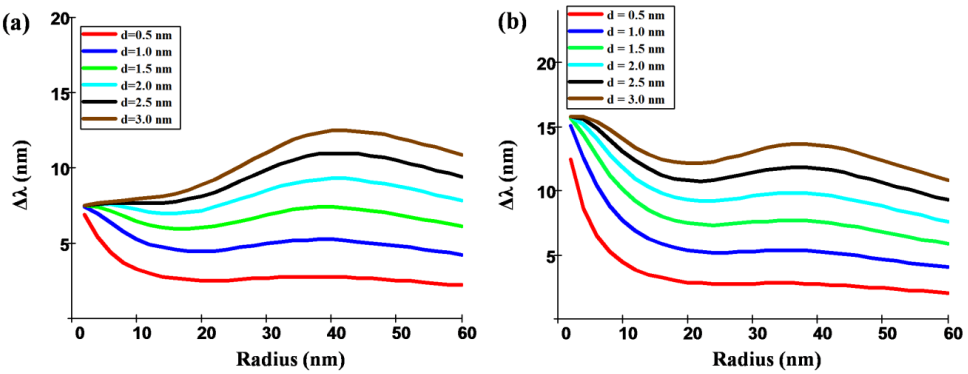

Source: belong to author

By the increasing adsorbate shell thickness, the LSPR peak shift increases, for 40 nm NP radius. Albeit, for 5 nm NP radius the changes on the LSPR spectral shift is not significant (<2 nm), by growing dielectric shell. Moreover, the slope of the graphics in figure 20 indicates that for 40 nm NP radius, small changes on the dielectric shell thickness can induce significant changes on $\Delta\lambda$. For instance, an increase of the shell thickness from 3 to 6 nm can induce ~ 12 nm (for silver) and ~ 6 nm (for gold) shift of the LSPR peak wavelength. Many groups have been working on different methodologies to prepare nanoparticles of various structures, leading to high plasmonic fields and tunable plasmon spectrum, from visible to near infrared band. In particular high bulk sensitivity and FoM values were measured for non-spherical structures, like nanorods [34], nanopyramids [21], nanocubes [36] and nanostars [35], particles.

The proposed approach can be extended to engineer the efficiently use of different nanostructures on molecular biosensing. On medical diagnostic, metallic nanoparticles are base-structures to the engineering of LSPR biosensors. In particular, LSPR label-free immunoassay is launched by functionalizing the NP with an antibody or antigen, by the use of a ligand molecule, as cysteine or cysteamine. Usually, ligand molecules present a thiol functional group that attaches to the metallic nanoparticle surface, and an amine group ($–NH_2$), which allows binding to antibodies/antigen carboxyl group.

On engineering a high performance LSPR biosensor, the length of the binding molecules (ligand, antibodies and antigen) should be estimated, and a realistic value of the adsorbate shell layer should be used on Campbell's model. For instance, cysteine and cysteamine (ligand molecules) are no longer than ~1 nm [19]. Moreover, the refractive index of the adsorbate shell layer should also be appraised. Regardless the different nature of binding molecules, an effective refractive index value of 1.47 RIU can be considered for molecular shell layer on an immunoassay LSPR platform [22]. The Laboratory of Biomedical Optics and Image of UFPE has demonstrated the use of metallic nanoparticle on the development of a LSPR biosensing platform for *Candida albicans* antigen identification. All the three steps assembling of sensing platform and identification of *C. albicans* antigen are shown in figure 21(left), following the published manuscript (doi: 10.1117/1.JNP.12.033003) by Farooq et al. (Appendix B).

Figure 20- The study presents the LPSR spectral shift upon the dielectric shell thickness layer for gold (a) and silver (b) nanospheres.

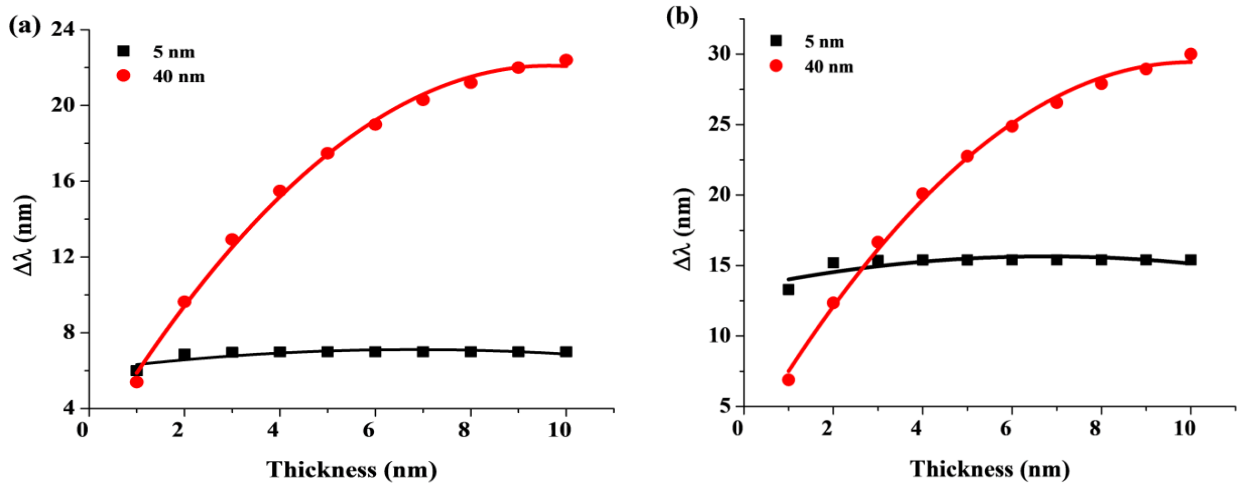

Source: belong to author

Figure 21 (right) shows the optical extinction spectrum of the NPs on the glass slides platform starting, with an LSPR peak at 415 nm. The use of cysteamine as a ligand on the NPs led to a LSPR peak shift (red line) 419 nm. The platform extinction spectrum, with the immobilization of *Candida albicans* antibodies (200 ng/mL) and glycine, shows with another LSPR peak shift (blue line) at 424 nm.

The use of antibodies solution with different concentrations induced changes on the extinction spectrum. The inset of figure 21 indicates the LSPR peak wavelength of the NP on glass slide after antibodies immobilization. The increase of antibodies solution concentration allows an increase of the number of immobilization sites on the NPs surface, and therefore a longer spectrum shift. Another significant spectrum shift was observed when *Candida albican* antigen was identified by the platform (black curve in figure 21). A 25 nm red-shift indicating an antigen-antibody binding was observed when a 200 ng/mL solution of antigen were identified on the sensing platform.

Figure 21- Schematic diagram of LSPR platform for immunoassay *C. albicans* sensor (left), and LSPR extinction spectrum of the biosensing platform (right). The inset shows the LSPR peak shift for different antibody concentrations.

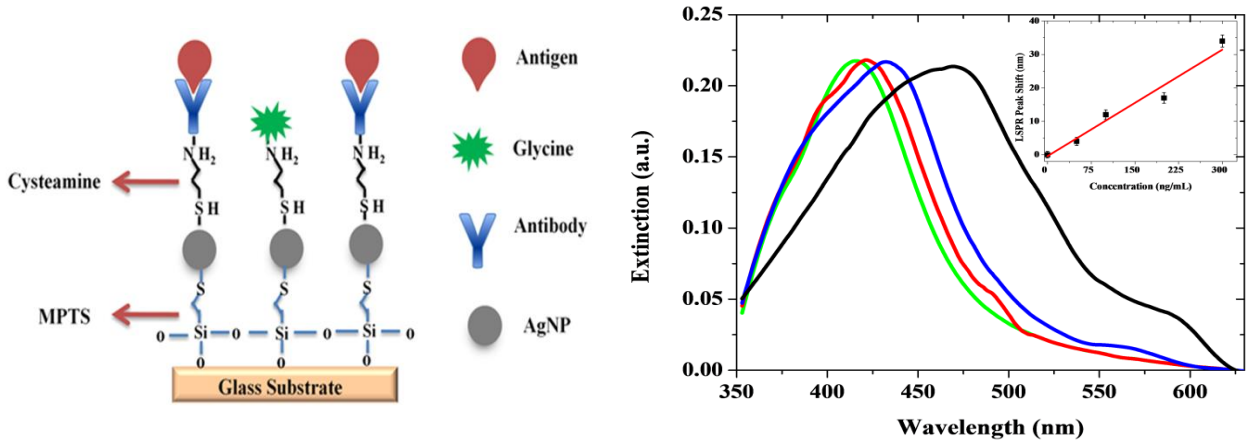

Source: belong to author

Moreover, the choice of the nanostructure with best performances is therefore dependent on the refractive index and effective thickness of the adsorbate molecules, LSPR sensing platforms are being extensively explored on biomedical diagnostic devices.

In this chapter, we discussed the development of a LSPR sensor on theoretical evaluation of sensing platform performance. FEM simulation approach was employed on the assessment of the LSPR spectra and leading to identification bulk and molecular sensitivity as a function of NP size. Our sensing platform was able to identify small concentration (50 ng/mL) of *C. albicans* antigen in a solution dropped on the platform. The results indicated the viability of exploring LSPR effects on *C. albicans* antigen biosensor.

4 OPTICAL PROPERTIES OF SILVER NANOPLATES FOR BIOMEDICAL APPLICATIONS

4.1 Introduction

Metallic nanostructures are an attractive option for biomedical applications [36–39]. The NP shapes, size, and material composition tailor LSPR applications on medical therapy and diagnosis procedures. Many groups have been working on different methodologies to prepare nanoparticles of various structures, leading to high plasmonic fields and tunable plasmon spectrum, from visible to near infrared band. It has been reported that colloidal chemical method offers particular control over size, shape and structure [26,155].

In this chapter, we investigate the optical properties of Ag nanotriangle (nanoplate) and evaluate its potential to be used on LSPR biosensing and on PDT. The analysis, based on experimental results and simulation approach, focus on the assessment of the LSPR spectrum and spatial distribution of the electromagnetic field enhancement near metallic nanoplates, with different altitude lengths and thickness.

Crucial parameters that improve the LSPR sensor performance, as sensibility and Figure of Merit, are identified and evaluated. The coupling of Ag nanoplates (AgNPls) with Methylene Blue (MB) photosensitizer is also appraised, and metal-enhanced oxygen singlet (MEO) is observed and quantified.

4.2 Methods and Materials

Ag nanotriangles sample with polyvinylpyrrolidone (PVP) stabilizer was obtained from nanoComposix. The specified average triangle altitude length of a nanoCompix nanostructure was ~57 nm and the extinction LSPR at 693 nm. Transmission electron microscopy (TEM) images of the nanoplates were obtained using MORGAGNI 20 at 100 kV. The samples transmission and emission spectrum, from 300-1100 nm, were obtained using an Ocean Optics spectrophotometer (HR +4000) and placing the samples in quartz cuvettes of 1 cm width. Fiber bundles were used to guide light from a Halogen-Deuterium light source to the sample and to send light from sample to the spectrophotometer.

On the LSPR bulk sensing experiments, the following solvents were explored: aceton, and, isopropyl alcohol from Quimica Moderna; tetrahydrofuran (THF), dimethylformamide (DMF), glycerol, and dimethyl sulfoxide from Sigma Aldrich; and poly ethylene glycol (PEG) from Chem Buyers.

Methylene Blue, obtained from Merck, was used as a photosensitizer molecule, on the generation of singlet oxygen. Green Reagent (GR), from Thermofisher, was explored as the singlet oxygen sensor. The sensor stock solution was prepared adding 100 µg of GR in 330 µL of methanol solution. The 500 µM of GR was kept under dark at a temperature below 10°C. The GR has an optical excitation maximum at 504 nm and emits green light with maximum wavelength at 525 nm. A He-Ne laser (at 632.8 nm) was used for the photosensitizer (MB) excitation. At the sample, the laser power was 1.2 mW with the spot size ~40 mm.

Finite Element Method (FEM) based simulations were performed using COMSOL Multiphysics. Simulations were used to determine the frequency domain scattered field distribution close to the AgNPl. On the simulation, the nanoplates were considered to equilateral triangles. The simulations explored nanotriangles with altitude length, D, from 10 to 60 nm. Moreover, the nanostructure thickness varied from 1 to 20 nm. On the numerical analysis, the electric field amplitude was set as 1V/m. For all AgNPls size evaluated, different tetrahedral meshing was explored. A perfectly matched layer (PML) was used around the silver plate to minimize reflection artifacts. The radius of PML spherical shaped model was 500 nm and layer thickness was 150 nm with triangular meshing. The data for real and imaginary refractive index dispersion is obtained from Johnson and Christy literature [58].

4.3 Results and Discussion

Figure 22(a) shows UV-visible extinction spectra of AgNPls colloid obtained theoretically and experimentally. A LSPR peak at 693 nm (measured) is due to plasmon dipole and a shoulder peak at 420 nm is associated to quadrupole resonance. The measured plasmon spectrum, appears much broader than the simulated result (60 nm altitude length, 10 nm thickness), indicating that the colloid is composed of AgNPls with different sizes. Figure 22(b) shows TEM images of silver nanoplates.

Figure 22- Experimental (solid line) and theoretical (dash-dotted line) extinction LSPR spectra of AgNPls in water (a). TEM images of silver nanoplates (b). The inset shows single nanoplate with ~57 nm altitude length.

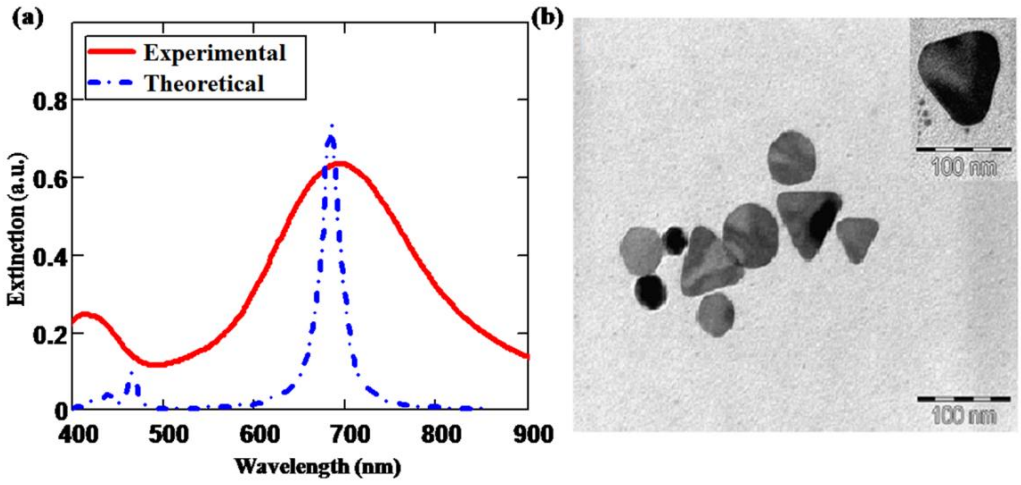

Source: belong to author

A high inhomogeneous shape/size distribution of AgNPls can be observed on figure 22(b). The inset of figure 22(b) shows single AgNPl with triangular shaped and 60 nm altitude length.

4.3.1 Effects of Nanoplate Dimensions on LSPR

Extinction spectra of nanoplates were also investigated with respect to the nanotriangle altitude length and thickness. Figure 23(a) depicts that when the altitude of AgNPls are increased from 10 to 60 nm, while keeping the thickness constant (10 nm) in surrounding medium (n = 1.33), the LSPR modes appear in the visible and near infrared spectral regions. The prominent modes are attributed to dipole resonances. Figure 23(a) shows that there is continuous red-shift in LSPR peak positions from 475 to 685 nm, with the increase of the nanoparticle altitude length.

It is found that FWHM increase continuously from smaller to larger Ag plates. Moreover, there is a linear relation between the plasmon peak shifts (dipole mode) and the nanoplates altitude length, as presented in figure 23(b). By changing the AgNPls thickness (t), significant effects on the extinction spectrum of the plates were observed, as shown in figure 24.

Figure 23- Simulated LSPR extinction spectra of AgNPls with different altitude lengths, t = 10 nm and n = 1.33 (a). Plasmon peak positions for various AgNPls altitude lengths (b).

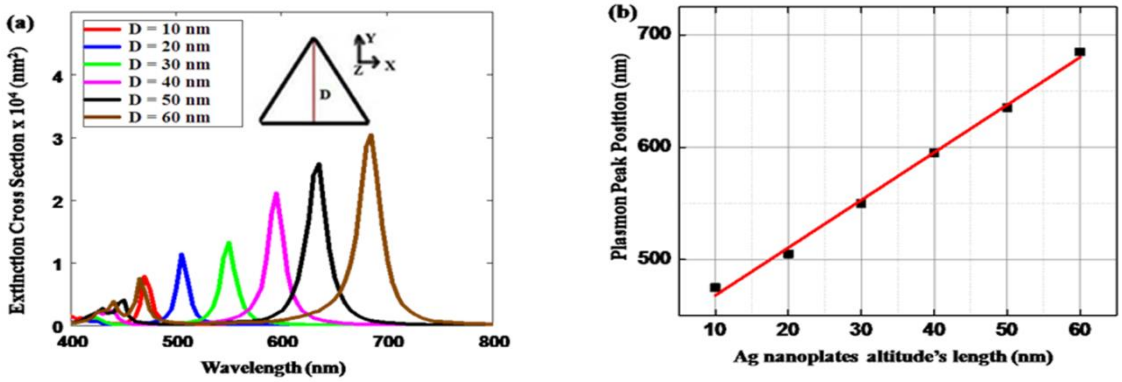

Source: belong to author

Figure 24- Simulated extinction spectrum of AgNPls with different thickness, D = 60 nm and n = 1.33 (a). Plasmon peak positions for various AgNPls thickness (b).

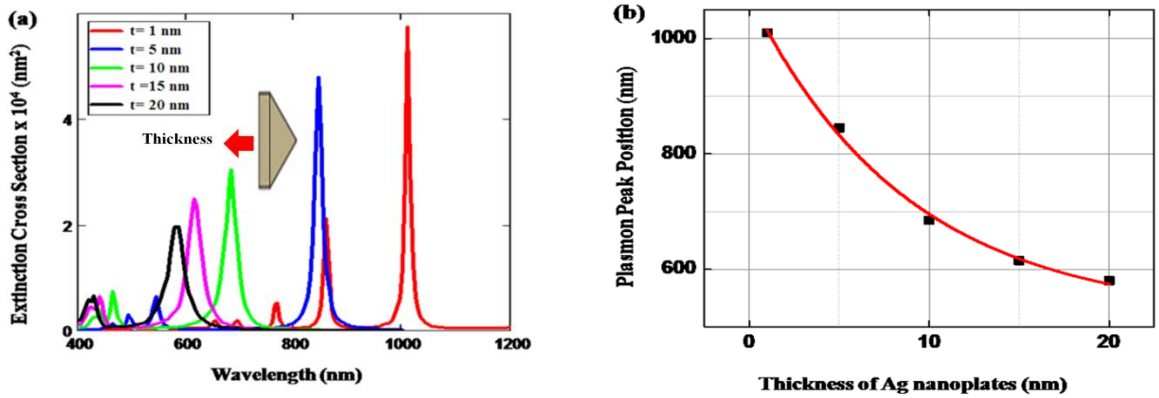

Source: belong to author

By reducing the plates thickness from 20 to 1 nm. (AgNPl with 60 nm altitude length), the plasmon spectra can shift from visible (580 nm) to near infra-red (1010 nm), as shown in figure 24(a). The simulations also indicate that the FWHM of the extinction spectrum decrease with respect to the reduction of AgNPls thickness. For 1 nm thick, AgNPl the extinction spectrum presents a sharp peak, with FWHM ~7 nm. For 20 nm thick nanoparticle, around 37 nm FWHM was observed. The evaluation of the field distribution close to the NP surface can attribute to various applications with AgNPls, such as SERS, fluorescent based imaging, PDT, and biosensing. Figure 24(b) indicates that spectral shift due to changes on the NP thickness are more

noticeable on thinner particles (t<10 nm). For larger thickness, the influence of NP thickness on LSPR shift is weaker. Tuning the AgNPl's altitude and thickness, and therefore controlling its optical features from visible to NIR, could potentially contribute to harvest chemo-sensors [156]. Not only LSPR spectrum, but also the electrical field distribution around the NP is controlled by the nanostructure size. Figure 25 displays the calculated normalized electric field distribution ($|E/E_0|$) around the single Ag nanoplate, with D = 60 nm and t = 10 nm, in a homogeneous surrounding medium (n = 1.33). As depicted in figure 25(a), the field enhancement is highly localized at the corners or tips of AgNPl. For dipole plasmon mode (685 nm) the strong field distribution is observed at the tips/corners of the nanoplate, while for quadrupole mode (465 nm) the field is spread to the sides of particle. Figure 25(c) shows the field amplitude decaying as a function of distance from the nanoplates tip surface. Field enhancement is highly perceived for 685 nm than for 465 nm wavelength. Indicating that the dipole mode could be more sensitive to the environment local changes.

Figure 25- The normalized electric field distribution $|E/E_0|$ of AgNPls solved with FEM analysis at dipole (685 nm) resonance (a) and quadrupole (465 nm) resonance (b). The EM field decay with respect to distance from AgNPl surface in water as surrounding medium (c).

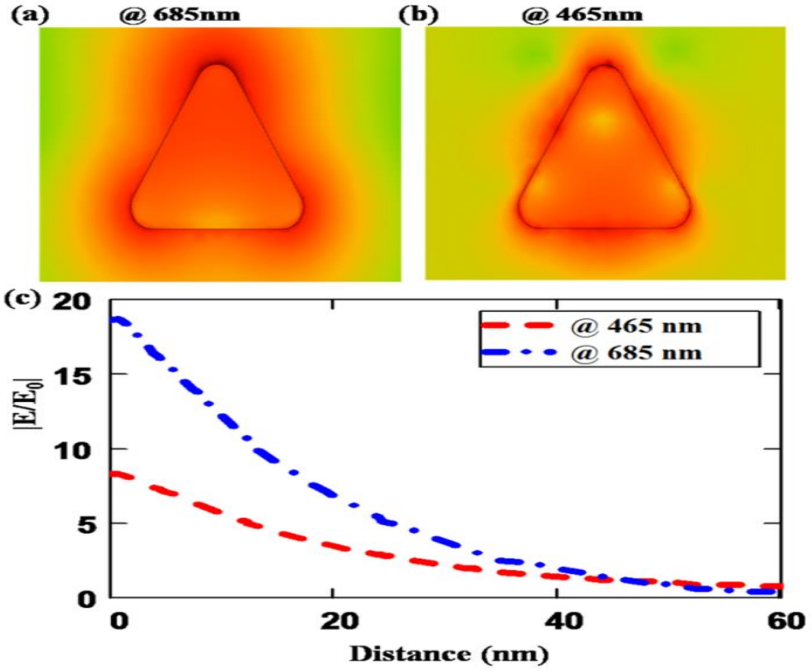

Source: belong to author

Moreover, 45 nm away from the NP surface 2-fold increase of the electric field was observed for the dipole mode. Electric field enhancement around Ag plates, with various altitude lengths, was numerically computed with respect to distance from the plate surface. Figure 26 shows the $|E/E_0|$ distribution around AgNPls with different altitude lengths (D = 10, 20, 30, 40, 50 and 60 nm) at their respective resonances wavelength (λ = 470, 505, 550, 595, 635, 685 nm). The field strength reduces by increasing the distance from the nanoplate surface. Far from the surface (>10 nm), field enhancement of the dipole modes is higher for larger NPs. The extension of the electrical field enhancement can be quantified by the EM field decay length, l_d, define as the distance that the magnitude of the electric field has decayed to 1/e of its surface value.

Figure 26- Simulated normalized plasmon field strength of silver plates with different sizes (D = 10, 20, 30, 40, 50, 60 nm; t = 10 nm), in water (n = 1.33). The simulations used the corresponding plasmon peak wavelengths of each nanoplate.

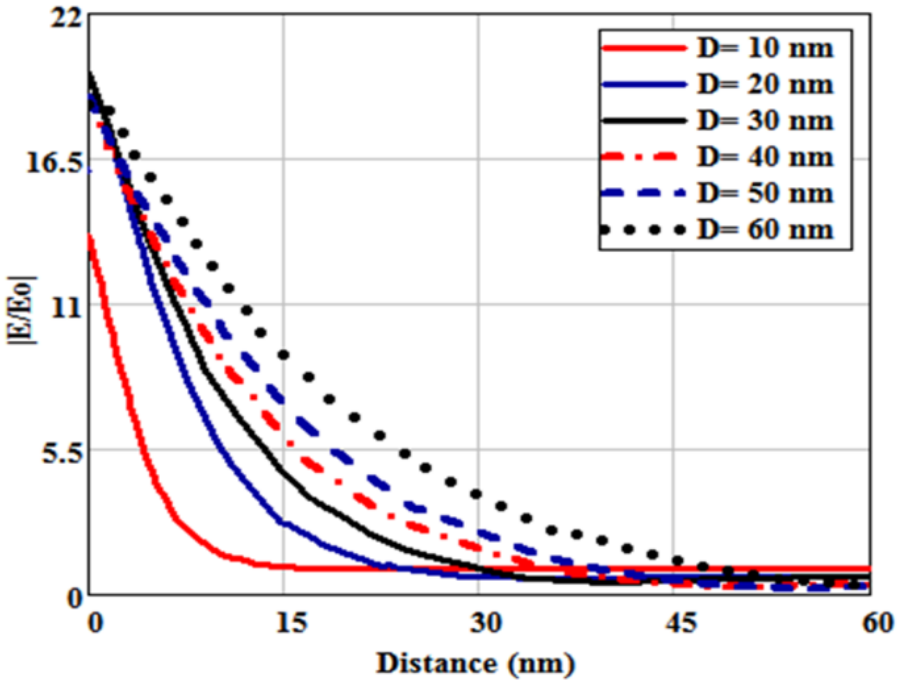

Source: belong to author

Table 6 elucidates the l_d values of Ag nanoplates with different altitudes (D = 10, 20, 30, 40, 50 and 60 nm) and t = 10 nm, in a homogeneous surrounding medium (n = 1.33), under resonant excitation of dipole plasmon modes. EM field decay length has a particular importance on molecular sensing [157]. The l_d values depend on shape, size and composition of the nanostructures. As the nanotriangle altitude increases, the EM field decay length grows. The EM field enhancement due to localized plasmon resonance extend to several nanometers, while the EM decay length value for surface plasmon resonance is about 200–300 nm [158].

Resonant excitation of plasmon modes lead to electric field enhancement close to AgNPls surface. However, significant changes on the field strength and distribution are observed when the excitation wavelength is scanned out of the plasmon peak. Figure 27, shows the $|E/E_0|$ distribution near AgNPl's tips (D = 60 nm and t = 10 nm) at different wavelength (λ = 685, 664, 634 nm). At the AgNPl surface, the electric field enhancement at 685 nm (resonance wavelength) is approximately 1.86 times higher than to 664 nm excitation, and 2.92 times higher than to 634 nm.

Table 6- EM field decay lengths of Ag nanoplates with different altitude lengths (D).

Altitude lengths (nm)	EM field decay length (nm)
10	5.10
20	9.11
30	11.10
40	13.21
50	15.10
60	18.22

Source: belong to author

Figure 27- Simulated normalized plasmon field strength of silver plates with D = 60 nm and t = 10 nm, at different excitation wavelengths (λ = 685, 664, 634 nm), in a homogeneous surrounding medium (n = 1.33).

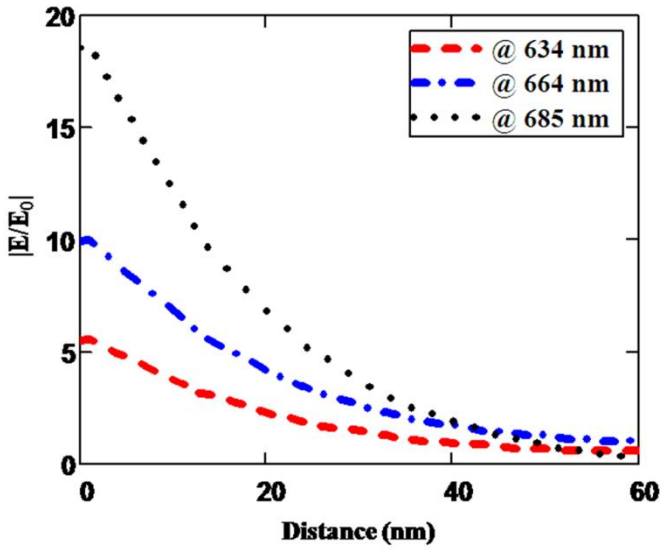

Source: belong to author

As the excitation electric field wavelength moves away from the plasmon resonance peak, the field enhancement becomes less effective. Moreover, far from the surface field enhancement of dipole modes are weaker. At 20 nm away from the AgNPl, the field enhancement at 685 nm is 1.6 times greater than to 664 nm, and 5 times more effective than to 634 nm. Besides, the value of EM field decay length at dipole resonance (685 nm) is higher (18.22 times) than to field decay length (12.4 times) under the excitation at 634 nm.

4.3.2 Nanoplate for Sensing

LSPR based sensing has been widely explored on the identification of refractive index (RI) changes of local medium [90,148]. For LSPR based sensors, bulk sensitivity is termed as the variation of LSPR peak position with respect to the change in RI unit (RIU) of the medium [159] and its formalism is already described in section 2.3.1. Figure 28(a) shows the measured LSPR extinction spectra of Ag plates (D = 57 nm, t = 10 nm) colloid in water (n = 1.33) and in dimethyl sulfoxide (n = 1.479). The increase of the medium RI induces 64 nm red-shift of the dipole plasmon peak, from 693 to 757 nm. A smaller red-shift (20 nm) of the quadrupole plasmon peak

is also shown in figure 28(a). The higher dipole shift is attributed to the increase of plasmon field enhancement due to sharp tips [160].

Changes of the RI of the AgNPl environment may induce shifts of the LSPR spectrum. Figure 28(b) shows the measured relative spectral shift of plasmon peak wavelength, $\Delta\lambda_{LSPR}$, of the AgNPls with acetone (n = 1.36), isopropyl alcohol (n = 1.38), tetrahydrofuran (n = 1.40), dimethylformamide (n = 1.43), poly-ethylene glycol (n = 1.46), glycerol (n = 1.47) and dimethyl sulfoxide (n = 1.479). On the evaluation of the relative spectral shift of plasmon peak wavelength, water was chosen as the reference medium, and therefore, $\Delta\lambda_{LSPR} = \Delta\lambda_{LSPR}(\text{solvent}) - \Delta\lambda_{LSPR}(\text{water})$. It was observed, in figure 28(b), that $\Delta\lambda_{LSPR}$ grows linearly with the increase of environmental medium RI, with $R^2 = 0.99$. By measuring the slope of the linear fitting in figure 28(b), a high AgNPls colloid bulk sensitivity value of 406 nm/RIU was found. The η_b value for AgNPls colloid is greater than the sensitivity value of 60 nm Ag nanospheres (η_b = 160 nm/RIU), or of 60 nm silver nanocubes (η_b = 113 nm/RIU) [161,162]. Mock et al. evaluated the sensitivity of nanotriangles with longest dimension (D = 83 nm and t = 10 nm), finding η_b = 350 nm/RIU [86]. A lower sensitivity value (η_b = 315 nm/RIU) was obtained by Martinssonet et al., exploring nanoplates with average particle size equal to 30 nm and t = 5 nm [155].

Figure 28- LSPR plasmon spectrum as a function of RI of solvents n = 1.33 (red solid line) and n = 1.479 (dotted blue line) (a). LSPR peak shift for different refractive index solvents (b).

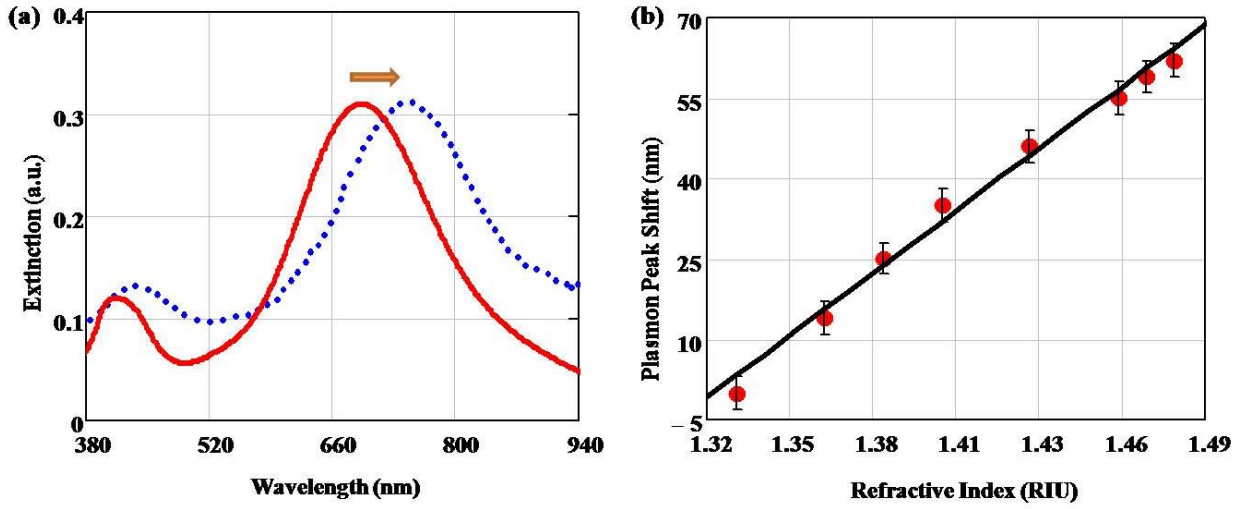

Source: belong to author

Table 7 presents bulk sensitivity of colloids and single Ag particles with different shapes, indicating the potential of exploring AgNPls as a starting point for the development of LSPR sensors. Our previous simulations lead to establish of the AgNPls dimensions that provide the highest sensitivity values for AgNPls.

The shift in LSPR spectra can also be induced by molecular attachment to the surface of NPs, provided by an attractive interaction, such as chemisorption, electrostatic or hydrophobic interaction. On LSPR molecular sensing, EM field decay is an important parameter, as described in section 2.3.3. For AgNPls we observed, in figure 26, that EM field decay length could vary from 5.19 nm (D = 10 nm) to 18.33 nm (D = 60 nm). The AgNPls decay length are bigger than the l_d literature values for nanodisks (6 nm) or Ag cores with Au shells (11 nm) [154,163].

Table 7- Survey of LSPR peak wavelength, bulk sensitivity, and Figure of Merit values for Ag nanoparticles with shapes.

Shapes	Ensemble/single	Resonance (nm)	Sensitivity(nm/RIU)	FoM	References
Nanoplates	Ensemble	686	409	2.6	Measured
Nanocubes	Ensemble	434	113	–	[162]
Nanospheres	Ensemble	398	144	3.0	[155]
Nanoplates	Ensemble	552	315	3.6	[155]
Nanocubes	Ensemble	444	158	3.3	[155]
Nanosphere	Single	435	160	2.2	[164]
Nanocube	Single	510	146	1.6	[102]
Nanoplate	Single	760	350	4.4	[86]
Nanorod	Single	776	400	–	[165]

The high AgNPls colloid bulk sensitivity value and the relatively long decay length indicate that nanotriangles are attractive structures for molecular sensing. LSPR sensing depends not only on the plasmonic peak shift but also on the precision to identify spectral changes. Therefore, Figure of Merit (FoM) defined in section 2.3.2, is another important parameter for sensor's performance.

In water, FWHM of the AgNPls plasmon peak was found to be 163 nm, and therefore the FoM value of the colloidal LSPR sensor platform was 2.6. On figure 28(a), a change around 34 nm of the plasmon FWHM was observed, with the increase of medium RI, Δn_d = 0.149, leading to 16% change on FoM values.

The increase in FWHM is associated to an enhancement in imaginary part of Ag dielectric function. The table 7 depicts the bulk sensitivity and FoM values of NPs with different shapes for individual and ensemble nanoparticles. In particular, it is expected that spectroscopic techniques exploring single particle detection would lead to a narrow extinction plasmon band, and therefore, to higher FoM values. Moreover, the product (η_b x FoM) gives a good indication of the sensing capability of a platform. From the table 7, a high value of η_b x FoM (1055.6) can be obtained by exploring silver nanotriangles, indicating the potential use of a nanostructure on sensor platforms.

4.3.3 Nanoplate for PDT

On MEO, it is required that the PS absorption spectrum overlaps the LSPR extinction peak. In particular, the absorption and emission spectrum of the MB (photosensitizer) overlaps the AgNPls extinction spectrum peak at 693 nm with 163 nm FWHM, as shown in figure 29. The MB emission peak is found at 692 nm, and emission intensity increases as MB concentration goes higher. AgNPls and MB present features that could lead to MEO. The surface charge density of the nanoparticle is expected to be +Ve, [166] while MB molecule in water solution is cationic [167]. Therefore, AgNPls-MB aggregation, due to electrostatic interaction is not expected. With the addition of MB in the colloid, no shift on the LSPR peak was observed, indicating that the fluorescent molecules were not attaching to the NP surface.

Figure 29- Extinction spectra of colloidal AgNPls, MB and fluorescence emission of MB aqueous solution, excited with 632.8 nm.

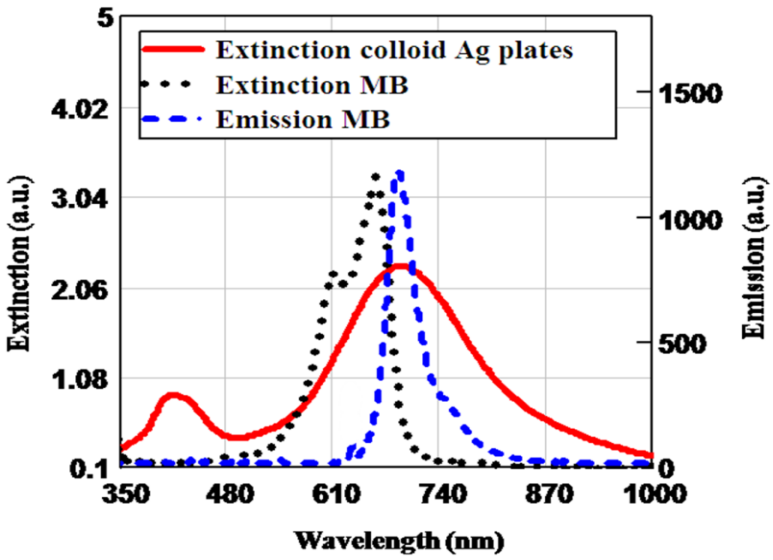

Source: belong to author

By playing with the MB and AgNPls concentrations, both metal-enhanced fluorescence (MEF) and fluorescence quenching, RET, can be observed on the MB-AgNPls solution. Figure 30(a) shows that AgNPls (3 µM) can prompt MEF on MB solution, with low PS concentration (<16 nM). For higher concentration of the PS, AgNPls induce the decrease of the MB fluorescence emission, as shown in figure 30(b). At high concentration (>2 μM), due to re-absorption process, a small red-shift of the MB emission was also observed. MEF phenomenon is attributed to the enhanced local electric field close to sub-wavelength nanoparticles, and quenching effect is due to the energy transfer between fluorophore and the metallic nanoparticles [168–170].

The MEF of the PS can be an indication that MEO is achievable on the MB-AgNPls colloid. On the investigation of the MEO, the GR singlet oxygen sensor (~1µM) was introduced to MB-AgNPls colloid. He-Ne laser light irradiated the colloid, simultaneously exciting the dipole plasmon mode and the MB molecules, during 2 minutes.

Figure 30- Emission intensity of MB solution, with AgNPls (blue circle) and without AgNPls (red square) at lower (a) and higher (b) concentrations, respectively.

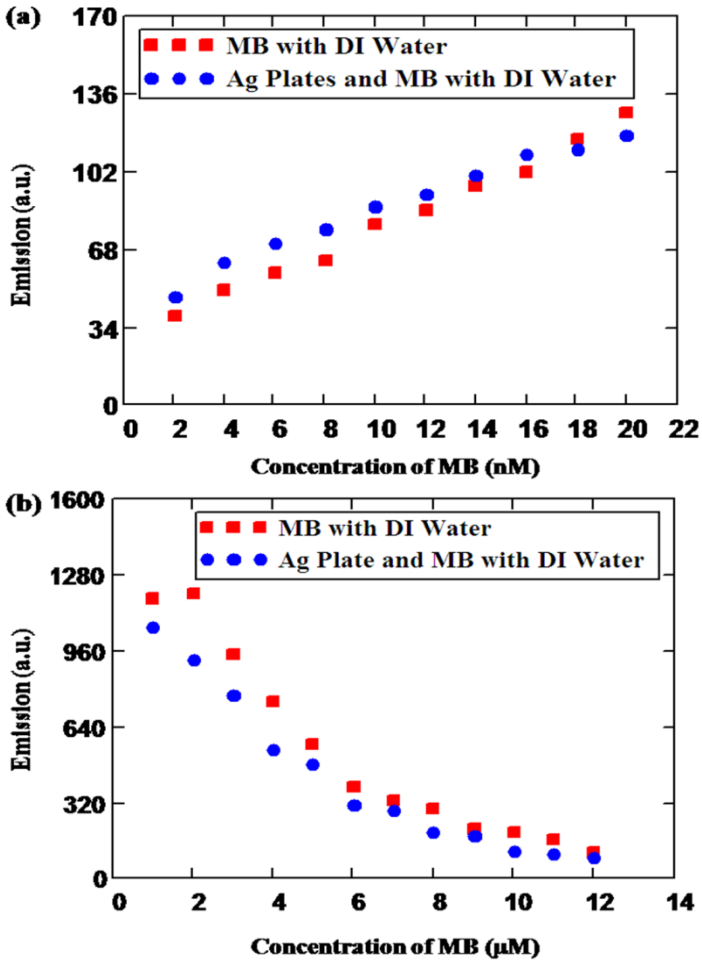

Source: belong to author

After that, the colloid was exposed to 500 nm light (~1.1mW), exciting the GR sensor. MB is not efficiently excited at 500 nm, and there is no significant overlapping of the MB and GR emission spectra. Figure 31 shows emission spectra of GR in the MB solution, with and without Ag plates. The AgNPls induce a clear enhancement of the GR emission, indicating an increase on the MB production of oxygen singlet, due to the interaction of the PS with the nanotriangles. The MEF resulting from the NP-GR molecules interaction is also considered on the evaluation of the GR emission.

Figure 31- Emission spectra of GR in MB solution and in MB-AgNPls colloid, excited with light at 500 nm wavelength.

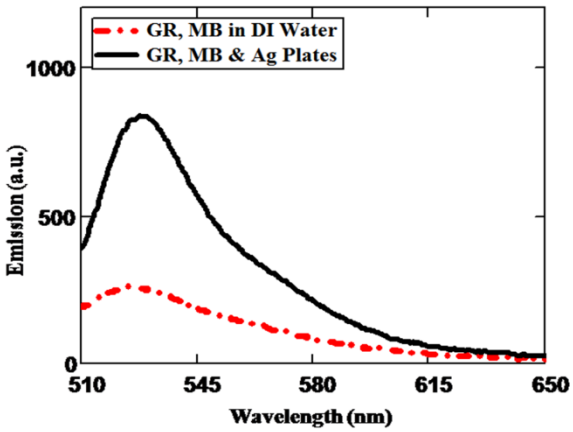

Source: belong to author

To quantify the MEO, we follow the procedure described in reference [171]. Shortly, we measured the fluorescence emission of the GR sensor (excited with 500 nm) in the MB solution, with and without nanoparticles, after the laser irradiation. Additionally, we calculated the integrated spectra of the MB aqueous solution with and without nanoparticles. The MEF of GR due to AgNPls was taken into account on the determination of MEO value.

The MEF factor for GR, GR_{MEF}, is obtained as:

$$GR_{MEF} = \frac{\int_0^\infty GR_{AgNPls} d\lambda}{\int_0^\infty GR_{Water}\, d\lambda} \tag{4.1}$$

Where $\int_0^\infty GR_{AgNPls} d\lambda$ and $\int_0^\infty GR_{Water}\, d\lambda$ are integrated spectra for GR solution with and without Ag nanoplates. The metal enhanced $^1O_2$, $^1O_{2,MEO}$, for MB is calculated as:

$$^1O_{2,MEO} = \frac{\int_0^\infty (GR, MB)_{AgNPls} d\lambda - \int_0^\infty (MB)_{AgNPls} d\lambda}{GR_{MEF}\left[\int_0^\infty (GR, MB)_{water} d\lambda - \int_0^\infty (MB)_{water} d\lambda\right]} \tag{4.2}$$

where $\int_0^\infty (GR, MB)_{AgNPls}\, d\lambda$ and $\int_0^\infty (GR, MB)_{water}\, d\lambda$ are the integrated spectra of the GR-MB solution with and without AgNPls, after exposure to He-Ne light.

Table 8- Metal-enhanced fluorescence (MEF) and metal-enhanced singlet oxygen generation (MEO) for different concentrations of MB in the presence of AgNPls colloid.

Concentration (nM)	MEF	MEO
4	2.3	2.2
16	1.30	1.1

Source: belong to author

Moreover, $\int_0^{\infty}(\mathrm{MB})_{\mathrm{AgNPls}}\,d\lambda$ and $\int_0^{\infty}(\mathrm{MB})_{\mathrm{water}}\,d\lambda$ are the integrated spectra of the MB solution with and without AgNPls, after exposure to He-Ne light. Table 8 shows the MEO values obtained for the MB-AgNPls colloids, with different PS concentrations. Table 8 also indicates the enhancement of MB emission due to the interaction with Ag nanostructures (MEF). As shown in table 8, MEO and MEF have higher values at low concentration of MB, as compare to high concentration of the PS. Moreover, higher values MEO are associated to more effective MEF, indicating that the PS emission spectroscopy can be used as an indication tool for metal enhanced oxygen singlet generation analyses.

De Melo et al. evaluated the use of Ag nanospheres on MEO, obtained 140% increase on oxygen singlet generation by riboflavin photosensitizer [172]. Our results shows 220% increase of the oxygen singlet generation due to the AgNPls (table 8), indicates the potential use of the nanostructure on PDT. Moreover, it is known that silver nanoparticles present antimicrobial activity that could, together with the PDT action, enhance the damage on bacterial and yeast biofilms.

5 EXPLORING GOLD NANOSHELLS ON SINGLET OXYGEN GENERATION

5.1 Introduction

In this chapter, gold nanoshells are considered of dielectric material (silica) core covered by thin metal (gold) shell that may be absorbed or scattered light within the range from UV to NIR (700-1300 nm) [173]. The core/shell Au nanostructures have been extensively studied for potential applications as increasing photoluminescence [174], catalysis [175], SERS [176] and fabricating photonic crystals [177]. In particular, biomedical applications include sensing [16], photothermal therapy (PTT) [138], hyperthermia [178], and targeted drug delivery [35] because of their valuable optical characteristics in stability, biocompatibility, low immunogenicity, and versatility [35]. Furthermore, due to their scattering features, Au nanoshells can be harvested in diagnostic imaging for computing topography as contrast enhanced reagent, photo-acoustic topography [179], optical coherence tomography [180] and dark field microscopy [181].

Various features of Au nanoshells can be exploited by varying the shell thickness to make them appropriate for different applications, for instance, PTT demands higher absorption nanoparticles while imaging and PDT require a system based on particles of higher scattering [31,182]. Loo and coworkers designed and manipulated silica core/gold shells for optical cancer imaging through scattering to destroy carcinoma cells by highly intensive absorption [183].

In this chapter, we evaluate the use of negatively charged silica core/gold thickness layer nanostructures with Methylene Blue on MEO. The selection of Au nanoshells is based on the fact that extinction LSPR peak (651 nm) overlaps the MB spectrum. The pre-determined near electric field around the nanoshell was calculated by finite element method (FEM) simulation, and MEO was quantified. The influence of irradiation time and concentration of metallic nanostructures on MEO was also appraised.

5.2 Materials and Methods

Gold nanoshells colloid sample contains polyvinylpyrrolidone (PVP) stabilizer with Au mass concentration (0.053 mg/mL) was obtained from nanoComposix. The specified average diameter of the nanostructures was 125±5.8 nm with core diameter 82.6±4.7 nm and shells thickness 21.5 nm. Methylene Blue, obtained from Merck, was utilized as a photosensitizer dye

to induce singlet oxygen generation. Singlet oxygen green reagent (GR), from Thermofisher, was prompted as the singlet oxygen sensor. The sensor stock solution was prepared adding 100 µg of GR in 330 µL of methanol solution. The solution concentration 500 µM of GR was kept at appropriate temperature under the dark. The GR depicts an optical excitation maximum at 504 nm and emits green light with maximum wavelength at 525 nm. The He-Ne laser (at 632.8 nm) was employed for the photosensitizer (MB) excitation. At the sample, the laser power was 1.25 mW with spot size ~ 40 mm. Scanning electron microscope (SEM) images of the gold nanoshells were obtained using MIRA 3 TESCAN functioned at 20 kV. These images were carried out on silicon substrates with dispersed Au shells. The samples LSPR extinction spectrum (300-1000 nm) were obtained using an Ocean Optics spectrophotometer (HR +4000). Samples were placed in 1 cm path length quartz cuvette. Fiber bundles were used to guide incident light from a Deuterium Halogen light source to the sample and to send light from sample to the spectrophotometer detector. Finite Element Method (FEM) based calculations were performed using COMSOL Multiphysics. Simulations were used to determine the frequency domain scattered field distribution near to the nanoshell. On the simulation, the nanoparticles were considered to isotropic (spherical) shapes. The simulations evaluated Au shell keeping constant core with various gold layers thickness. Moreover, the nanostructure shell thickness varied from 5 to 20 nm. On the numerical analysis, the back ground electric field amplitude (E_0) was adjusted as 1 V/m. For all Au shells size evaluated, different tetrahedral meshing were manipulated. A perfectly matched layer (PML) was explored around the shell to minimize reflection artifacts. The radius of PML spherical shaped model was 600 nm and layer thickness was 200 nm with triangular meshing. Au shells geometry was designed by free tetrahedral meshing. The radius of silica core (R) 42 nm with coated Au layer thickness (T) were employed. The data for real and imaginary refractive index dispersion is obtained from J&C [58].

5.3 Results and Discussion

5.3.1 UV-Visible Spectrum Analyses

On the characterization of the nanoparticles, scanning electron microscope images and optical transmission spectrum were explored. Figure 32 shows the Au nanoshell model for simulation (left) and SEM images of dispersed Au nanoshells on the surface of silica wafer

(right), indicating spherical shape. The figure 32 confirmed 125 nm average diameter of the nanoshell used.

Spectroscopic analyses were also performed on the characterization of the purchased colloid. Au nanoshells on the surface of silica wafer, indicating spherical shape. Figure 33 exhibits extinction spectra of gold shells obtained experimentally (peak at 651 nm) and theoretically (peak at 650 nm). The measured plasmon spectrum appears in good agreement with the simulated result.

Figure 32- The gold nanoshell model for FEM simulation (left) in the surrounding medium (n_m). SEM of silica core with gold coated thickness on silicon wafer substrate (right). Scale bar of the image: 1µm. Scale bar of inset image: 200 nm.

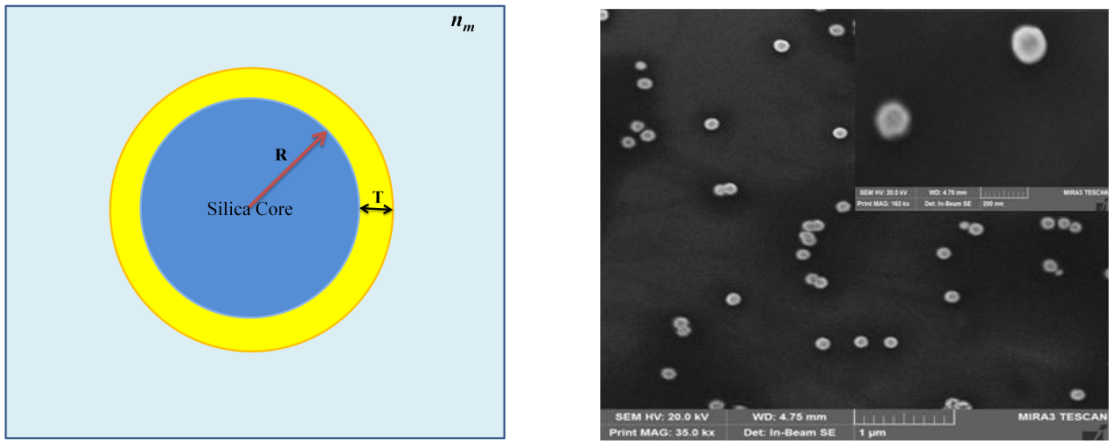

Source: belong to author

Figure 33- The localized surface plasmon resonance extinction spectrum of the gold nanoshells.

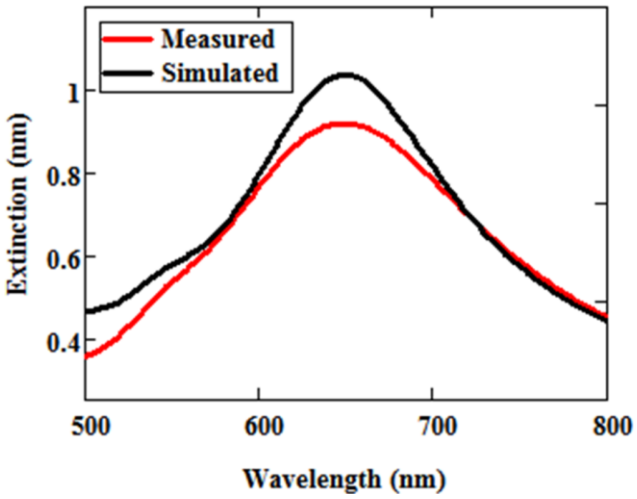

Source: belong to author

5.3.2 LSPR Field Analyses

In order to reveal the insight effects of E-field distribution and its influence near the Au nanoshell surface, analysis and calculations using FEM simulation were performed. The near field distribution was obtained by 3-D space that contained Au nanoshells. All the simulations were calculated in homogeneous surrounding medium water (n = 1.33) that makes the results more practical for biological applications.

Figure 34 shows the cross sections of absorption and scattering of gold nanoshells with different shell thickness, keeping silica core R = 42 nm. For thin Au layer thickness (T = 5 nm), the absorption and scattering cross sections values are $5.0x10^4$ nm^2 and $5.3x10^4$ nm^2 and no difference can be observed in their LSPR peak position (figure 34(a)). However, the absorption spectra is affected by dipole as well as quadrupole resonance modes, while scattering is influenced only by dipole mode. On increasing the Au shell thickness from 5 to 20 nm, the absorption cross section is decreasing gradually as compared to scattering (figure 34(a-c)). Even the scattering becomes more important for T = 20 nm where absorption is very low.

Figure 34- Nanoshells scattering and absorption cross sections with core radius 42 nm and shell thickness 5 nm (a), 10 nm (b) and 20 nm (c), respectively.

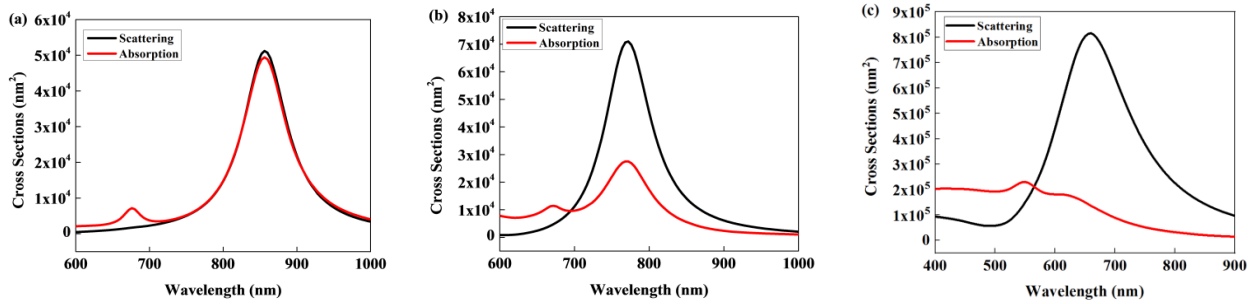

Source: belong to author

Moreover, the Au nanoshells (silica core/Au shell) depict scattering cross section (C_{sca} = 8.2 x 10^5 nm^2 for R = 42 nm and T = 20 nm) that is higher than to the solid Au spheres reported by Jain et al. [31]. Also, the variation in size of nanospheres from 5 to 100 nm limit the optical spectrum (510-560 nm) and may be ineffective to obtain desired tunability in the transparent window 700 to 900 nm [184].

Therefore, due to higher scattering magnitude and broad range covering LSPR spectrum in NIR, nanoshells are more prompted for imaging and therapy as compared to gold nanospheres. Moreover, decrease in Au coated layer thickness, the extinction LSPR spectra of silica/Au nanostructures exhibit a distinct red-shift from 650 nm for 20 nm thickness to 854 nm for 5 nm layer thickness.

Here, E-field was calculated at LSPR extinction peaks for various thickness, as shown in figure 35. Further analyses on E-field calculations show that higher E-field distribution occurs in the direction of polarization but decreases as the distance increases from particle surface. It can be seen clearly that stronger field intensity is generated by altering the gold layer thickness, as shown in figure 35(a-c).

The changes in normalized electric field (|E/E0|) on Au nanoshells were compared at different wavelengths using numerical results as shown in figure 36. The center of Au nanoshell is located at the position X = 0, Y = 0 and Z = 0, as well as the field enhancement along X-axis in homogeneous medium was found by changing Au layer thickness. The maximum field exists at 714 and 854 nm for 10 and 5 nm shell thickness in XY plane at Z = 0. However, the highest normalized field was found for shell thickness 20 nm at 650 nm, comparatively to the NP with the shell thickness 5 and 10 nm.

It is interesting to notice that the LSPR extinction peak (at 650 nm) for 20 nm Au nanoshell is very close the excitation peak (664 nm) of MB dye. Indicating that Au nanoshell (T = 20 nm) can be manipulated to enhance the generation of singlet oxygen by MB. Moreover, nanoshell with different thickness will not be effective on MEO of MB solution. Figure 37 demonstrates the magnitude of normalized E-field distribution decay on nanoshells with Au layer thickness 5, 10 and 20 nm under the excitation at 633 nm. As expected, the E-field and the field decay length are higher for thickness 20 nm as compared to 5 nm or 10 nm under the excitation at 633 nm. At ~20 nm away from the NP surface, the field enhancement at excitation wavelength (633 nm) for 20 nm shell thickness is 2 times higher than 10 nm thickness, and 3.7 times greater than for 5 nm thickness.

Figure 35- The normalized electric field distribution at XY plane of silica core/Au shells with the thickness (a) T = 5 nm, (b) T = 10 nm, and (c) T = 20 nm corresponded to the fields at extinction spectral peaks 854 nm, 714 nm and 650 nm plasmonic wavelengths respectively.

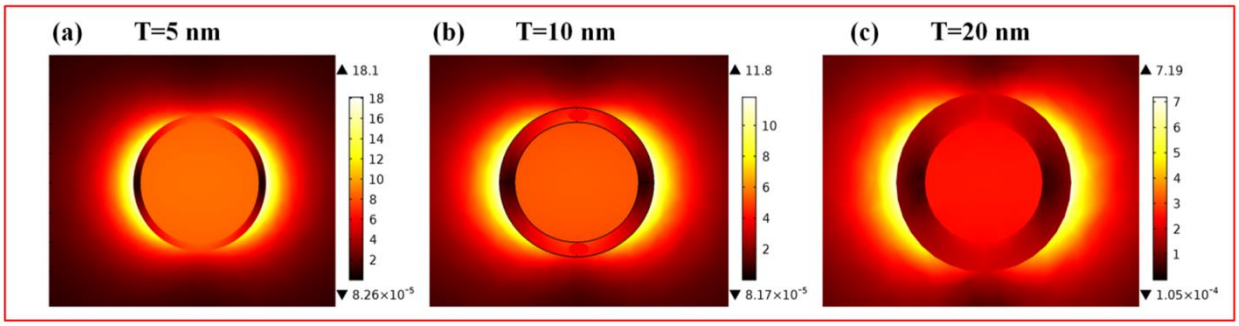

Source: belong to author

Figure 36- The electric field distribution ($|E/E_0|$) along X-axis (both Y = 0 and Z = 0) obtained by FEM simulation and (a-c) corresponds to the 650 nm, 714 nm and 854 nm respectively, for different shells thickness.

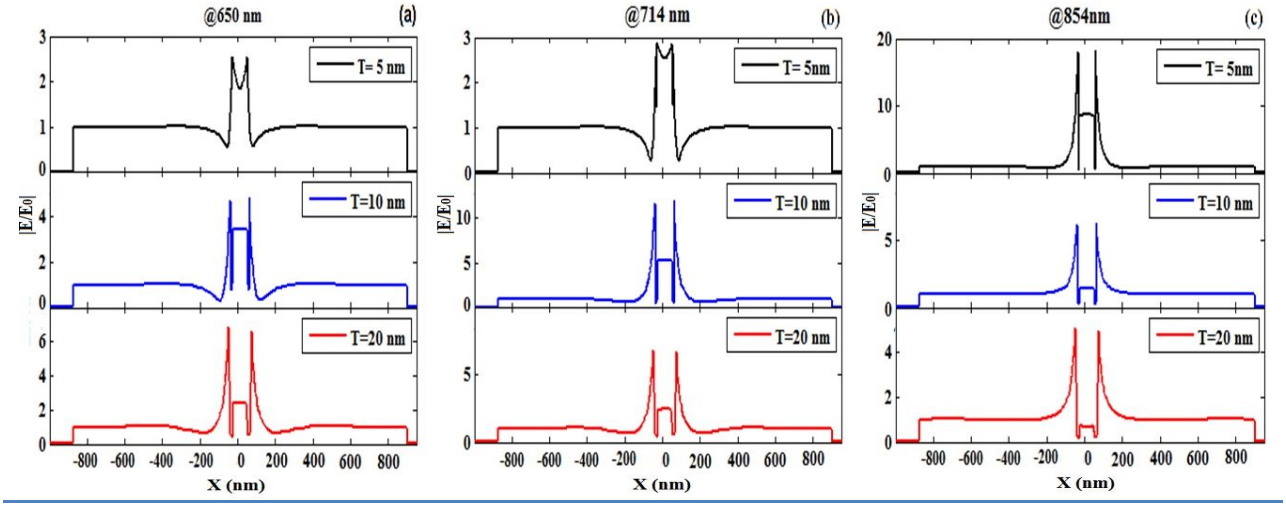

Source: belong to author

Figure 37- Normalized E-field enhancement ($|E/E_0|$) with respect to distance from the surface of Au shell with various silica coated thickness under the excitation at 633 nm.

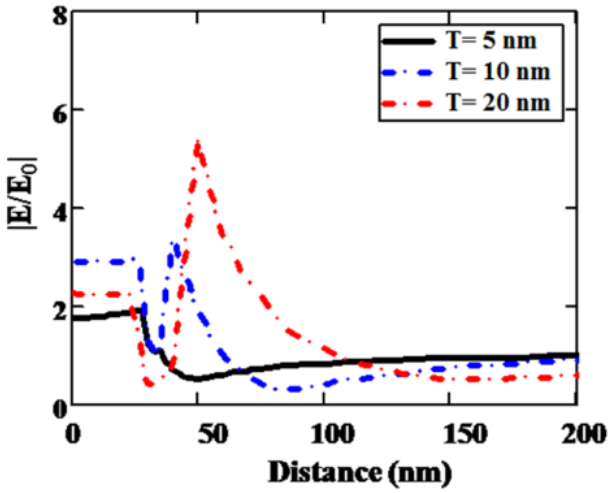

Source: belong to author

5.3.4 Gold Nanoshells for MEO

Au nanoshells and MB present features that could lead to MEO. The surface charge of the nanoshells is expected to be –Ve, while MB molecules in water solution are cationic. Electrostatic interaction can determine the NP-MB coupling and even lead to conjugation. The metallic NP-PS distance is an important factor on MEO, although particle surface charge as well as concentration can also play a significant role on MEO. The conjugation of NP and PS in solution phase due to electrostatic interaction, with the opposite charge signal, may lead to resonance energy transfer (RET) that can reduce the generation of $^1O_2$. To avoid RET, some chemical and physical techniques are adopted [185,186]. For molecules with opposite charges, RET can be avoided by controlling the NP-PS distance with the solution compounds concentration. Moreover, for an effective MEO, plasmonic extinction peak and the PS absorption spectrum should overlap. In particular, 84 nm silica core/ 20 nm Au shell shows LSPR peak at 651 nm, as observed in figure 33 and theoretical calculated peak is 650 nm. Therefore, these nanoparticles can be employed to enhance the generation of singlet oxygen on MB. Figure 38 reveals experimentally that the colloidal Au nanoshells spectrum overlaps the MB extinction (peak at 662 nm) and emission spectra (peak at 692 nm).

Figure 38- UV-Visible extinction spectra of colloid Au nanoshells, extinction and fluorescence intensity of MB.

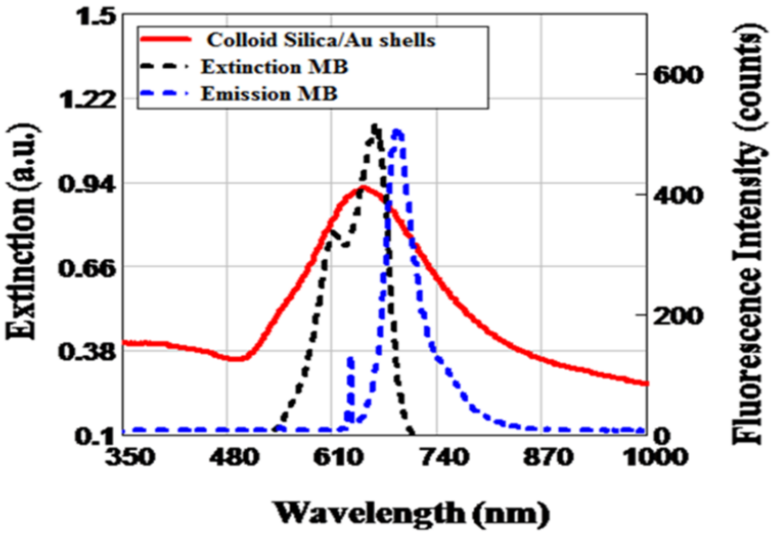

Source: belong to author

To investigate MEO, singlet oxygen sensor GR of concentration (1 µM) was used with colloidal MB-Au nanoshells. The colloid was irradiated by He-Ne laser for 2 minutes to excite MB molecules. Further, the colloid was exposed with light source at wavelength 500 nm exciting the GR sensor. As there is no overlapping between GR and MB emission spectra, therefore MB is not influenced at 500 nm wavelength light. Figure 39 depicts GR emission spectra, with and without nanoshells, using MB photosensitizer. It is evident that fluorescence intensity of GR is increased with coated nanoparticles.

To quantify MEO, we used the procedure introduced in chapter 4 (section 4.3.3). We calculated the fluorescence emission of the GR sensor (excited at 500 nm), with and without nanoshells in the MB solution, after the laser irradiation. In addition, we measured the integrated spectra of the aqueous MB, with and without nanoshells, under laser irradiation.

Figure 39- Fluorescence intensity spectra of GR in MB solution and MB-shells colloid, excited at 500 nm wavelength.

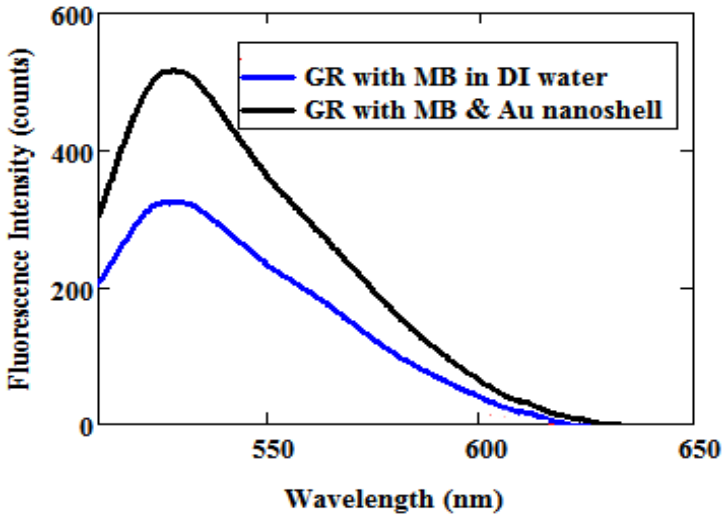

Source: belong to author

The MEF of GR due to Au nanoshells was taken into account in order to find MEO value. The MEF for GR, GR_{MEF}, is determined as $GR_{MEF} = \frac{\int_0^\infty GR_{AuNP} d\lambda}{\int_0^\infty GR_{Water}\, d\lambda}$ and already described in section 4.3.3. The metal enhanced $^1O_2$, $^1\dot{O}_{2,MEO}$, for MB was calculated as discussed in section 4.3.3 ($^1\dot{O}_{2,MEO} = \frac{\int_0^\infty (GR,MB)_{AuNP} d\lambda - \int_0^\infty (MB)_{AuNP} d\lambda}{GR_{MEF}\left[\int_0^\infty (GR,MB)_{water} d\lambda - \int_0^\infty (MB)_{water} d\lambda\right]}$). The MB with Au nanoshells produced more singlet oxygen than without nanoparticles. The $^1O_2$ prompted by Au nanoshells was detected indirectly using fluorescent probe GR. Figure 40 shows the fluorescence peak intensity of GR in MB aqueous solution with and without Au nanoshells, as a function of irradiation time (at 632.8 nm, 1.2 mW). The calculated fluorescence intensities were normalized to the initial sample fluorescence at each instant of time. With the increasing the irradiation time, higher $^1O_2$ production was observed with the presence of metallic Au nanoparticles. This is due to contribution of plasmon resonance effect of AuNPs [171].

Table 9 depicts MEO values obtained for the MB-NPs colloids, with different Au nanoshells concentrations. As shown in table 9, MEO values increase gradually with the increase of NPs concentration. Zhang et al. explored first plasmon assisted MEO when PS is in close vicinity of Ag island film, and calculated 3-fold more $^1O_2$, upon exposure of UV irradiation [187].

Figure 40- Fluorescence intensity ratio of GR with several irradiation time for MB solution with and without Au nanoshells.

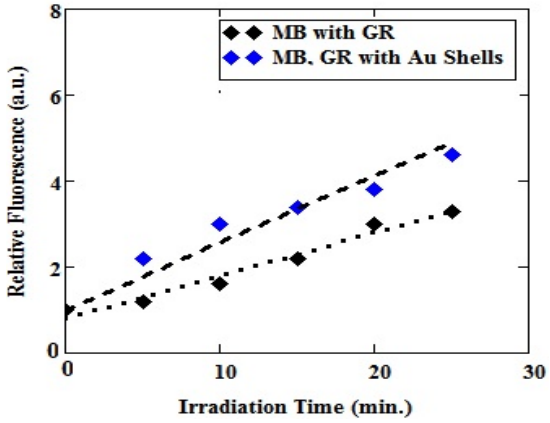

Source: belong to author

Table 9- MEO generation of MB for various concentrations of Au nanoshells.

Mass Concentration (μM)	MEO
2.4	0.8
4.8	1.40
7.2	2. 2
9.4	2.5
11.8	3.2

Source: belong to author

By exploring a solution-based platform, de Melo et al. demonstrated the potential application of silver nanoparticles, enclosed by a pectin layer, on photodynamic therapy and 1.8-fold enhancement of the singlet oxygen production by riboflavin solution were observed [172]. Moreover, in chapter 4, 220% increase of the oxygen singlet generation due to silver nanoplates was observed. The Au nanoshells improved more singlet oxygen generation (300%) on MB, seen in table 9. Moreover, the gold nanoshells suggest a high value of MEO than to silver plates due to the fact that plates depict higher E-field distribution at tips but weak on the sides. The obtained results indicate the potential use of the shells for generating higher MEO on PDT applications.

6 CONCLUSION AND FUTURE PERSPECTIVES

6.1 Conclusion

The noble metal nanostructures endow Localized Surface Plasmon Resonance with unique physical, chemical and optical features. The robust scattering and absorption of plasmonic nanostructures provide an opportunity to utilize them in label free sensing and Photodynamic therapy. The LSPR extinction spectrum is reliant on shape, size, materials composition and dielectric function of surrounding medium.

By exploring computer simulation, the performance of nanostructure-based sensing LSPR platform were evaluated. FEM simulation approach was adopted on the assessment of the LSPR spectrum and EM spatial distribution near metallic nanoparticle, leading to the identification bulk and molecular sensitivity as a function of the nanoparticle size. Here, Campbell's model was extended for multilayer nanostructures and, for the first time this model was evaluated exploiting single NP size-dependence approach. Moreover, the presented results provide insights on the LSPR behavior due to adsorption of molecules layer on the NP surface, establishing a new paradigm on engineering LSPR biosensor.

Moreover, the theoretical approach determined the assessment of the nanoparticle design, leading to high performance of nanoplates (nanotriangles) solution-based platform for sensing and PDT. The control of the nanoplates altitude lengths and thickness leads to tune LSPR extinction bands and spatial distribution of the electromagnetic field enhancement near the metallic nanoplates. Both increasing the plate's altitude and decreasing the thickness strongly influence on plasmon peak as well as FWHM. In particular, for ~57 nm altitude plates, EM field enhancement extends for more than 18 nm, indicating the feasibility of using the nanoplates on molecular sensing. High sensitivity (406 nm/RIU) and good FoM (2.6) values were indicating for AgNPls colloids to employ plates for sensing applications.

The silver plates colloids are also encouraged to use for metal enhanced singlet oxygen generation and metal enhanced fluorescence in the vicinity of MB aqueous solution. A 220% increase of the MB oxygen single generation due to the AgNPls indicates the potential use of the nanostructure on PDT.

Furthermore, we have also exhibited the potential use of silica/gold nanoshells colloid conjugate with methylene blue on PDT. The production of metal-enhanced singlet oxygen was detected and quantified for MB water solution with the silica core/Au coated thickness layer nanoparticles. We demonstrated the presence of Au nanoshells improved singlet oxygen generation (300%) on MB.

The methodology developed in this thesis allows engineering high performance nanostructures for biomedical application.

6.2 Future Prospects

6.2.1 Explore FEM on Optical-Thermal therapy

The strong absorption of metallic nanoparticles enable them to employ in optical-thermal therapy. The absorption of sub-wavelength nanostructures increases the temperature around the nanoparticles that is manipulated to ablate cells. Based on FEM, diverse shapes or size of metal nanoparticles can be manipulated to predetermine higher absorption. The initial simulations given in this thesis make promise in ever evolving world of optical-thermal research. In particular, more work should be needed with spheres, triangular nanoplates and gold nanoshells. There should be other variables included using FEM to manipulate thermal related characteristics such as inter-particle distance, different core-shell ratios and nanoparticles size. Various other shapes, for instance gold nanorods or bipyramids, need to examine due to their high surface to volume ratio and can provide wide possibility in thermal related areas.

6.2.2 Evaluate Substrate and Solution based-Platforms

The localized surface plasmon resonance peaks of gold nanoparticles can be tuned from visible to near-infrared region to explore on several sensing applications. However, the evaluation of light interaction with plasmon nanoparticles on a suspension or on a dielectric substrate may influence on sensibility and stability of the platforms. The metal nanoparticles on substrate can induce higher electric field enhancement that can improve sensor performance. Previous simulations were performed comparing the field enhancement of NP on substrate and in a liquid medium predict the higher field intensity on substrate, to pave the way for their use in sensing.

6.2.3 Smartphone-based Detection

There is currently great interest in exploring fast and cost effective diagnostic optical technology. Usually these optical diagnostics are obtained using traditional devices, such as spectrophotometers, which are often large, heavy and expensive instruments requiring skilled or technical experts to handle them. However, access to these instruments for spectroscopic evaluation are limited in developing countries and in the less developed regions of the world, as neither the devices required nor the knowledge to handle such devices are accessible to the general public. In recent years, there has been a growing interest in developing portable, low-cost optical spectroscopic devices and integrating them with mobile phones to take advantage of the ease of accessing and processing data using mobile computing technology. For example, several smartphone-based spectrometers have been demonstrated at wavelength resolutions ranging from 2 to 15 nm. Currently the Laboratory of Biomedical Optics at UFPE is implementing a self-referenced colorimetric method for mobile-phone, that can be used on the color change evaluation of LSPR sensor platform.

6.2.4 Candida Albicans PDT

Based on our results (chapter 5), the use of gold nanoshells are being explored by the LOBI team for the photoinactivation of *Candida albicans*.

6.3 List of Publications

6.3.1 Articles Published

- **Sajid Farooq**, Wendell W. Neves, Omar Pandoli, Tommaso Del Rosso, Leonardo M. de Lima, Rosa F. Dutra, Renato E. de Araujo,"*Engineering a plasmonic sensing platform for Candida albicans antigen identification*," **J. Nanophoton**.12(3), 033003 (2018). doi: 10.1117/1.JNP.12.033003
- **Farooq, S**. and de Araujo, R. E. (2018), "*Engineering LSPR platform for molecular biosensing*," **Open Journal of Applied Sciences**, 8, 126-139. https://doi.org/10.4236/ojapps.2018.83010
- Martha S. Ribeiroa, Luciana S.A. de Melo, **Sajid Farooq**, Alessandra Baptista, Ilka T. Kato d, Silvia C. Núñez, Renato E. de Araujo, *Photodynamic inactivation of Escherichia coli and Streptococcus mutans assisted by localized surface plasmon resonance of silver nanoparticles*. **Photodiagnosis and Photodynamic Therapy** 22 (2018) 191–196. https://doi.org/10.1016/j.pdpdt.2018.04.007
- **Sajid Farooq**, F. Nunes; R. E. de Araujo (2018), "*Optical Properties of Silver Nanoplates and Perspectives for Biomedical Applications*". **Photonics Nanostructures: Fundam**. **Appl**, https://doi.org/10.1016/j.photonics.2018.07.001

6.3.2 Congress Contribution

- **S. Farooq**, R. de Araujo; Evaluating the use of silica coated gold nanoshell on metal enhanced singlet oxygen generation, CLEO/Europe-EQEC 2017.
- **S. Farooq**, R. de Araujo; G. de Oliveira, R. Dutra; Engineering a solution-based localized surface plasmon resonance platform for Dengue diagonosis, CLEO/Europe-EQEC 2017.
- **S. Farooq**, R. de Araujo; Exploring Triangular Silver Nanoplates LSPR Modes for Biological Application, 10^{th} International Conference on Nanophotonics (ICNP) Recife-PR Brazil 2017.
- **S. Farooq**, R. de Araujo; Metal-Enhanced Singlet Oxygen generation by Silica coated Gold Nanoshells, 10^{th} International Conference on Nanophotonics (ICNP) Recife-PR Brazil 2017.
- Correia, T.T.S., **S. Farooq**, R. de Araujo; Photodynamic Inactivation of Candida Yeast Assisted by Gold Nanoshells, VIII Interactional Symposium on Diagnostics and Therapeutic (SINATER) Recife-PE Brazil 2017.
- YM, BArbosa ; WR, C. J. ; CCBO Mota ; ARAUJO, R. E. ; **FAROOQ, S.** ; CARNEIRO, V. ; PLA, Nascimento . LASER DIODO PARA SENSIBILIDADE DENTINÁRIA: ANÁLISE DE DANO TÉRMICO POR ELEMENTOS FINITOS. 2017.

REFERENCES

[1] D.A. Stuart, A.J. Haes, C.R. Yonzon, E.M. Hicks, R.P. Van Duyne, Biological applications of localised surface plasmonic phenomenae, IEE Proc.-Nanobiotechnol. 152 (2005) 13–32. doi:10.1049/ip-nbt.

[2] S.-S. Link, M.A. El-Sayed, Shape and size dependence of radiative, non-radiative and photothermal properties of gold nanocrystals, Int. Rev. Phys. Chem. 19 (2000) 409–453. doi:10.1080/01442350050034180.

[3] B. Sepúlveda, P.C. Angelomé, L.M. Lechuga, L.M. Liz-Marzán, LSPR-based nanobiosensors, Nano Today. 4 (2009) 244–251. doi:10.1016/j.nantod.2009.04.001.

[4] E.C. Dreaden, A.M. Alkilany, X. Huang, C.J. Murphy, M. a. El-Sayed, The golden age: gold nanoparticles for biomedicine, Chem. Soc. Rev. 41 (2012) 2740. doi:10.1039/c1cs15237h.

[5] E.M. Pridgen, R. Langer, O.C. Farokhzad, Biodegradable, polymeric nanoparticle delivery systems for cancer therapy, Nanomedicine. 2 (2007) 669–680. doi:10.2217/17435889.2.5.669.

[6] M. Faraday, The Bakerian Lecture: Experimental Relations of Gold (and Other Metals) to Light, Philos. Trans. R. Soc. London. 147 (1857) 145–181. doi:10.1098/rstl.1857.0011.

[7] I. Freestone, N. Meeks, M. Sax, C. Higgitt, The Lycurgus Cup — A Roman nanotechnology, Gold Bull. 40 (2007) 270–277. doi:10.1007/BF03215599.

[8] G. Mie, Beiträge zur Optik trüber Medien, speziell kolloidaler Metallösungen, Ann. Phys. 330 (1908) 377–445. doi:10.1002/andp.19083300302.

[9] S. Eustis, M.A. El-Sayed, Why gold nanoparticles are more precious than pretty gold: Noble metal surface plasmon resonance and its enhancement of the radiative and nonradiative properties of nanocrystals of different shapes, Chem. Soc. Rev. 35 (2006) 209–217. doi:10.1039/B514191E.

[10] T. Endo, S. Yamamura, N. Nagatani, Y. Morita, Y. Takamura, E. Tamiya, Localized surface plasmon resonance based optical biosensor using surface modified nanoparticle layer for label-free monitoring of antigen-antibody reaction, Sci. Technol. Adv. Mater. 6 (2005) 491–500. doi:10.1016/j.stam.2005.03.019.

[11] G. Seifert, G. Schmid (ed.). Clusters and colloids. From Theory to Applications. VCH Verlagsgesellschaft, Weinheim 1994, 546 p., 232 figs., 37 tabs., hard cover, ISBN 3-527-29043-5, Cryst. Res. Technol. 29 (1994) 956–956. doi:10.1002/crat.2170290707.

[12] C.F. Bohren, D.R. Huffman, Absorption and scattering of light by small particles, Wiley, 1983.

[13] P.K. Jain, W. Huang, M.A. El-Sayed, On the universal scaling behavior of the distance decay of plasmon coupling in metal nanoparticle pairs: A plasmon ruler equation, Nano Lett. 7 (2007) 2080–2088. doi:10.1021/nl071008a.

[14] S. Link, M.A. El-Sayed, Shape and size dependence of radiative, non-radiative and photothermal properties of gold nanocrystals, Int. Rev. Phys. Chem. 19 (2000) 409–453. doi:10.1080/01442350050034180.

[15] K.A. Willets, R.P. Van Duyne, Localized surface plasmon resonance spectroscopy and sensing, Annu. Rev. Phys. Chem. 58 (2007) 267–297. doi:10.1146/annurev.physchem.58.032806.104607.

[16] B.B. Xu, X.Y. Ma, Y.Y. Rao, J. Dong, W.P. Qian, Plasmonic biosensors and nanoprobes based on gold nanoshells, Chinese Sci. Bull. 56 (2011) 3234–3241. doi:10.1007/s11434-011-4670-1.

[17] H. Wang, D.W. Brandl, F. Le, P. Nordlander, N.J. Halas, Nanorice: A Hybrid Plasmonic Nanostructure, Nano Lett. 6 (2006) 827–832. doi:10.1021/nl060209w.

[18] S.E. Skrabalak, J. Chen, Y. Sun, X. Lu, L. Au, C.M. Cobley, Y. Xia, Gold Nanocages: Synthesis, Properties, and Applications, Acc. Chem. Res. 41 (2008) 1587–1595. doi:10.1021/ar800018v.

[19] A.M. Fales, H. Yuan, T. Vo-Dinh, Silica-Coated Gold Nanostars for Combined Surface-Enhanced Raman Scattering (SERS) Detection and Singlet-Oxygen Generation: A Potential Nanoplatform for Theranostics, Langmuir. 27 (2011) 12186–12190. doi:10.1021/la202602q.

[20] G.J. Nusz, A.C. Curry, S.M. Marinakos, A. Wax, A. Chilkoti, Rational selection of gold nanorod geometry for label-free plasmonic biosensors, ACS Nano. 3 (2009) 795–806. doi:10.1021/nn8006465.

[21] J. Lee, W. Hasan, T.W. Odom, Tuning the thickness and orientation of single au pyramids for improved refractive index sensitivities, J. Phys. Chem. C. 113 (2009) 2205–2207. doi:10.1021/jp8111155.

[22] V.K. Sharma, R.A. Yngard, Y. Lin, Silver nanoparticles: Green synthesis and their antimicrobial activities, Adv. Colloid Interface Sci. 145 (2009) 83–96. doi:10.1016/j.cis.2008.09.002.

[23] P. Mulvaney, Surface Plasmon Spectroscopy of Nanosized Metal Particles, Langmuir. 12 (1996) 788–800. doi:10.1021/la9502711.

[24] J.P. Abid, A.W. Wark, P.F. Brevet, H.H. Girault, M.A. El-Sayed, J. Belloni, Preparation of silver nanoparticles in solution from a silver salt by laser irradiation, Chem. Commun. 103 (2002) 792–793. doi:10.1039/b200272h.

[25] K.L. Kelly, E. Coronado, L.L. Zhao, G.C. Schatz, The Optical Properties of Metal Nanoparticles: The Influence of Size, Shape, and Dielectric Environment, J. Phys. Chem. B. 107 (2003) 668–677. doi:10.1021/jp026731y.

[26] I. Pastoriza-Santos, L.M. Liz-Marzan, Colloidal silver nanoplates. State of the art and future challenges, J. Mater. Chem. 18 (2008) 1724–1737. doi:10.1039/B716538B.

[27] Neval A. Cinel, Serkan Bütün, Ekmel Özbay, Electron beam lithography designed silver nano-disks used as label free nano-biosensors based on localized surface plasmon resonance, Opt. Express. 20 (2012) 2587. doi:10.1364/OE.20.002587.

[28] J.C. Hulteen, D.A. Treichel, M.T. Smith, M.L. Duval, T.R. Jensen, R.P. Van Duyne, Nanosphere lithography: Size-tunable silver nanoparticle and surface cluster arrays, J. Phys. Chem. B. 103 (1999) 3854–3863. doi:10.1021/jp9904771.

[29] T.R. Jensen, M.D. Malinsky, C.L. Haynes, R.P. Van Duyne, Nanosphere lithography: tunable localized surface plasmon resonance spectra of silver nanoparticles, J. Phys. Chem. B. 104 (2000) 10549–10556. doi:10.1021/jp002435e.

[30] I. ELSAYED, X. HUANG, M. ELSAYED, Selective laser photo-thermal therapy of epithelial carcinoma using anti-EGFR antibody conjugated gold nanoparticles, Cancer Lett. 239 (2006) 129–135. doi:10.1016/j.canlet.2005.07.035.

[31] P.K. Jain, K.S. Lee, I.H. El-Sayed, M.A. El-Sayed, Calculated Absorption and Scattering Properties of Gold Nanoparticles of Different Size, Shape, and Composition: Applications in Biological Imaging and Biomedicine, J. Phys. Chem. B. 110 (2006) 7238–7248. doi:10.1021/jp057170o.

[32] Mona B. Mohamed, Kamal Z. Ismail, and Stephan Link, M.A. El-Sayed, Thermal Reshaping of Gold Nanorods in Micelles, J. Phys. Chem. B. 102 (1998) 9370–9374. doi:10.1021/JP9831482.

[33] J. Chen, F. Saeki, B.J. Wiley, H. Cang, M.J. Cobb, Z.-Y. Li, L. Au, H. Zhang, M.B. Kimmey, X. Li, Y. Xia, Gold Nanocages: Bioconjugation and Their Potential Use as Optical Imaging Contrast Agents, Nano Lett. 5 (2005) 473–477. doi:10.1021/nl047950t.

[34] A.K.S. Braz, <italic>In situ</italic> gold nanoparticles formation: contrast agent for dental optical coherence tomography, J. Biomed. Opt. 17 (2012) 66003. doi:10.1117/1.JBO.17.6.066003.

[35] B. Singhana, P. Slattery, A. Chen, M. Wallace, M.P. Melancon, Light-activatable gold nanoshells for drug delivery applications., AAPS PharmSciTech. 15 (2014) 741–52. doi:10.1208/s12249-014-0097-8.

[36] P.K. Jain, X. Huang, I.H. El-Sayed, M.A. El-Sayed, Noble metals on the nanoscale: Optical and photothermal properties and some applications in imaging, sensing, biology, and medicine, Acc. Chem. Res. 41 (2008) 1578–1586. doi:10.1021/ar7002804.

[37] S. Khan, F. Alam, A. Azam, A.U. Khan, Gold nanoparticles enhance methylene blue-induced photodynamic therapy: A novel therapeutic approach to inhibit Candida albicans biofilm, Int. J. Nanomedicine. 7 (2012) 3245–3257. doi:10.2147/IJN.S31219.

[38] C. Loo, A. Lin, L. Hirsch, M.-H. Lee, J. Barton, N. Halas, J. West, R. Drezek, Nanoshell-enabled photonics-based imaging and therapy of cancer., Technol. Cancer Res. Treat. 3 (2004) 33–40. doi:d=3018&c=4130&p=12032&do=detail [pii].

[39] M. Soler, M.-C. Estevez, R. Villar-Vazquez, J.I. Casal, L.M. Lechuga, Label-free nanoplasmonic sensing of tumor-associate autoantibodies for early diagnosis of colorectal cancer, Anal. Chim. Acta. 930 (2016) 31–38. doi:10.1016/j.aca.2016.04.059.

[40] N. Nath, A. Chilkoti, Label-Free Biosensing by Surface Plasmon Resonance of Nanoparticles on Glass: Optimization of Nanoparticle Size, Anal. Chem. 76 (2004) 5370–5378. doi:10.1021/ac049741z.

[41] K.M. Mayer, J.H. Hafner, Localized Surface Plasmon Resonance Sensors, Chem. Rev. 111 (2011) 3828–3857. doi:10.1021/cr100313v.

[42] W.Y. Ma, J. Yao, H. Yang, J.Y. Liu, F. Li, J.P. Hilton, Q. Lin, Effects of vertex truncation of polyhedral nanostructures on localized surface plasmon resonance., Opt. Express. 17 (2009) 14967–76. doi:10.1364/OE.17.014967.

[43] M. Potara, A.-M. Gabudean, S. Astilean, Solution-phase, dual LSPR-SERS plasmonic sensors of high sensitivity and stability based on chitosan-coated anisotropic silver nanoparticles, J. Mater. Chem. 21 (2011) 3625. doi:10.1039/c0jm03329d.

[44] X. Jiang, Q. Zeng, A. Yu, Thiol-Frozen Shape Evolution of Triangular Silver Nanoplates, Langmuir. 23 (2007) 2218–2223. doi:10.1021/la062797z.

[45] S. Xu, W. Ouyang, P. Xie, Y. Lin, B. Qiu, Z. Lin, G. Chen, L. Guo, Highly Uniform Gold Nanobipyramids for Ultrasensitive Colorimetric Detection of Influenza Virus, Anal. Chem. 89 (2017) 1617–1623. doi:10.1021/acs.analchem.6b03711.

[46] H. Zhang, Z. She, H. Su, K. Kerman, H.-B. Kraatz, Effects of bipyramidal gold nanoparticles and gold nanorods on the detection of immunoglobulins., Analyst. 141 (2016) 6080–6086. doi:10.1039/c6an01111j.

[47] A.K.S. Braz, R.E. de Araujo, T.Y. Ohulchanskyy, S. Shukla, E.J. Bergey, A.S.L. Gomes, P.N. Prasad, <italic>In situ</italic> gold nanoparticles formation: contrast agent for dental optical coherence tomography, J. Biomed. Opt. 17 (2012) 66003. doi:10.1117/1.JBO.17.6.066003.

[48] S. Hennig, V. Mönkemöller, C. Böger, M. Müller, T. Huser, Nanoparticles as Nonfluorescent Analogues of Fluorophores for Optical Nanoscopy, ACS Nano. 9 (2015) 6196–6205. doi:10.1021/acsnano.5b01503.

[49] N.S. Abadeer, C.J. Murphy, Recent Progress in Cancer Thermal Therapy Using Gold Nanoparticles, J. Phys. Chem. C. 120 (2016) 4691–4716. doi:10.1021/acs.jpcc.5b11232.

[50] S. Krishnan, P. Diagaradjane, S.H. Cho, Nanoparticle-mediated thermal therapy: evolving strategies for prostate cancer therapy., Int. J. Hyperthermia. 26 (2010) 775–89. doi:10.3109/02656736.2010.485593.

[51] R.R. Allison, K. Moghissi, Photodynamic therapy (PDT): PDT mechanisms, Clin. Endosc. 46 (2013) 24–29. doi:10.5946/ce.2013.46.1.24.

[52] A.M. Fales, H. Yuan, T. Vo-Dinh, Silica-Coated Gold Nanostars for Combined Surface-Enhanced Raman Scattering (SERS) Detection and Singlet-Oxygen Generation: A Potential Nanoplatform for Theranostics, (2011).

[53] G. Pasparakis, Light-induced generation of singlet oxygen by naked gold nanoparticles and its implications to cancer cell phototherapy, Small. 9 (2013) 4130–4134. doi:10.1002/smll.201301365.

[54] Y.N. Konan, R. Gurny, E. Allémann, State of the art in the delivery of photosensibilizers for photodynamic therapy, Photochem. Photobiol., B Biol. 66 (2002) 89–106.

[55] J.R. Lakowicz, Radiative decay engineering 5: Metal-enhanced fluorescence and plasmon emission, Anal. Biochem. 337 (2005) 171–194. doi:10.1016/j.ab.2004.11.026.

[56] M.B. Ross, G.C. Schatz, Radiative effects in plasmonic aluminum and silver nanospheres and nanorods, J. Phys. D. Appl. Phys. 48 (2015) 184004. doi:10.1088/0022-3727/48/18/184004.

[57] L.J. Mendoza Herrera, D.M. Arboleda, D.C. Schinca, L.B. Scaffardi, Determination of plasma frequency, damping constant, and size distribution from the complex dielectric function of noble metal nanoparticles, J. Appl. Phys. 116 (2014). doi:10.1063/1.4904349.

[58] P.B Johnson, R. W. Christy, Optical Constants of the Noble Metals, Phys. Rev. B. 6 (1972) 4370–4379.doi:https://doi.org/10.1103/PhysRevB.6.4370.

[59] Lord Rayleigh, On the scattering of light by small particles, Philos Mag. 41 (1871) 447–454. http://dx.doi.org/10.1017/CBO9780511703966.010 (accessed July 14, 2016).

[60] Uwe Kreigbig, Michael Vollmer, Optical Properties of Metal Clusters, 25th ed., Springer Series in

Materials Science, Verlag Berlin Heidelberg, 1995. doi:10.1007/978-3-662-09109-8.

[61] U. Hohenester, J. Krenn, Surface plasmon resonances of single and coupled metallic nanoparticles: A boundary integral method approach, Phys. Rev. B. 72 (2005) 195429. doi:10.1103/PhysRevB.72.195429.

[62] Stephan Alexander Maier, Plasmonics: Fundamentals and Applications, Springer US, Boston, MA, 2007. doi:10.1007/0-387-37825-1.

[63] G.C. Papavassiliou, OPTICAL PROPERTIES OF SMALL INORGANIC AND ORGANIC METAL PARTICLES, Prog. Solid St. Chem. 12 (n.d.) 185–271.

[64] U. Kreibig, M. Vollmer, Optical Properties of Metal Clusters, Springer Berlin Heidelberg, Berlin, Heidelberg, 1995. doi:10.1007/978-3-662-09109-8.

[65] Milton Kerker, The Scattering of Light and Other Electromagnetic Radiation, Academic Press, New York, 1969.

[66] X. Wang, Y. Li, H. Wang, Q. Fu, J. Peng, Y. Wang, J. Du, Y. Zhou, L. Zhan, Gold nanorod-based localized surface plasmon resonance biosensor for sensitive detection of hepatitis B virus in buffer, blood serum and plasma, Biosens. Bioelectron. 26 (2010) 404–410. doi:10.1016/j.bios.2010.07.121.

[67] T.J. Davis, D.E. Gómez, K.C. Vernon, Simple model for the hybridization of surface plasmon resonances in metallic nanoparticles, Nano Lett. 10 (2010) 2618–2625. doi:10.1021/nl101335z.

[68] T.R. Jensen, M.L. Duval, K. Lance Kelly, A.A. Lazarides, G.C. Schatz, R.P. Van Duyne, Nanosphere lithography: Effect of the external dielectric medium on the surface plasmon resonance spectrum of a periodic array of silver nanoparticles, J. Phys. Chem. B. 103 (1999) 9846–9853. doi:10.1021/jp9926802.

[69] M.A. Mahmoud, M.A. El-Sayed, Aggregation of gold nanoframes reduces, rather than enhances, sers efficiency due to the trade-off of the inter- and intraparticle plasmonic fields, Nano Lett. 9 (2009) 3025–3031. doi:10.1021/nl901501x.

[70] Y. Song, P.D. Nallathamby, T. Huang, H.E. Elsayed-Ali, X.-H.N. Xu, Correlation and Characterization of 3D Morphological Dependent Localized Surface Plasmon Resonance Spectra of Single Silver Nanoparticles Using Dark-field Optical Microscopy and Spectroscopy and AFM., J. Phys. Chem. C. Nanomater. Interfaces. 114 (2010) 74–81. doi:10.1021/jp9083019.

[71] J.J. Mock, M. Barbic, D.R. Smith, D.A. Schultz, S. Schultz, Shape effects in plasmon resonance of individual colloidal silver nanoparticles, J. Chem. Phys. 116 (2002) 6755. doi:10.1063/1.1462610.

[72] Y. Song, P.D. Nallathamby, T. Huang, H.E. Elsayed-Ali, X.-H.N. Xu, Correlation and Characterization of Three-Dimensional Morphologically Dependent Localized Surface Plasmon Resonance Spectra of Single Silver Nanoparticles Using Dark-Field Optical Microscopy and Spectroscopy and Atomic Force Microscopy, J. Phys. Chem. C. 114 (2010) 74–81. doi:10.1021/jp9083019.

[73] H. Chen, X. Kou, Z. Yang, W. Ni, J. Wang, Shape- and size-dependent refractive index sensitivity of gold nanoparticles, Langmuir. 24 (2008) 5233–5237. doi:10.1021/la800305j.

[74] V. Juvé, M.F. Cardinal, A. Lombardi, A. Crut, P. Maioli, J. Pérez-Juste, L.M. Liz-Marzán, N. Del

Fatti, F. Vallée, Size-dependent surface plasmon resonance broadening in nonspherical nanoparticles: single gold nanorods., Nano Lett. 13 (2013) 2234–40. doi:10.1021/nl400777y.

[75] J.H. Hodak, A. Henglein, G. V. Hartland, Size dependent properties of Au particles: Coherent excitation and dephasing of acoustic vibrational modes, J. Chem. Phys. 111 (1999) 8613. doi:10.1063/1.480202.

[76] F. Della Sala, S. D'Agostino, Handbook of molecular plasmonics, Pan Stanford, 2013.

[77] H. C. van de Hulst, Light Scattering by Small Particles, Dover, Publication, Inc., New York, 1981.

[78] G.H. Chan, J. Zhao, G.C. Schatz, R.P. Van Duyne, Localized Surface Plasmon Resonance Spectroscopy of Triangular Aluminum Nanoparticles, J. Phys. Chem. C. 112 (2008) 13958–13963. doi:10.1021/jp804088z.

[79] G.H. Chan, J. Zhao, E.M. Hicks, G.C. Schatz, R.P. Van Duyne, Plasmonic Properties of Copper Nanoparticles Fabricated by Nanosphere Lithography, Nano Lett. 7 (2007) 1947–1952. doi:10.1021/nl070648a.

[80] J.A. Creighton, D.G. Eadon, Ultraviolet–visible absorption spectra of the colloidal metallic elements, J. Chem. Soc., Faraday Trans. 87 (1991) 3881–3891. doi:10.1039/FT9918703881.

[81] C. Langhammer, Z. Yuan, I. Zorić, B. Kasemo, Plasmonic properties of supported Pt and Pd nanostructures, Nano Lett. 6 (2006) 833–838. doi:10.1021/nl060219x.

[82] J.M. Mcmahon, W. Ab, G.C. Schatz, S.K. Gray, Plasmonics in the ultraviolet with the poor metals Al, Ga, In, Sn, Tl, Pb, and Bi, Phys. Chem. Chem. Phys. Phys. Chem. Chem. Phys. 15 (2013) 5415–5423. doi:10.1039/c3cp43856b.

[83] W.A. Murray, J.R. Suckling, W.L. Barnes, Overlayers on Silver Nanotriangles: Field Confinement and Spectral Position of Localized Surface Plasmon Resonances, Nano Lett. 6 (2006) 1772–1777. doi:10.1021/nl060812e.

[84] N. Nath, A. Chilkoti, Label-Free Biosensing by Surface Plasmon Resonance of Nanoparticles on Glass: Optimization of Nanoparticle Size, Anal. Chem. 76 (2004) 5370–5378. doi:10.1021/ac049741z.

[85] K.-S. Lee, M.A. El-Sayed, Gold and Silver Nanoparticles in Sensing and Imaging: Sensitivity of Plasmon Response to Size, Shape, and Metal Composition, J. Phys. Chem. B. 110 (2006) 19220–19225. doi:10.1021/jp062536y.

[86] J.J. Mock, D.R. Smith, S. Schultz, Local Refractive Index Dependence of Plasmon Resonance Spectra from Individual Nanoparticles, Nano Lett. 3 (2003) 485–491. doi:10.1021/nl0340475.

[87] a. J. Haes, R.P. Van Duyne, A nanoscale optical biosensor: Sensitivity and selectivity of an approach based on the localized surface plasmon resonance spectroscopy of triangular silver nanoparticles, J. Am. Chem. Soc. 124 (2002) 10596–10604. doi:Article.

[88] K.M. Mayer, J.H. Hafner, Localized Surface Plasmon Resonance Sensors, Chem. Rev. 111 (2011) 3828–3857. doi:10.1021/cr100313v.

[89] Y. Sun, Y. Xia, Increased sensitivity of surface plasmon resonance of gold nanoshells compared to that of gold solid colloids in response to environmental changes, Anal. Chem. 74 (2002) 5297–5305. doi:10.1021/ac0258352.

[90] H. Chen, X. Kou, Z. Yang, W. Ni, J. Wang, Shape- and Size-Dependent Refractive Index Sensitivity of Gold Nanoparticles, Langmuir. 24 (2008) 5233–5237. doi:10.1021/la800305j.

[91] N. Verellen, P. Van Dorpe, C. Huang, K. Lodewijks, G.A.E. Vandenbosch, L. Lagae, V. V. Moshchalkov, Plasmon Line Shaping Using Nanocrosses for High Sensitivity Localized Surface Plasmon Resonance Sensing, Nano Lett. 11 (2011) 391–397. doi:10.1021/nl102991v.

[92] R. Bukasov, J.S. Shumaker-Parry, Highly Tunable Infrared Extinction Properties of Gold Nanocrescents, Nano Lett. 7 (2007) 1113–1118. doi:10.1021/nl062317o.

[93] E.M. Larsson, J. Alegret, M. Käll, D.S. Sutherland, Sensing Characteristics of NIR Localized Surface Plasmon Resonances in Gold Nanorings for Application as Ultrasensitive Biosensors, Nano Lett. 7 (2007) 1256–1263. doi:10.1021/nl0701612.

[94] C.L. Nehl, H. Liao, J.H. Hafner, Optical properties of star-shaped gold nanoparticles, Nano Lett. 6 (2006) 683–688. doi:10.1021/nl052409y.

[95] C. Yu, J. Irudayaraj, Quantitative evaluation of sensitivity and selectivity of multiplex nanoSPR biosensor assays., Biophys. J. 93 (2007) 3684–92. doi:10.1529/biophysj.107.110064.

[96] S.J. Zalyubovskiy, M. Bogdanova, A. Deinega, Y. Lozovik, A.D. Pris, K.H. An, W.P. Hall, R.A. Potyrailo, Theoretical limit of localized surface plasmon resonance sensitivity to local refractive index change and its comparison to conventional surface plasmon resonance sensor, J. Opt. Soc. Am. A. 29 (2012) 994. doi:10.1364/JOSAA.29.000994.

[97] L.J. Sherry, S.-H. Chang, G.C. Schatz, R.P. Van Duyne, B.J. Wiley, Y. Xia, Localized Surface Plasmon Resonance Spectroscopy of Single Silver Nanocubes, Nano Lett. 5 (2005) 2034–2038. doi:10.1021/nl0515753.

[98] F. Tam, C. Moran, N. Halas, Geometrical Parameters Controlling Sensitivity of Nanoshell Plasmon Resonances to, J. Phys. Chem. B. (2004) 17290–17294.

[99] K.M. Mayer, S. Lee, H. Liao, B.C. Rostro, A. Fuentes, P.T. Scully, C.L. Nehl, J.H. Hafner, A Label-Free Immunoassay Based Upon Localized Surface Plasmon Resonance of Gold Nanorods, ACS Nano. 2 (2008) 687–692. doi:10.1021/nn7003734.

[100] S. Underwood, P. Mulvaney, Effect of the Solution Refractive Index on the Color of Gold Colloids, Langmuir. 10 (1994) 3427–3430. doi:10.1021/la00022a011.

[101] J. Burgin, M. Liu, P. Guyot-Sionnest, Dielectric Sensing with Deposited Gold Bipyramids, J. Phys. Chem. C. 112 (2008) 19279–19282. doi:10.1021/jp807465p.

[102] L.J. Sherry, S.-H. Chang, G.C. Schatz, R.P. Van Duyne, B.J. Wiley, Y. Xia, Localized Surface Plasmon Resonance Spectroscopy of Single Silver Nanocubes, Nano Lett. 5 (2005) 2034–2038. doi:10.1021/nl0515753.

[103] J.J. Mock, D.R. Smith, S. Schultz, Local Refractive Index Dependence of Plasmon Resonance Spectra from Individual Nanoparticles, Nano Lett. 3 (2003) 485–491. doi:10.1021/nl0340475.

[104] Y. Khalavka, J. Becker, C. Sönnichsen, Synthesis of rod-shaped gold nanorattles with improved plasmon sensitivity and catalytic activity, J. Am. Chem. Soc. 131 (2009) 1871–1875. doi:10.1021/ja806766w.

[105] K.M. Mayer, J.H. Hafner, A.À. Antigen, Localized surface plasmon resonance sensors., Chem.

Rev. 111 (2011) 3828–57. doi:10.1021/cr100313v.

[106] J. Becker, A. Trügler, A. Jakab, U. Hohenester, C. Sönnichsen, The optimal aspect ratio of gold nanorods for plasmonic bio-sensing, Plasmonics. 5 (2010) 161–167. doi:10.1007/s11468-010-9130-2.

[107] A.J. Haes, S. Zou, G.C. Schatz, R.P. Van Duyne, Nanoscale Optical Biosensor: Short Range Distance Dependence of the Localized Surface Plasmon Resonance of Noble Metal Nanoparticles, J. Phys. Chem. B. 108 (2004) 6961–6968. doi:10.1021/jp036261n.

[108] L.S. Jung, C.T. Campbell, T.M. Chinowsky, M.N. Mar, S.S. Yee, Quantitative Interpretation of the Response of Surface Plasmon Resonance Sensors to Adsorbed Films, Langmuir. 14 (1998) 5636–5648. doi:10.1021/la971228b.

[109] S.R. Beeram, F.P. Zamborini, Selective Attachment of Antibodies to the Edges of Gold Nanostructures for Enhanced Localized Surface Plasmon Resonance Biosensing, J. Am. Chem. Soc. 131 (2009) 11689–11691. doi:10.1021/ja904387j.

[110] A.J. Haes, W.P. Hall, L. Chang, W.L. Klein, R.P. Van Duyne, A Localized Surface Plasmon Resonance Biosensor: First Steps toward an Assay for Alzheimer's Disease, Nano Lett. 4 (2004) 1029–1034. doi:10.1021/nl049670j.

[111] N. Nath, A. Chilkoti, A colorimetric gold nanoparticle sensor to interrogate biomolecular interactions in real time on a surface., Anal. Chem. 74 (2002) 504–9. http://www.ncbi.nlm.nih.gov/pubmed/11838667 (accessed August 16, 2016).

[112] S.R. Beeram, F.P. Zamborini, Purification of Gold Nanoplates Grown Directly on Surfaces for Enhanced Localized Surface Plasmon Resonance Biosensing, ACS Nano. 4 (2010) 3633–3646. doi:10.1021/nn1007397.

[113] S.M. Marinakos, S. Chen, A. Chilkoti, Plasmonic Detection of a Model Analyte in Serum by a Gold Nanorod Sensor, Anal. Chem. 79 (2007) 5278–5283. doi:10.1021/ac0706527.

[114] C. Yu, J. Irudayaraj, Multiplex Biosensor Using Gold Nanorods, Anal. Chem. 79 (2007) 572–579. doi:10.1021/ac061730d.

[115] R. V Olkhov, J.D. Fowke, A.M. Shaw, Whole serum BSA antibody screening using a label-free biophotonic nanoparticle array., Anal. Biochem. 385 (2009) 234–41. doi:10.1016/j.ab.2008.10.042.

[116] N. Sakai, Y. Fujiwara, M. Arai, K. Yu, T. Tatsuma, Electrodeposition of gold nanoparticles on ITO: Control of morphology and plasmon resonance-based absorption and scattering, J. Electroanal. Chem. 628 (2009) 7–15. doi:10.1016/j.jelechem.2008.12.008.

[117] G. Raschke, S. Kowarik, T. Franzl, C. Sönnichsen, T.A. Klar, J. Feldmann, A. Nichtl, K. Kürzinger, Biomolecular Recognition Based on Single Gold Nanoparticle Light Scattering, Nano Lett. 3 (2003) 935–938. doi:10.1021/nl034223+.

[118] G.J. Nusz, S.M. Marinakos, A.C. Curry, A. Dahlin, F. Höök, A. Wax, A. Chilkoti, Label-free plasmonic detection of biomolecular binding by a single gold nanorod., Anal. Chem. 80 (2008) 984–9. doi:10.1021/ac7017348.

[119] C.D. Geddes, J.R. Lakowicz, Editorial: Metal-Enhanced Fluorescence, J. Fluoresc. 12 (2002) 121–129. doi:10.1023/A:1016875709579.

[120] K. Aslan, I. Gryczynski, J. Malicka, E. Matveeva, J.R. Lakowicz, C.D. Geddes, Metal-enhanced fluorescence: an emerging tool in biotechnology, Curr. Opin. Biotechnol. 16 (2005) 55–62. doi:10.1016/j.copbio.2005.01.001.

[121] K. Aslan, I. Gryczynski, J. Malicka, E. Matveeva, J.R. Lakowicz, C.D. Geddes, Metal-enhanced fluorescence: An emerging tool in biotechnology, Curr. Opin. Biotechnol. 16 (2005) 55–62. doi:10.1016/j.copbio.2005.01.001.

[122] P.P. Pompa, L. Martiradonna, A. Della Torre, F. Della Sala, L. Manna, M. De Vittorio, F. Calabi, R. Cingolani, R. Rinaldi, Metal-enhanced fluorescence of colloidal nanocrystals with nanoscale control, Nat. Nanotechnol. 1 (2006) 126–130. doi:10.1038/nnano.2006.93.

[123] C.D. Geddes, A. Parfenov, D. Roll, I. Gryczynski, J. Malicka, J.R. Lakowicz, Silver Fractal-like Structures for Metal-Enhanced Fluorescence: Enhanced Fluorescence Intensities and Increased Probe Photostabilities., J. Fluoresc. 13 (2003) 267–276. doi:10.1023/A:1025046101335.

[124] J.R. Lakowicz, Radiative Decay Engineering: Biophysical and Biomedical Applications, Anal. Biochem. 298 (2001) 1–24. doi:10.1006/abio.2001.5377.

[125] E. Fort, S. Grésillon, Surface enhanced fluorescence, J. Phys. D Appl. Phys. J. Phys. D Appl. Phys. 41 (2008) 13001–31. doi:10.1088/0022-3727/41/1/013001.

[126] Valeur Bernard, Bernard Valeur Molecular Fluorescence Principles and Applications, Fluoresc. Mol. Princ. , Appl. (n.d.).

[127] Claude Schweitzer, Reinhard Schmid, Physical Mechanisms of Generation and Deactivation of Singlet Oxygen, Chem. Rev. 103 (2003) 1685–1757.

[128] Nicholas J. Turro, Modern Molecular Photochemistry, University Science Books, 1991.

[129] H. Kautsky, H. de Bruijn, Die Aufklärung der Photoluminescenztilgung fluorescierender Systeme durch Sauerstoff: Die Bildung aktiver, diffusionsfähiger Sauerstoffmoleküle durch Sensibilisierung, Naturwissenschaften. 19 (1931) 1043–1043. doi:10.1007/BF01516190.

[130] J.G. Moser, Photodynamic tumor therapy : 2nd and 3rd generation photosensitizers, Harwood Academic Publishers, 1998.

[131] J.P. Tardivo, A. Del Giglio, C.S. De Oliveira, D.S. Gabrielli, H.C. Junqueira, D.B. Tada, D. Severino, R. De F??tima Turchiello, M.S. Baptista, Methylene blue in photodynamic therapy: From basic mechanisms to clinical applications, Photodiagnosis Photodyn. Ther. 2 (2005) 175–191. doi:10.1016/S1572-1000(05)00097-9.

[132] S. Perni, C. Piccirillo, J. Pratten, P. Prokopovich, W. Chrzanowski, I.P. Parkin, M. Wilson, The antimicrobial properties of light-activated polymers containing methylene blue and gold nanoparticles, Biomaterials. 30 (2009) 89–93. doi:10.1016/j.biomaterials.2008.09.020.

[133] M. Wainwright, D.A. Phoenix, L. Rice, S.M. Burrow, J. Waring, Increased cytotoxicity and phototoxicity in the methylene blue series via chromophore methylation, J. Photochem. Photobiol. B Biol. 40 (1997) 233–239. doi:10.1016/S1011-1344(97)00061-4.

[134] R.W. Redmond, J.N. Gamlin, A compilation of singlet oxygen yields from biologically relevant molecules., Photochem. Photobiol. 70 (1999) 391–475. http://www.ncbi.nlm.nih.gov/pubmed/10546544 (accessed May 29, 2017).

[135] Y. Zhang, K. Aslan, M.J.R. Previte, C.D. Geddes, Metal-enhanced singlet oxygen generation: a consequence of plasmon tripplet yields, J.Fluoresc. 17(2007) 345-349. doi:10.1007/s108-007-0196-y.

[136] A.M. Fales, H. Yuan, T. Vo-Dinh, Silica-Coated Gold Nanostars for Combined Surface-Enhanced Raman Scattering (SERS) Detection and Singlet-Oxygen Generation: A Potential Nanoplatform for Theranostics, Langmuir. 27 (2011) 12186–12190. doi:10.1021/la202602q.

[137] Z. Ren, X. Li, J. Guo, R. Wang, Y. Wu, M. Zhang, C. Li, Solution-based metal enhanced fl uorescence with gold and gold / silver core – shell nanorods, 357 (2015) 156–160.

[138] A.M. Fales, H. Yuan, T. Vo-Dinh, Silica-coated gold nanostars for combined SERS Detection and singlet oxygen generation: a potential nanoplatform for theranostics, Lang. 27 (2011) 12186–12190. doi:10.1016/j.pestbp.2011.02.012.Investigations.

[139] Y. Zhang, K. Aslan, M.J.R. Previte, C.D. Geddes, Plasmonic engineering of singlet oxygen generation, Proc. Natl. Acad. Sci. 105 (2008) 1798–1802. doi:10.1073/pnas.0709501105.

[140] A.J. Haes, L. Chang, W.L. Klein, R.P. Van Duyne, Detection of a Biomarker for Alzheimer's Disease from Synthetic and Clinical Samples Using a Nanoscale Optical Biosensor, J. Am. Chem. Soc. 127 (2005) 2264–2271. doi:10.1021/ja044087q.

[141] J.L. Hammond, N. Bhalla, S.D. Rafiee, P. Estrela, Localized Surface Plasmon Resonance as a Biosensing Platform for Developing Countries, Biosensors. 4 (2014) 172–188. doi:10.3390/bios4020172.

[142] K. Takemura, O. Adegoke, N. Takahashi, T. Kato, T.-C. Li, N. Kitamoto, T. Tanaka, T. Suzuki, E.Y. Park, Versatility of a localized surface plasmon resonance-based gold nanoparticle-alloyed quantum dot nanobiosensor for immunofluorescence detection of viruses, Biosens. Bioelectron. 89 (2017) 998–1005. doi:10.1016/j.bios.2016.10.045.

[143] L. Xu, Y. Liu, Z. Chen, W. Li, Y. Liu, L. Wang, Y. Liu, X. Wu, Y. Ji, Y. Zhao, L. Ma, Y. Shao, C. Chen, Surface-engineered gold nanorods: Promising DNA vaccine adjuvant for HIV-1 treatment, Nano Lett. 12 (2012) 2003–2012. doi:10.1021/nl300027p.

[144] A.R. Camara, P.M.P. Gouvêa, A.C.M.S. Dias, A.M.B. Braga, R.F. Dutra, R.E. de Araujo, I.C.S. Carvalho, Dengue immunoassay with an LSPR fiber optic sensor, Opt. Express. 21 (2013) 27023. doi:10.1364/OE.21.027023.

[145] W. Hong, F. Liang, D. Schaak, M. Loncar, Q. Quan, Nanoscale Label-free Bioprobes to Detect Intracellular Proteins in Single Living Cells, Sci. Rep. 4 (2014) 6179. doi:10.1038/srep06179.

[146] M. Duval Malinsky, L. Kelly, G.C. Schatz, R.P. Van Duyne, Chain length dependence and sensing capabilities of the localized surface plasmon resonance of silver nanoparticles chemically modified with alkanethiol self-assembled monolayers, J. Am. Chem. Soc. 123 (2001) 1471. http://dx.doi.org/10.1021/ja003312a.

[147] K.M. Mayer, J.H. Hafner, Localized Surface Plasmon Resonance Sensors, Chem. Rev. 111 (2011) 3828–3857. doi:10.1021/cr100313v.

[148] S. Lee, K.M. Mayer, J.H. Hafner, Improved Localized surface plasmon resonance Immunoassay with gold bipyramid Substrates, Anal.Chem. 81 (2009) 4450–4455. doi:10.1021/ac900276n.

[149] J. Homola, S.S. Yee, G. Gauglitz, Y. Sun, X. Fan, J. Homola, S.S. Yee, G. Gauglitz, Surface plasmon resonance sensors: review, Sensors Actuators B Chem. 54 (1999) 3–15. doi:10.1016/S0925-4005(98)00321-9.

[150] L. Tong, H. Wei, S. Zhang, H. Xu, Recent advances in plasmonic sensors, Sensors (Basel). 14 (2014) 7959–7973. doi:10.3390/s140507959.

[151] J.N. Anker, W.P. Hall, O. Lyandres, N.C. Shah, J. Zhao, R.P. Van Duyne, Biosensing with plasmonic nanosensors, Nat. Mater. 7 (2008) 442–453. doi:10.1038/nmat2162.

[152] P.B. Johnson, R.W. Christy, Optical Constants of the Noble Metals, Phys. Rev. B. 6 (1972) 4370–4379. doi:10.1103/PhysRevB.6.4370.

[153] https://oceanoptics.com/knowledge-support/example-setups/, (n.d.).

[154] G. Barbillon, Determination of Evanescent Electric Field Decay Length of Metallic Nanodisks by Using Localized Surface Plasmon Spectroscopy, J. Mater. Sci. Eng. 4 (2010) 1934–8959. http://www.davidpublishing.com/davidpublishing/Upfile/7/31/2014/2014073166764797.pdf (accessed March 20, 2017).

[155] E. Martinsson, M.A. Otte, M.M. Shahjamali, B. Sepulveda, D. Aili, Substrate Effect on the Refractive Index Sensitivity of Silver Nanoparticles, J. Phys. Chem. C. 118 (2014) 24680–24687. doi:10.1021/jp5084086.

[156] J. Ye, C. Chen, W. Van Roy, P. Van Dorpe, G. Maes, G. Borghs, The fabrication and optical property of silver nanoplates with different thicknesses., Nanotechnology. 19 (2008) 325702. doi:10.1088/0957-4484/19/32/325702.

[157] G.Barbillon, J.-L.Bijeon, J.-S.Bouillard, J.Plain, M.L. de la Chapelle, P.-M.Adam, P.Royer, Detection of biomolecules in near-field domain adsorbed on a single metallic nanoparticle, J. Microsc. 229 (2007) 270–274.

[158] Y. Shen, J. Zhou, T. Liu, Y. Tao, R. Jiang, M. Liu, G. Xiao, J. Zhu, Z.-K. Zhou, X. Wang, C. Jin, J. Wang, Plasmonic gold mushroom arrays with refractive index sensing figures of merit approaching the theoretical limit, Nat. Commun. 4 (2013) 1102–1110. doi:10.1038/ncomms3381.

[159] M.A. Otte, B. Sepulveda, Figures of Merit for Refractometric LSPR Biosensing, in: Nanoplasmonic Sensors, Springer New York, New York, NY, 2012: pp. 317–331. doi:10.1007/978-1-4614-3933-2_13.

[160] R. Morarescu, H. Shen, R.A.L.R. a. L. Vallée, B. Maes, B. Kolaric, P. Damman, Exploiting the localized surface plasmon modes in gold triangular nanoparticles for sensing applications, J. Mater. Chem. 22 (2012) 11537. doi:10.1039/c2jm30944k.

[161] K.-S. Lee, M.A. El-Sayed, Gold and Silver Nanoparticles in Sensing and Imaging: Sensitivity of Plasmon Response to Size, Shape, and Metal Composition, J. Phys. Chem. B. 110 (2006) 19220–19225. doi:10.1021/jp062536y.

[162] M.A. Mahmoud, M. Chamanzar, A. Adibi, M.A. El-Sayed, Effect of the Dielectric Constant of the Surrounding Medium and the Substrate on the Surface Plasmon Resonance Spectrum and Sensitivity Factors of Highly Symmetric Systems: Silver Nanocubes, J. Am. Chem. Soc. 134 (2012) 6434–6442. doi:10.1021/ja300901e.

[163] B.K. Shrestha, A.J. Haes, Improving surface enhanced Raman signal reproducibility using gold-coated silver nanospheres encapsulated in silica membranes, J. Opt. 17 (2015) 114017. doi:10.1088/2040-8978/17/11/114017.

[164] J.J. Mock, D.R. Smith, S. Schultz, Local Refractive Index Dependence of Plasmon Resonance Spectra from Individual Nanoparticles, Nano Lett. 3 (2003) 485–491. doi:10.1021/nl0340475.

[165] A. Jakab, C. Rosman, Y. Khalavka, J. Becker, A. Trügler, U. Hohenester, C. Sönnichsen, Highly sensitive plasmonic silver nanorods, ACS Nano. 5 (2011) 6880–6885. doi:10.1021/nn200877b.

[166] S. Perni, P. Prokopovich, J. Pratten, I.P. Parkin, M. Wilson, Nanoparticles: their potential use in antibacterial photodynamic therapy., Photochem. Photobiol. Sci. 10 (2011) 712–720. doi:10.1039/c0pp00360c.

[167] K. Patil, R. Pawar, P. Talap, Self-aggregation of Methylene Blue in aqueous medium and aqueous solutions of Bu4NBr and urea, Phys. Chem. Chem. Phys. 2 (2000) 4313–4317. doi:10.1039/b005370h.

[168] T. Härtling, P. Reichenbach, L.M. Eng, Near-field coupling of a single fluorescent molecule and a spherical gold nanoparticle, Opt. Express. 15 (2007) 12806–12817. doi:10.1364/OE.15.012806.

[169] P. Anger, P. Bharadwaj, L. Novotny, Enhancement and quenching of single-molecule fluorescence, Phys. Rev. Lett. 96 (2006) 3–6. doi:10.1103/PhysRevLett.96.113002.

[170] K.A. Kang, J. Wang, J.B. Jasinski, S. Achilefu, Fluorescence Manipulation by Gold Nanoparticles: From Complete Quenching to Extensive Enhancement, J. Nanobiotechnology. 9 (2011) 16. doi:10.1186/1477-3155-9-16.

[171] Y. Zhang, K. Aslan, M.J.R. Previte, C.D. Geddes, Plasmonic engineering of singlet oxygen generation, Proc. Natl. Acad. Sci. 105 (2008) 1798–1802. doi:10.1073/pnas.0709501105.

[172] L.S.A. de Melo, A.S.L. Gomes, S. Saska, K. Nigoghossian, Y. Messaddeq, S.J.L. Ribeiro, R.E. de Araujo, Singlet Oxygen Generation Enhanced by Silver-Pectin Nanoparticles, J. Fluoresc. 22 (2012) 1633–1638. doi:10.1007/s10895-012-1107-4.

[173] L.R. Hirsch, N.J. Halas, J.L. West, Whole-Blood Immunoassay Facilitated by Gold Nanoshell–Conjugate Antibodies, in: NanoBiotechnology Protoc., Humana Press, New Jersey, 2005: pp. 101–112. doi:10.1385/1-59259-901-X:101.

[174] R. Sun, M. Wan, W. Wu, P. Gu, Z. Chen, Z. Wang, Shaping the photoluminescence from gold nanoshells by cavity plasmons in dielectric-metal core-shell resonators, AIP Adv. 6 (2016) 85216. doi:10.1063/1.4961727.

[175] S. Phadtare, A. Kumar, V.P. Vinod, C. Dash, D. V. Palaskar, M. Rao, P.G. Shukla, S. Sivaram, M. Sastry, Direct Assembly of Gold Nanoparticle “Shells” on Polyurethane Microsphere “Cores” and Their Application as Enzyme Immobilization Templates, Chem. Mater. 15 (2003) 1944–1949. doi:10.1021/cm020784a.

[176] S.J. Oldenburg, S.L. Westcott, R.D. Averitt, N.J. Halas, Surface enhanced Raman scattering in the near infrared using metal nanoshell substrates, J. Chem. Phys. (1999). doi:10.1063/1.479235.

[177] J.H. LEE, W. PARK, THREE-DIMENSIONAL METALLIC PHOTONIC CRYSTAL BASED ON SELF-ASSEMBLED GOLD NANOSHELLS, Funct. Mater. Lett. 1 (2008) 65–69.

doi:10.1142/S1793604708000125.

[178] F. Mohammad, G. Balaji, A. Weber, R.M. Uppu, C.S.S.R. Kumar, Influence of Gold Nanoshell on Hyperthermia of Superparamagnetic Iron Oxide Nanoparticles, J. Phys. Chem. C. 114 (2010) 19194–19201. doi:10.1021/jp105807r.

[179] W. Li, X. Chen, Gold nanoparticles for photoacoustic imaging., Nanomedicine (Lond). 10 (2015) 299–320. doi:10.2217/nnm.14.169.

[180] J.C.Y. Kah, M. Olivo, T.H. Chow, K.S. Song, K.Z.Y. Koh, S. Mhaisalkar, C.J.R. Sheppard, Control of optical contrast using gold nanoshells for optical coherence tomography imaging of mouse xenograft tumor model in vivo, J. Biomed. Opt. 14 (2009) 54015. doi:10.1117/1.3233946.

[181] C.L. Nehl, N.K. Grady, G.P. Goodrich, F. Tam, N.J. Halas, J.H. Hafner, Scattering Spectra of Single Gold Nanoshells, Nano Lett. 4 (2004) 2355–2359. doi:10.1021/nl048610a.

[182] F. Tam, G.P. Goodrich, B.R. Johnson, N.J. Halas, Plasmonic Enhancement of Molecular Fluorescence, Nano Lett. 7 (2007) 496–501. doi:10.1021/nl062901x.

[183] C. Loo, A. Lowery, N. Halas, J. West, R. Drezek, Immunotargeted Nanoshells for Integrated Cancer Imaging and Therapy, Nano Lett. 5 (2005) 709–711. doi:10.1021/nl050127s.

[184] S. Link, M.A. El-Sayed, Size and Temperature Dependence of the Plasmon Absorption of Colloidal Gold Nanoparticles, J. Phys. Chem. B. 103 (1999) 4212–4217. doi:10.1021/jp984796o.

[185] A.L. Feng, M.L. You, L. Tian, S. Singamaneni, M. Liu, Z. Duan, T.J. Lu, F. Xu, M. Lin, Distance-Dependent Plasmon-Enhanced Fluorescence of Upconversion Nanoparticles using Polyelectrolyte Multilayers as Tunable Spacers, Sci. Rep. 5 (2015) 7779. doi:10.1038/srep07779.

[186] J. Dong, H. Zheng, H. Shao, Z. Zhang, G. Liu, S.-X. Qu, Surface enhanced fluorescence of physically polished nanostructured metal surface: the effect of the native oxide layer., J. Nanosci. Nanotechnol. 11 (2011) 9626–30. http://www.ncbi.nlm.nih.gov/pubmed/22413259 (accessed March 27, 2017).

[187] Y. Zhang, K. Aslan, M.J.R. Previte, C.D. Geddes, Metal-enhanced singlet oxygen generation: A consequence of plasmon enhanced triplet yields, J. Fluoresc. 17 (2007) 345–349. doi:10.1007/s10895-007-0196-y.

[188] M.N.O. Sadiku, A simple introduction to finite element analysis of electromagnetic problems, IEEE Trans. Educ. 32 (1989) 85–93. doi:10.1109/13.28037.

[189] F. Le, D.W. Brandl, Y.A. Urzhumov, H. Wang, J. Kundu, N.J. Halas, J. Aizpurua, P. Nordlander, Metallic Nanoparticle Arrays: A Common Substrate for Both Surface-Enhanced Raman Scattering and Surface-Enhanced Infrared Absorption, ACS Nano. 2 (2008) 707–718. doi:10.1021/nn800047e.

[190] https://br.comsol.com/multiphysics/finite-element-method, (n.d.).

[191] D.K. (David K. Cheng, Field and wave electromagnetics, Addison-Wesley, 1989.

[192] J. Zhao, A.O. Pinchuk, J.M. Mcmahon, S. Li, L.K. Ausman, A.L. Atkinson, G.C. Schatz, Methods for Describing the Electromagnetic Properties of Silver and Gold Nanoparticles, Chem. Soc. Rev. 41 (2008) 1710–1720.

APPENDIX- A - FINITE ELEMENT METHOD AND COMSOL MULTIPHYSICS

The laws of physics for space and time dependent are usually described by partial differentiation equations (PDEs). Due to complex geometries and problems, such PDEs cannot be resolved using analytical methods. Therefore, an approximation of these PDEs can be constructed which is based on various types of discretization. Discretization involves dividing the region into subdomains [188]. These discretizations approximations can be solved with numerical model equations. Consequently, these solutions based on numerical model equations are an approximation to the real solutions of PDEs. The finite element method, thus, is employed to compute such approximations. The numerical calculations used by COMSOL Multiphysics, is based on the FEM. FEM is standard method to solve the partial differential equations and EM fields are expanded to the finite elements. Maxwell's equations are used to convert into the matrix equations and these equations are solved by iterative and direct methods [189]. The FEM analysis of any problem includes basically four steps: (1) discrete the solution region into finite number of elements or sub-regions, (2) deriving governing equations for a typical element, (3) assembling of all elements in the solution region, (4) and solving the system of equations obtained. For instance, consider a function *u* that may be dependent variable in PDE (i.e. pressure, electric potential, temperature, etc.) [188]. The function *u* can be approximated by a function u_i using linear combinations of basis functions according to the following relations :

$$u = u_i \tag{A1}$$

$$u_i = \sum_j u_j \psi_j \tag{A2}$$

where u_j represents the coefficient of the functions that approximate *u* with u_i and ψ_j denotes the basis functions. For example, the figure A. 1 shows this principle for for 1-D problem. *u* could, for example, presents the temperature along length , x, of a rod that is non-uniformly heated.

Figure A. 1: The function u (solid-blue line) is approximated with u_i (dashed-red line), which is a linear combination of linear basis functions (ψ_i) and is represented by the solid black lines). The coefficients are denoted by u_0 through u_7 (a), while the coefficients are represented by u_0 to u_9 (b).

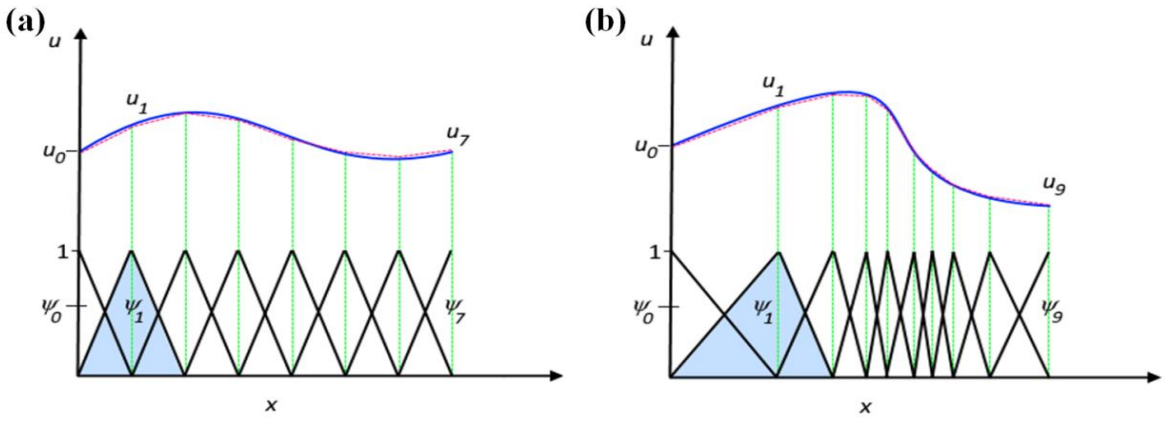

Source: adopted from [190]

The linear basis functions have a value of 1 at their respective nodes and 0 at other nodes. In this case, the seven elements involve along the portion of x axis (i.e. the length of the rod) where the function u is defined. One of the advantages of using FEM is that it provides great freedom of discretization, both in the elements that may be used to discretize the basis and space functions. For example, the elements are uniformly divided over the x-axis, albeit this does not have to be the case, as shown in fig A.1(a). However, smaller elements in a region where gradient of function u is large could have been applied as seen in figure A. 1(b). It is apparent that figure A. 1(a) and (b) show the linear basis functions involve very limited support (non-zero only over the narrow interval) and overlap along the x-axis. Another advantage of FEM is, the theory is well developed. Also depending on the complex problem at hand, other functions may be chosen instead of the linear functions. For example, the theory provides useful error estimates or bounds for the error, when numerical model equations are solved on the computer.

Maxwell's equations can be solved by FEM. Maxwell's equations relate the electric charge density (ρ), electric field (E), electric field displacement (D), current density (J) as well as magnetic field intensity (H) and magnetic flux density (B) as [191]:

$$\nabla \cdot \vec{D} = \rho \tag{A3}$$

$$\nabla \cdot \vec{B} = 0 \tag{A4}$$

$$\nabla \times \vec{E} = \frac{\partial \vec{B}}{\partial t} \tag{A5}$$

$$\nabla \times \vec{H} = \vec{J} + \frac{\partial \vec{D}}{\partial t} \tag{A6}$$

In order to solve these equations (A3-6), a set of boundary conditions and material constitutive relations are required. The material constitutive relations relate between $\vec{J}$ to $\vec{E}$ field, $\vec{E}$ to $\vec{D}$ field and $\vec{B}$ to $\vec{H}$ field, and express as [191]:

$$\vec{D} = \epsilon_0 \vec{E} + \vec{P} \tag{A7}$$

$$\vec{B} = \mu_0(\vec{H} + \vec{M}) \tag{A8}$$

$$\vec{J} = \sigma \vec{E} \tag{A9}$$

where ϵ_0 and μ_0 are permittivity and permeability in free space and σ is electric conductivity. The polarization ($\vec{P}$) for linear material is proportional to electric displacement i.e. $\vec{P} = \epsilon_0 \chi_e \vec{E}$ where χ_e is the electric susceptibility. Magnetization ($\vec{M}$) in linear material is also related to magnetic field $\vec{H}$ and given as $\vec{M} = \chi_m \vec{H}$ where χ_m is the magnetic susceptibility. The theoretical formulation of the Radio Frequency (RF) Module or Optical Wave Module presents the electromagnetic analysis at a macroscopic level involving Maxwell's equations at certain boundary conditions. The Electromagnetic Waves, frequency domain in both Wave Optics Module or RF module is typically based on the solution of inhomogeneous wave equation; the governing Maxwell's equations are reduced as [192]:

$$\vec{\nabla} \times \left[\frac{1}{\mu_r}\vec{\nabla} \times \vec{E}\right] - \omega^2 \epsilon_0 \mu_0 (\epsilon_r - \frac{j\sigma}{\omega \epsilon_0})\vec{E} = 0 \tag{A10}$$

where ϵ_r and μ_r are the material properties i.e. material relative permittivity and relative permeability respectively.

In this research, direct method is used to solve various shapes and size of gold or silver nanostructures in homogeneous medium. The background oscillating field of arbitrary amplitude

was set to 1 Vm^{-1}. A perfectly matched layer (PML) additionally incorporated to avoid any reflection artifacts during the simulation and extinction cross sections as well as normal electric field were calculated within a range of wavelength.

COMSOL simulation was executed using the procedure which contained the following steps as:

1 Global

Global Settings

Name	**Gold Nanoparticle**
Path	D:\COMSOL\Gold Nanoparticle.mph
Unit System	SI

Used Products

COMSOL Multiphysics
Radio Frequency (RF) Module

1.1 Global Definitions

1.1.1 Parameters

Name	**Expression**	**Unit**	**Description**
E0	1 [V/m]	1 V/m	Electric Field
r	10 [nm]	0.1 E-7	Radius of NP
λi	500 [nm]	5.0 E-7 m	Initial wavelength
k	2*π/λi	1.2566 E7 1/m	Wavenumber
f	c_const/ λi	5.9958 1/s	frequency
r_pml	500 [nm]	5.0 E-7 m	Radius of PML
t_pml	200 [nm]	2.0 E-7 m	Thickness of PML
n_medium	1.33	1.33	Surrounding medium
Lambda_step	1 [nm]	0.01 E-7 m	Step size
Sigma_geom	π*r^2	3.1416 E-16 m^2	Geometric cross section
S_in	((E0^2)*n_medium)/(2*Z0_const)		Scaling factor

1.1.2 Functions

- Interpolation 1

Function Name	eps_r
Function type	Interpolation

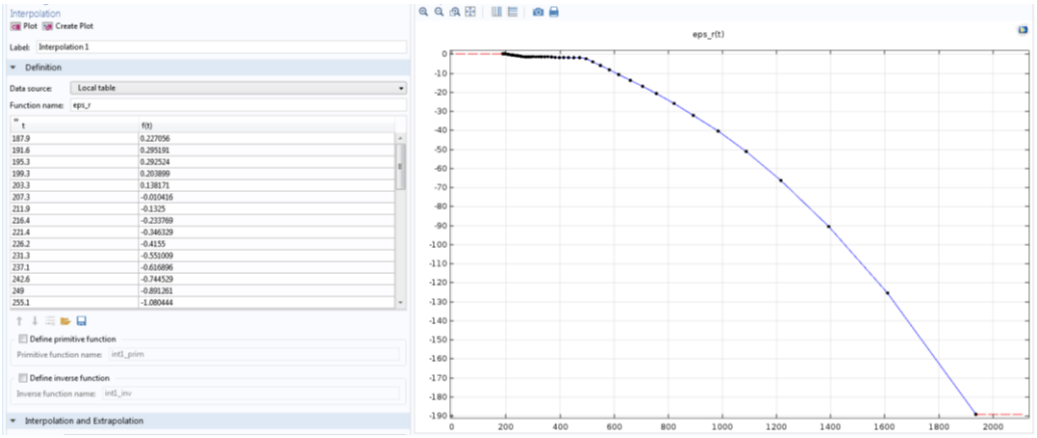

- Interpolation 2

Function Name	eps_i
Function type	Interpolation

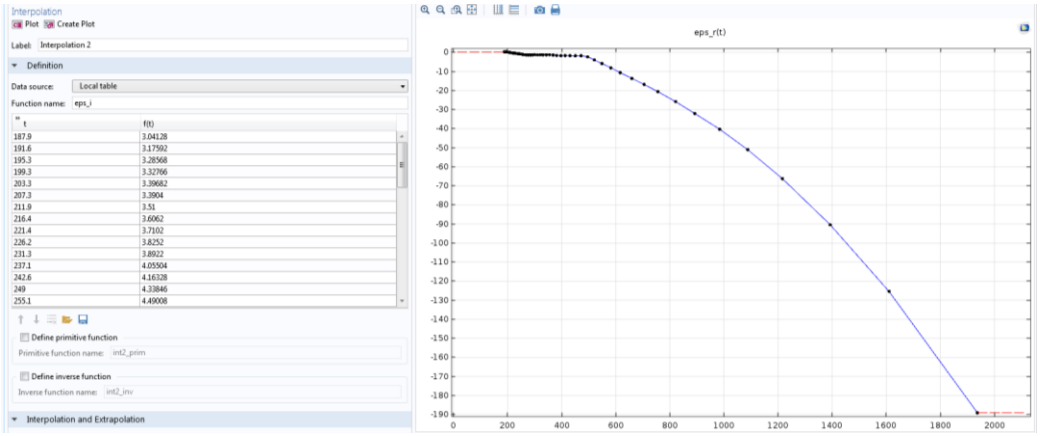

2 Component

2.1 Definations

2.1.1 Variables

Name	Expression	Unit	Description
nrelPoav	nx*emw.relPoavx+ny*emw.relPoavy+nz*emw.relPoavz	W/m^2	
sigma_sc	intop_surf(nrelPoav)/S_in	m^2	
sigma_abs	intop_vol(emw.Qh)/S_in	m^2	
sigma_ext	sigma_sc+sigma_abs	m^2	
nsigma_sc	(intop_surf(nrelPoav)/S_in)/sigma_geom		

2.1.2 Integration

Integration 1

Operator name	Intop_vol
Nanoparticle	Domain 6

Integration 2

Operator name	Intop_surf
Nanoparticle	Domain 9-12, 22, 23, 29, 34

2.1.3 Physical Domain

- Explicit

Physical domain

Label	Physical domain
Geometric entity level	Domain 5, 6

2.1.4 PML Domain

- Complement

PML domain

Label	PML domain
Geometric entity level	Physical domain

2.1.5 Nanoparticle

- Explicit

Nanoparticle

Label	Nanoparticle
Geometric entity level	Domain 6

2.1.5 Nanoparticle

- Explicit

Nanoparticle Surface

Label	Nanoparticle surface
Geometric entity level	Boundary 9-12, 22, 23, 29, 34

2.1.5 External PML Surface

- Explicit

External PML Surface

Label	External PML surface
Geometric entity level	Boundary 5-8, 20, 21, 28, 34

2.1.5 Internal PML Surface

- Explicit

Internal PML Surface

Label	Internal PML surface
Geometric entity level	Boundary 9-12, 22, 23, 29, 34,

2.1.5 Perfectly Matched Layer 1 (*pml*1)

- Perfectly Matched Layer

Internal PML Surface

Name	*pml*1
Domain selection	PML domain
Type	Spherical
Center Coordinate	*x*,*y*,*z* (0,0,0)
Physics	EM Waves, Frequency Domain (emw)
PML Scaling Factor	0.5

3 Geometry

Label	Size	Thickness
Sphere 1	r	
Sphere 2	r_pml	t_pml

Figure A. 2- The 3D geometry of AuNP surrounded by PML layer.

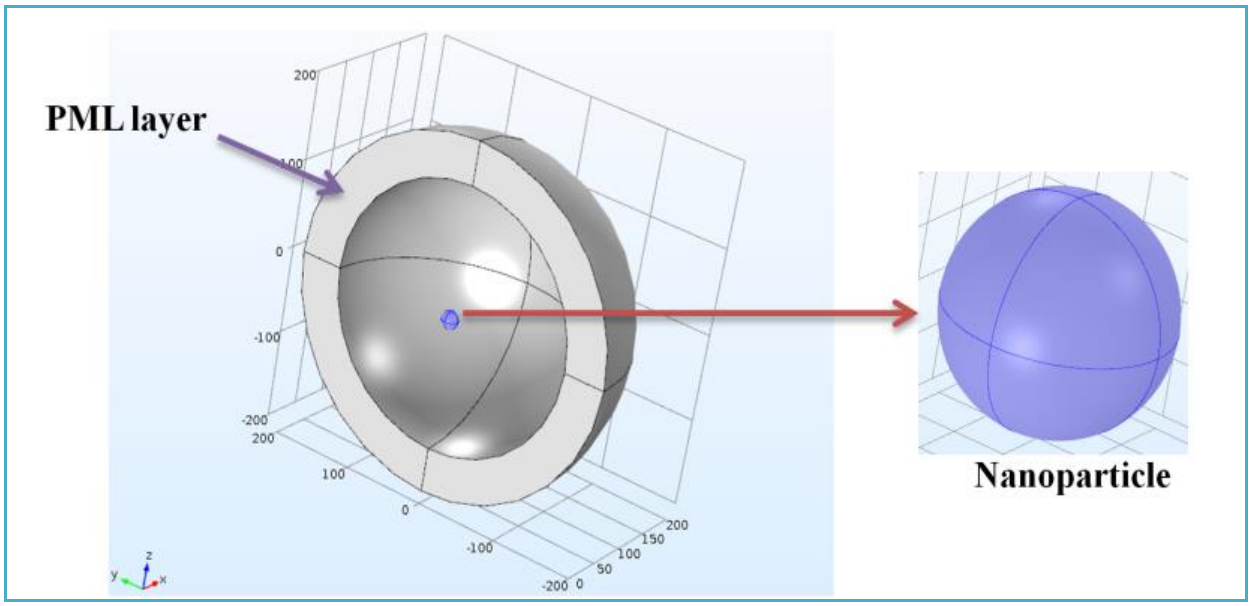

Source: belong to author

4 Material

4.1 Water

Setting

Label	Water
Geometric entity level	Domain 1-11 (all-domain)

Water Selection

Figure A. 3: The water (blue) around the AuNP.

Material Contents

Property	Name	Value	Unit	Property group
Relative permeability	mur	1	1	Basic
Relative permittivity	epsilonr	(1.33)^2	1	Basic
Electrical conductivity	sigma	0[S/m]	S/m	Basic
Dynamic viscosity	mu	eta(T[1/K]...	Pa·s	Basic
Ratio of specific heats	gamma	1.4	1	Basic
Heat capacity at constant pressure	Cp	Cp(T[1/K])...	J/(kg·K)	Basic
Density	rho	rho(pA[1/...	kg/m³	Basic
Thermal conductivity	k	k(T[1/K])[...	W/(m·K)	Basic
Speed of sound	c	cs(T[1/K])[...	m/s	Basic
Refractive index, real part	n	1	1	Refractive index
Refractive index, imaginary part	ki	0	1	Refractive index

Appearance

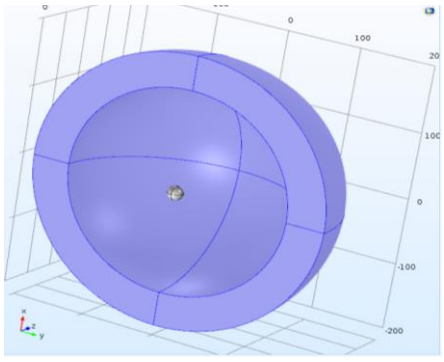

Source: belong to author

4.2 Dielectric Functions of Gold

Setting

Label	Gold Nanoparticle
Geometric entity level	Domain 6 (Nanoparticle)

Gold Selection

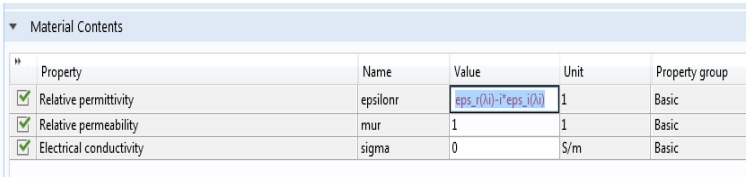

5 Electromagnetic Waves, Frequency Domain

Electromagnetic Waves, Frequency Domain

Name	emw
Domain selection	All domains
Equation form	Study control
Solve for	Scattered field
Equation	Eq. (10)

Background Electric Field

E0*exp(-j*(2*pi/(λ1[nm]))*n_medium*z)	x	V/m
0	y	
0	z	

- Wave Equation, Electric 1
- Perfect Electric Conductor 1
- Initial Value 1
- Scattering Boundary Condition

6 Mesh

6.1 Free Triangular 1

Label	Free Triangular
Geometric entity level	Boundary
Selection	External PML surface
Size	Finer

6.2 Swept

Label	Swept 1
Geometric entity level	Domain
Selection	PML domain

Distribution	All domain
Number of elements	8

6.3 Free Tetrahedral 1

Label	Free Tetrahedral 1
Geometric entity level	Boundary
Selection	Nanoparticle surface
Size	Finer

Figure A. 4- The 3D Mesh Pattern for AuNP for FEM simulation.

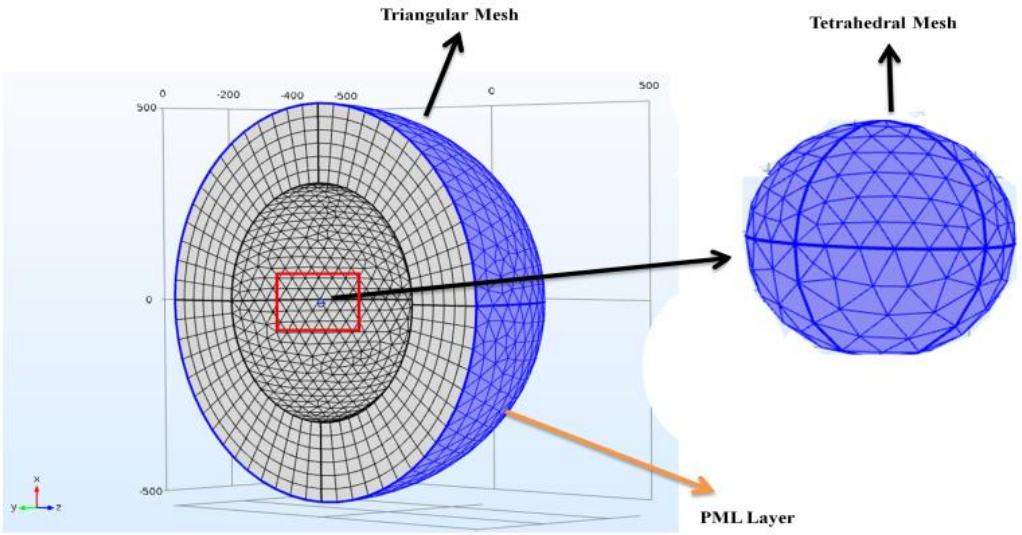

Source: belong to author

7 Study

7.1 Parametric Sweep

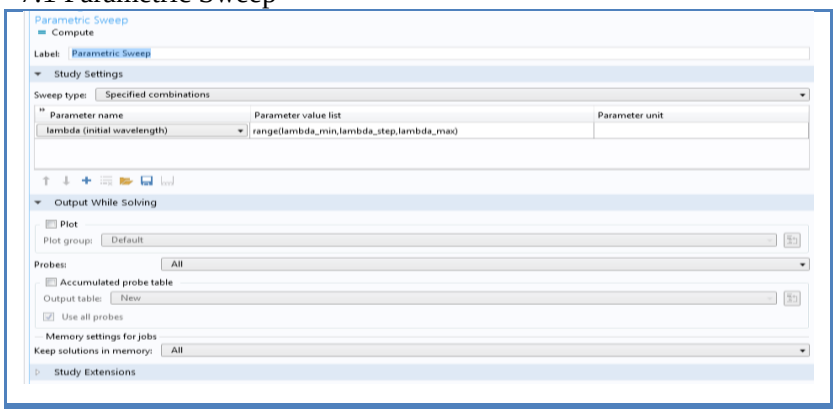

7.2 Frequency Domain

Label	Frequency Domain

Frequency unit	Hz
Frequencies	c_const/(λ1[nm])
Electromagnetic Waves, Frequency Domain	Physics settings (check in)

7.3 Solver Configuration

7.3 Solver Configuration

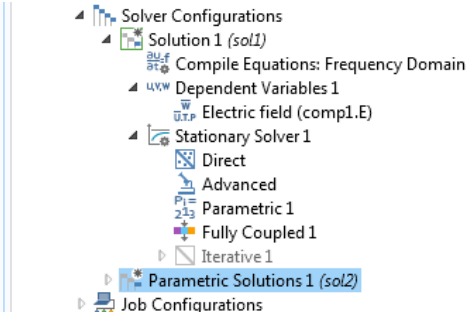

APPENDIX B - PUBLISHED ARTICLES

Scientific Research Publishing

Open Journal of Applied Sciences, 2018, 8, 126-139
http://www.scirp.org/journal/ojapps
ISSN Online: 2165-3925
ISSN Print: 2165-3917

Engineering a Localized Surface Plasmon Resonance Platform for Molecular Biosensing

Sajid Farooq, Renato E. de Araujo*

Laboratory of Biomedical Optics and Imaging, Federal University of Pernambuco, Recife, Brazil
Email: *renato.earaujo@ufpe.br

How to cite this paper: Farooq, S. and de Araujo, R.E. (2018) Engineering a Localized Surface Plasmon Resonance Platform for Molecular Biosensing. *Open Journal of Applied Sciences*, **8**, 126-139.
https://doi.org/10.4236/ojapps.2018.83010

Received: January 27, 2018
Accepted: March 19, 2018
Published: March 22, 2018

Abstract

In this work, we introduce a new perspective on the development of Localized Surface Plasmon Resonance (LSPR) optical biosensors. Computational simulations, focused on the assessment of the LSPR spectrum and spatial distribution of the electromagnetic field enhancement near a metallic nanoparticle, elucidated the behavior of crucial parameters, as figure of merit, bulk and molecular sensitivity, which governs a LSPR sensor performance. Gold and silver nanospheres were explored as starting point to assess plasmonic optical characteristics of the nanostructured sensor platform. Here, for the first time in the literature, Campbell's model was evaluated exploiting a NP size-dependence approach. The theoretical analyses indicate a nonlinear behavior of the bulk and molecular sensitivity as function of the NP size. Substantial LSPR peak shifts due to the adsorption of molecules layer on a NP surface were observed for nanoparticles with ~5 nm and ~40 nm radius. Moreover, on molecular sensing, LSPR peak shift is also determined by the thickness of adsorbed molecular shell layers. We observed that for 40 nm radius gold and silver nanospheres, significant LSPR peak shift could be induced by small (few nm) thickness change of the adsorbate shell layer. Moreover, this work provides insights on the LSPR behavior due to adsorption of molecular layer on a NP surface, establishing a new paradigm on engineering LSPR biosensor. Furthermore, the proposed approach can be extended to engineer an efficiently use of different nanostructures on molecular sensing.

Keywords

Localized Surface Plasmon Resonance, Optical Sensor, Nanomaterials

1. Introduction

The noble metal nanostructures strongly interact with light, resulting in size de-

Engineering a plasmonic sensing platform for *Candida albicans* antigen identification

Sajid Farooq,[a] Wendell W. Neves,[a] Omar Pandoli,[b] Tommaso Del Rosso,[b] Leonardo M. de Lima,[b] Rosa F. Dutra,[a] and Renato E. de Araujo[a,*]

[a]Universidade Federal de Pernambuco, Recife, Brazil

[b]Pontifícia Universidade Católicado Rio de Janeiro, Rio de Janeiro, Brazil

Abstract. We established a procedure to develop a localized surface plasmon resonance (LSPR) optical sensor platform for immunoassay. Computational simulations, focused on the assessment of the LSPR spectrum and spatial distribution of the electromagnetic field enhancement near the metallic nanoparticle, were used to engineer a nanostructured-sensing platform. Crucial parameters that rule the LSPR sensor performance, as bulk and molecular sensitivity, were evaluated, guiding the development of the optical platform. An LSPR surface-based platform composed of silver nanospheres adhered on a glass slide and functionalized with monoclonal anti-*Candida* antibodies of the IgG class was fabricated. Molecular biosensing was demonstrated by the identification of *Candida albicans* antigen. In particular, *C. albicans* is the most common species involved in a variety of hospital yeast infections. The developed sensing platform was able to identify *C. albicans* antigen concentration as low as 50 ng/mL, indicating the viability of exploring LSPR effect on *C. albicans* antigen biosensor. Moreover, this work provides insight on the LSPR behavior due to the adsorption of molecules layer on a nanoparticle surface, establishing a paradigm on engineering LSPR biosensor. [DOI: 10.1117/1.JNP.12.033003]

Keywords: localized surface plasmon resonance; nanoparticle; optical sensor; diagnostic device; Candida albicans.

Paper 18006SS received Jan. 15, 2018; accepted for publication Apr. 16, 2018; published online May 8, 2018.

1 Introduction

Optical-based sensors are fast, reliable, and fairly simple method for diagnostic medical devices. In particular, localized surface plasmon resonance (LSPR) phenomenon can be explored in order to obtain a cheap and accurate label-free molecular sensing.[1,2] It is known that metallic nanoparticles (NPs) may absorb or scatter light elastically with remarkable efficiency at the plasmon resonance frequency.[3] Moreover, the plasmon resonance frequency is reliant on the size, material, and shape of the NP and its environment.[4,5]

LSPR is associated to a collective oscillation of the conduction electrons in the metal. In principal, LSPR can be achieved in all metal, semiconductor by fulfilling the Frohlich condition: $[\mathrm{Re}(\epsilon) = -2\epsilon_m]$, where ϵ_m is the permittivity of surrounding nonabsorbing medium and ϵ; is the complex permittivity of NP.[6] Therefore, a negative value of the real component ϵ; is necessarily condition for LSPR. In particular, Au and Ag present a negative real permittivity and small positive imaginary permittivity, in the visible and infrared spectrum region, satisfying the Frohlich condition. Moreover, metals such as Na, Li, Al, Cu, Ga, Pt, and Pd can exhibit plasmon resonance on the UV–visible spectrum.[7]

However, these metals are easily oxidized and reactive to the surrounding medium. Consequently, Au and Ag NPs are highly attractive for sensing proposes.

*Address all correspondence to: Renato E. de Araujo, E-mail: renato.earaujo@ufpe.br

1934-2608/2018/$25.00 © 2018 SPIE

Photonics and Nanostructures - Fundamentals and Applications 31 (2018) 160–167

Contents lists available at ScienceDirect

Photonics and Nanostructures - Fundamentals and Applications

journal homepage: www.elsevier.com/locate/photonics

Optical properties of silver nanoplates and perspectives for biomedical applications

Sajid Farooq[a], Frederico Dias Nunes[b], Renato Evangelista de Araujo[a,*]

[a] Laboratory of Biomedical Optics and Imaging, Federal University of Pernambuco, Recife-PE, Brazil
[b] Departamento de Engenharia Nuclear, Federal Universityof Pernambuco, Recife-PE, Brazil

ARTICLE INFO

Keywords:
Localized surface plasmon resonance
Silver nanoplates
Sensitivity
Photodynamic therapy

ABSTRACT

Silver nanoplates of triangular shapes have attractive optical extinction spectrum with multipolar resonance modes. In this work, we investigate the optical properties of Ag nanotriangles and evaluate the feasibility of using it on LSPR biosensing and on photodynamic therapy. Three dimensional finite element simulation and experimental analyses were explored on the assessment of the LSPR spectrum and spatial distribution of the electromagnetic field enhancement near metallic nanoplates, with different altitude length and thickness. Refractive index based sensitivity (406 nm/RIU) and figure of merit (2.6) values were measured for AgNPls colloids, and attributed to dipole LSPR near field enhancement at the tips of the nanostructure. It was observed that LSPR field enhancement extend for more than 18 nm from the nanoparticle surface, indicating the viability of using the nanoplates on molecular sensing. The interaction of Ag nanoplates with Methylene Blue photosensitizer was also appraised, and a 2.2–fold metal enhanced single oxygen generation was determined. Our results indicate that Ag nanotriangles are promising candidates for biosensing and photodynamic application.

1. Introduction

Plasmonic nanostructures are increasingly receiving significant interest as an important starting point for medical therapy and medical diagnosis [1–4]. The interaction of incident light with noble metallic nanoparticle (Np) can induce a collective resonance of the conduction electrons, i.e., Localized Surface Plasmon Resonance (LSPR) [5,6]. Therefore, light can be elastically scattered or absorbed with remarkable efficiency, at a resonance frequency. The various reported examples of LSPR biosensors were proposed for the diagnosis of relevant medical disease, as Alzheimer [7], preeclampsia [8], influenza [9], HIV–1 [10], dengue [11], and hepatitis B infections [12]. Moreover, LSPR platform can also be applied on intracellular protein sensing [13] and colorimetric indicators [14]. Plasmonic nanoparticles have also been explored as contrast agents for optical imaging modalities as fluorescence microscopy and optical coherent tomography [15]. Metallic nanoparticles are usually not fluorescent, and therefore for imaging applications they are frequently tagged with fluorophores and targeting molecules [16]. Not only the remarkable optical properties of plasmonic nanoscale particles but also its high colloidal stability promote the use the nanostructures on cell/tissue optical images [17,18]. On medical therapy, metallic nanoparticles have been exploited on photo-thermal therapy (PTT) [19]. Light energy absorbed by the plasmonic nanostructures is converted to heat that dissipates, increasing the temperature of the Np surrounding medium. Various shapes as spheres, rods, shells and cages exhibit robust potential for thermal related therapy [20]. Likewise PTT, Photodynamic Therapy (PDT) has emerged as one of the important therapeutic options for numerous diseases treatment. PDT combines photosensitizing drugs and light to generate selective damage on a target tissue [21].

Moreover, photodynamic procedures are used either routinely in clinical management or in experimental studies in a diverse range of medical fields, such as oncology [22], dermatology [23], ophthalmology [24], gastroenterology [25], cardiology [26], neonatology [24], and mycology [27]. Several molecules can be probed as PDT photosensitizers (PS), as porphyrins, chlorines, phtalocyanine, naphtalocyanines, purpurins, aminoacridine, indocyanine green, and Methylene Blue [27,28]. In particular, cationic Methylene Blue (MB) is a photosensitizer with a high oxygen singlet, $^1O_2$, generation quantum yield, ~0.52 [29]. Furthermore, MB is a FDA-approved anti-microbial agent, and a low cost bacteriologic staining for histological applications [30–32].

The strong and intense near localized field that surrounds the plasmonic Np could improve the generation of oxygen singlet by a photosensitized molecule, phenomenon known as Metal Enhanced Oxygen singlet generation (MEO) [33,34]. The potential use of silver

* Corresponding author.
E-mail address: renato.earaujo@ufpe.br (R.E. de Araujo).

https://doi.org/10.1016/j.photonics.2018.07.001
Received 28 March 2018; Received in revised form 13 June 2018; Accepted 23 July 2018
Available online 10 August 2018
1569-4410/

Photodiagnosis and Photodynamic Therapy 22 (2018) 191–196

Contents lists available at ScienceDirect

Photodiagnosis and Photodynamic Therapy

journal homepage: www.elsevier.com/locate/pdpdt

Photodynamic inactivation assisted by localized surface plasmon resonance of silver nanoparticles: In vitro evaluation on *Escherichia coli* and *Streptococcus mutans*

Martha S. Ribeiro[a], Luciana S.A. de Melo[b], Sajid Farooq[b], Alessandra Baptista[a], Ilka T. Kato[d], Silvia C. Núñez[c], Renato E. de Araujo[b,*]

[a] Center for Lasers and Applications, IPEN-CNEN/SP, 05508-000, São Paulo, SP, Brazil
[b] Laboratory of Biomedical Optics and Imaging, Federal University of Pernambuco, Recife, PE, 50740-530, Brazil
[c] Biomedical Engineering Post-Graduation Program, Universidade Brasil, São Paulo, SP, Brazil
[d] The Engineering, Modelling and Applied Social Science Department, UFABC, 09210-580, Santo André, SP, Brazil

ARTICLE INFO

Keywords:
Metallic nanoparticle
Bacterial inactivation
Photosensitizer uptake
Antimicrobial
Blue LED

ABSTRACT

Localized surface plasmon resonance (LSPR) of gold nanoparticles has been reported to increase the antimicrobial effect of the photodynamic therapy. Although silver nanoparticles (AgNPs) are an efficient growth inhibitor of microorganisms, no studies exploring LSPR of AgNPs to enhance the photodynamic inactivation (PDI) have been related. In this work, we described the LSPR phenomenon of AgNP sand investigated its interaction with riboflavin, a natural photosensitizer. We evaluated the use of AgNPs coated with pectin (p-AgNP) in riboflavin (Rb)-mediated PDI of *Escherichia coli* (Gram- bacteria) and *Streptococcus mutans* (Gram + bacteria) using a blue light-emitting diode ($\lambda = 455 \pm 20$ nm) of optical power 200 mW. Irradiance was 90 mW/cm^2 and radiant exposure varied according to the time exposure. Uptake of Rb and p-AgNP by the cells was evaluated by measuring the supernatant absorption spectra of the samples. We observed that LSPR of p-AgNPs was able to enhance the riboflavin photodynamic action on *S. mutans* but not on *E. coli*, probably due to the lower uptake of Rb by *E. coli*. Taken together, our results provide insights to explore the use of the LPRS promoted by silver nanostructures to optimize antimicrobial PDI protocols.

1. Introduction

Light-based therapy and diagnosis are essential non-invasive tools for medical and biomedical applications. The interaction of light with biological tissue can be prompted with the use of external agents, as photosensitizers, dyes, scatters, and fluorescent particles [1,2]. In particular, photodynamic inactivation (PDI) has been extensively used as a promising antimicrobial approach since it does not promote the selection of mutant resistant strains [3,4]. PDI explores the light-interaction with specific photosensitizers (PSs) to induce oxidative stress on microorganism, leading to cell death via different targets [5,6].

More recently, metallic nanoparticles (NPs) have been also manipulated on the development of new biomedical sensor [7], contrast agents [8], and to improve light-based therapies [9–11]. Biomedical applications of metallic NPs are driven by the interaction of light with nanostructure that leads to a collective resonance of the conduction electrons in the metal, known as Localized Surface Plasmon Resonance (LSPR) effect [12]. At resonance, metallic NPs can scatter light with remarkable efficiency, enhancing the electric field density close to the metal surface. The NP material, size, shape and surrounding medium determine the magnitude and resonance frequency of LSPR effect [13]. Also, the field density boost can be sensed by molecules that are placed close to the NP, and therefore inducing, for instance, a luminescence enhancement.

To establish NP LSPR-PS interaction it is required that LSPR frequency and the PS absorption spectrum overlap. Thus, the PS could perceive the field enhancement close to the NP surface, and a better excitation of the PS molecule could be promoted [14]. In fact, spherical AgNPs present a LSPR peak at the blue region of the electromagnetic spectrum [15] and since some PSs can be excited using blue light, as porphyrins and riboflavin, singlet oxygen ($^1O_2$) generation by PSs could be enhanced by LSPR of AgNP [16].

Zhang et al. were the first to demonstrate that LSPR may induce singlet $^1O_2$ generation enhancement by displacing PSs on a non-continuous silver film [17]. Melo and coworkers also observed metal-enhanced singlet oxygen (MEO) generation in riboflavin (Rb) water

* Corresponding author.
E-mail address: renato.earaujo@ufpe.br (R.E. de Araujo).

https://doi.org/10.1016/j.pdpdt.2018.04.007
Received 23 August 2017; Received in revised form 11 April 2018; Accepted 13 April 2018
Available online 17 April 2018